AN ABSTRACT OF THE THESIS OF

Blaine R. Roberts for the degree of Doctor of Philosophy in Biochemistry and Biophysics presented on May 1, 2007.

Title: Structural Studies of the Antioxidant Defense Enzymes; Copper, Zinc Superoxide Dismutase and Alkyl Hydroperoxide Reductase Flavoprotein.

Abstract approved:

_____

Joseph S. Beckman

Oxygen derived radicals are involved in many aspects of life from aging and cell signaling to disease states as diverse as heart disease, diabetes, neurodegeneration and inflammation. Therefore, understanding the function of antioxidant defense proteins and the effects of oxygen derived radicals on protein function is essential to elucidate the role of reactive oxygen species in disease. This thesis describes the X-ray crystallographic structure and biochemical properties of two antioxidant defense enzymes; the N-terminal domain of alkyl hydroperoxide reductase flavoprotein (AhpF) of *Salmonella typhimurium* and zinc-deficient superoxide dismutase (SOD). In addition, the effect of peroxynitrite on the fluorescence of green fluorescent protein (GFP) was investigated.

The N-terminal domain of AhpF has two redox active cysteines that were found to be sensitive to X-ray induced reduction. Additionally, the disulfide redox center had an unusually low redox potential in relation to the pK_a of the active site thiols of other thioredoxin family members. The N-terminal domain of AhpF provides a platform to investigate the factors that govern the relationship between the pK_a and reduction potential of the active site cysteines.

Previous studies have shown that the loss of zinc from Cu,Zn SOD is sufficient to kill motor neurons and is important in the pathogenesis of amyotrophic lateral sclerosis. Structural studies reported herein revealed how zinc organizes the zinc-binding loop (loop IV), electrostatic loop (loop VII), and quaternary structure of SOD. The absence of zinc also increased the susceptibility of zinc-deficient SOD to aggregate in the presence of a reductant. Together these discoveries explain many of the properties that cause zinc-deficient SOD to be toxic to motor neurons.

Green fluorescent protein has been proposed as a real-time marker for tyrosine nitration in vivo. We demonstrate that GFP was not sensitive enough to monitor peroxynitrite-mediated nitration in vivo, even with large bolus additions of peroxynitrite totaling 150μM. Hence, measuring the loss of GFP fluorescence in cells has limited utility as a measure of nitrative stress.

Structural Studies of the Antioxidant Defense Enzymes; Copper, Zinc Superoxide Dismutase and Alkyl Hydroperoxide Reductase Flavoprotein.

by

Blaine R Roberts

A THESIS

submitted to

Oregon State University

in partial fulfillment of
the requirements for the
degree of

Doctor of Philosophy

Presented May 1, 2007

Commencement June 2007

Doctor of Philosophy thesis of Blaine R. Roberts presented on May 1, 2007

APPROVED:

_____

Major Professor, representing Biochemistry and Biophysics

_____

Chair of the Department of Biochemistry and Biophysics

_____

Dean of the Graduate School

I understand that my thesis will become part of the permanent collection of Oregon State University libraries. My signature below authorizes release of my thesis to any reader upon request.

_____

Blaine R. Roberts, Author

ACKNOWLEDGEMENTS

I would like to thank my mentor and thesis advisor Joe Beckman for providing me with continued encouragement, guidance and support throughout my graduate career. The opportunities that you have provided by introducing me to the many collaborators that have visited your lab and by sending me to scientific meetings, have allowed me to meet the people behind the papers and develop relationships with them that will prove to be instrumental in my continued development as a scientist.

I would like to extend my gratitude to Andy Karplus for all of his help in preparing manuscripts and coordinating with collaborators. Also thank you for introducing me to and teaching me X-ray crystallography.

I would also like to thank Mark Levy, Nate Lopez, Kristine Robinson, Val Bomben, Keith Nylin, Vlad Ermilov, and Irena Ermilova of the Beckman lab and Rick Faber, Ganapathy Sarma and Donnie Berkholz of the Karplus lab for all of their assistance, thoughtful conversation and friendship. I would also like to thank all of the undergraduates, Emily Clark, Chris Holguin, Andrew Kiemnec, Katie Myers, and Katie Jones who have worked with me during my graduate career.

I thank my undergraduate mentor, Ed Dratz, for giving me my first glimpse into the world of research. Also thank you for providing the motivational “kick” that I needed to continue in science.

Thank you to my family for all of their love and support. I would specifically like to thank Dave Roberts, my father, and Sue Roberts, my mother, for raising me on a farm, which allowed me the freedom to explore the biological process from an early age. My experiences on the

farm and my father’s background in biology have certainly been instrumental in fueling my scientific curiosity.

I would also like to extend my gratitude to my wife’s family for all of their help in a multitude of home remodeling projects that would certainly still be unfinished without their help.

Most importantly I would like to thank my wife Anne Roberts. Without her love and support I could not have accomplished this work. Anne, thank you for believing in me, encouraging me, and dealing with me through all of the trials and tribulations that I encountered over my graduate school experience. I would also like to thank my two daughters Abigail and Victoria Roberts for reminding me that true growth cannot occur without the love and support of family and friends.

CONTRIBUTION OF AUTHORS

My thesis advisor Joe Beckman was involved in the design, interpretation of results as well as the writing of the abstract and chapters 1,2,4,5. Andy Karplus was involved in the design, interpretation of results and writing of chapters 2 and 3. John Tainer and Elizabeth Getzoff purified, crystallized, and collected the X-ray diffraction data for chapter 2. John Tainer and Elizabeth Getzoff were also involved in the writing of chapter 2. Dean Malencik and Sonia Anderson were involved in the experimental design, data collection and interpretation of the analytical ultracentrifuge data present in chapter 2. Valerie Bomben and Kathrin Meyers were involved in the experimental design and data collection of dimer exchange data in chapter 2. Zachary A. Wood was involved in determining the crystallization conditions in chapter 3. Thomas Jönsson and Leslie B. Poole provided the purified protein used in chapter 3. Leslie B. Poole and was also involved in the writing of chapter 3. Chris Holguin and Emily Clark were involved in protein purification and data collection for chapter 4.

TABLE OF CONTENTS

Page

1. Introduction 1

2. Structural Characterization of Zinc-deficient Human Superoxide Dismutase and its Potential Implications for ALS 8

2.1 Abstract 9

2.2 Introduction 10

2.3 Results 13

2.4 Discussion 16

2.5 Materials and Methods 21

2.6 Acknowledgments 25

3. Oxidized and synchrotron cleaved structures of the disulfide redox center in the N-terminal domain of Salmonella typhimurium AhpF 38

3.1 Abstract 39

3.2 Introduction 39

3.3 Results 41

3.4 Discussion 43

3.5 Materials and Methods 47

3.6 Acknowledgements 50

3.7 Abbreviations 51

4. Exploring the Reactions of Peroxynitrite with Green Fluorescent Protein 56

4.1 Abstract 57

4.2 Introduction 58

4.3 Results 60

4.4 Discussion 62

4.5 Materials and Methods 64

5. Conclusion and Outlook 74

6. Bibliography 86

LIST OF FIGURES

Figure Page

2.1 Key structural features of wild-type Cu,Zn SOD 27

2.2 The copper active site of zinc-deficient SOD chain A 28

2.3 Disorder of the active site channel increases copper accessibility 29

2.4 Crystal contacts influencing structure 30

2.5 Origins of the shift in dimer orientation 31

2.6 Conserved conformation of Arg143 in human Cu,Zn SOD 33

2.7 Aggregation and heterodimer formation 35

2.8 Zinc-deficient SOD, an intermediate that can be formed by both wild-type and mutant Cu,Zn SOD may contribute to the cellular toxicity in ALS 36

3.1 Comparison of rNTD with the N-terminal domain of AhpF 52

3.2 Reduction of the NTD redox-active disulfide center by synchrotron radiation 53

3.3 Apparent pK_a determination of the active site Cys129 thiol(ate) 54

4.1 The structure of GFP and the fluorescent chromophore 69

4.2 Sensitivity of GFP fluorescence to peroxynitrite 70

4.3 Detection of nitrated GFP using a polyclonal antibody to nitrotyrosine 71

4.4 Difference spectra of denatured or native GFP treated with peroxynitrite 72

LIST OF FIGURES (Continued)

Figure Page

4.5 Nitration of glial cells expressing GFP-α-actinin with peroxynitrite 73

5.1 Location of ALS causing mutations on SOD 83

5.2 The link between the disulfide and the zinc binding site 84

5.3 The affect the loss of zinc has on the stability of the zinc loop 85

LIST OF TABLES

Table Page

2.1 Data collection and refinement statistics for zinc-deficient SOD 37

3.1 Data collection and refinement statistics for NTD..... 55

Dedication

In memory of my grandfather

Russell D. Roberts

1921 - 2005

Structural Studies of the Antioxidant Defense Enzymes; Copper, Zinc Superoxide Dismutase and Alkyl Hydroperoxide Reductase Flavoprotein.

Chapter 1

Introduction

The paradox of molecular oxygen (O_2) being both necessary for human life and yet being toxic can be understood using molecular orbital theory, which predicts two unpaired electrons occupying two π-antibonding orbitals. Usually, molecules with unpaired electrons are highly reactive. However, the molecular bonding of diatomic oxygen is kinetically unreactive compared to most other radicals. Oxygen can be transformed into reactive species, such as superoxide ($O_2^{\bullet -}$), hydroxyl radical ($^{\bullet}OH$), singlet oxygen ($^1O_2$*) and hydrogen peroxide (H_2O_2). Uncontrolled, reactive oxygen species are capable of reacting rapidly with other molecules, setting off a radical chain reaction similar to an atomic bomb. Nature has extensive antioxidant defenses to prevent, avoid, repair or contain reactive oxygen species. This thesis will explore subtle aspects of structural influences on the functioning of Cu,Zn SOD and N-terminal domain of alkyl hydroperoxide reductase flavoprotein, two antioxidant proteins that play major roles in minimizing the damage caused by reactive oxygen species. Lastly, the effects of peroxynitrite ($ONOO^-$) on the fluorescence of green fluorescent protein (GFP) were explored.

Copper, zinc superoxide dismutase (SOD) is distributed to many cellular components of eukaryotic cells including the cytosol, nucleus, peroxisomes and the mitochondrial intremembrane space and is even found in the periplasmic space of prokaryotes. [1; 2; 3] SOD is a 16 kDa protein that has one copper and one zinc ion bound per subunit. As the name implies, the main function of SOD is to catalyze the dismutation of superoxide (Scheme1).[4; 5]

Scheme 1:

$$2O_2^{\bullet -} + 2\,H^+ \longrightarrow O_2 + H_2O_2$$

The rate that SOD scavenges superoxide is nearly diffusion limited (~2 x 10^9 $M^{-1}s^{-1}$) and is independent of pH over the range of 5-9.5.[4; 6] Mechanistically, SOD scavenges superoxide through the successive reduction and oxidation of the bound copper. [4;7; 8] Zinc, although not directly involved in the dismutation of superoxide, is crucial for maintaining the pH-independence of the enzymatic rate of SOD and provides structural stability.[6; 9; 10; 11; 12; 13]

Mutations to the SOD1 gene are linked to 2-3% of the patients that have the fatal neurodegenerative disease Amyotrophic Lateral Sclerosis (ALS). ALS is typically an adult onset disease characterized by the progressive death of motor neurons in the spinal cord, brain stem and cortex. [14] The majority of ALS cases (90%) are sporadic without a known cause. The remaining 10% of ALS cases have a familial link.[15; 16] Currently, there are well over 100 missense mutations of SOD that have been identified. (www.alsod.org) The symptoms of both familial and sporadic cases of ALS are similar and may indicate that both forms of ALS are propagated by a comparable mechanism. Thus fostering the hope that elucidating the mechanisms that cause the familial form of the disease will be directly applicable to the sporadic cases as well. After 14 years of intensive research the mechanism of toxicity remains unclear. However, we do know that all of the mutations to the SOD1 gene are inherited in an autosomal dominant fashion, except D90A,[17; 18] and that transgenic animals over-expressing ALS mutant forms of SOD develop ALS symptoms.[16; 19] These observations have led to the consensus that mutations of SOD lead to a toxic gain in function for the enzyme that cannot be explained by simply a loss of superoxide scavenging activity.

Naturally, a plethora of hypotheses have been proposed for the toxicity of SOD in ALS.[20] For the purposes of this thesis, we will focus on the aggregation and the zinc-deficient SOD hypotheses. The aggregation hypothesis posits that the aggregation of SOD is causative of ALS. This hypothesis is based on the observations of SOD-rich aggregates in the motor neurons and astrocytes of familial ALS patients and transgenic animals expressing ALS-mutant SOD[20; 21; 22; 23] Putative mechanisms for how aggregates of SOD would be toxic to motor neurons include causing dysfunction of the mitochondria;[24; 25] depletion of chaperones;[26] and dysfunction of the ubiquitin-proteasome system.[21; 27] However, it is not clear if the large aggregates of SOD seen in tissue are directly toxic. Indeed there is evidence that the aggregation of SOD, which occurs late in the disease, are not themselves toxic and may be protective.[28; 29; 30]

Despite the ambiguity of toxicity, a number of studies have deduced the process of how SOD aggregates.[22] Investigations into ALS-causing mutants of SOD have shown that mutant SODs are destabilized and have an increased propensity to aggregate.[31; 32] Furthermore, the destabilization of SOD mutants correlates with disease progression where the fastest progressing mutants are also the most destabilized.[32] In vitro studies have shown that the formation of aggregation prone apo-monomers of SOD involves the reduction of the single disulfide and the loss of metals. [33; 34; 35] Because zinc is bound about 7000 times less tightly than copper it is likely that the process of aggregation from the holo enzyme involves a zinc-deficient intermediate, which may have important implications for ALS.[39]

The zinc-deficient hypothesis is based on aberrant copper chemistry causing the production of superoxide and the depletion of small molecular weight antioxidants such as ascorbate and glutathione.[36; 37; 38] Zinc-deficient SOD has been shown to be toxic to cultured motor neurons.[38] In addition, several ALS mutants of SOD have altered zinc-binding properties.[39; 40; 41] The toxicity of zinc-deficient SOD is hypothesized to result from catalyzing the

reduction of molecular oxygen to form superoxide (scheme 2) [38], which reacts with nitric oxide to create peroxynitrite.

Scheme 2:

$$SOD\text{-}Cu^{+1} + O_2 \longrightarrow SOD\text{-}Cu^{+2} + O_2^{\bullet -}$$

The source of electrons that fuel the production of superoxide may be small molecular weight reductants such as ascorbate, which reduces copper in zinc-deficient SOD 1,000 fold faster than in the zinc replete enzyme.[38] This thesis aimed to understand how the loss of zinc affects the structure and aggregation properties of SOD.

In general, oxygen derived radicals are thought to be detrimental to the health of a cell or organism and the constant battle of antioxidants versus reactive oxygen species is thought to play a central role for disease and aging.[42; 43] In disease processes such as heart disease, diabetes and ALS, reactive oxygen species are thought to evade the antioxidant defenses causing cellular dysfunction and ultimately clinical symptoms, such as the loss of motor function or heart attack. However, depending on the perspective of the organism, reactive oxygen species are not always detrimental. In the case of a bacterial infection, such as *Salmonella typhimurium*, neutrophils engulf and bathe the invading bacterium with hydrogen peroxide, hypochlorus acid, superoxide and peroxynitrite.[44; 45] In this case, reactive oxygen species are the hero for the host and the villain for the bacterium. To defend against the onslaught of reactive oxygen species, bacteria such as *Salmonella typhimurium* have several key defense enzymes, such as Cu,Zn SOD and an inducible system known as the alkyl hydroperoxide reductase system, which are able to efficiently reduce hydrogen peroxide, organic hydroperoxides and peroxynitrite using NADH as a source of reducing equivalents.[46; 47; 48; 49]

The alkyl hydroperoxide reductase system is found in many bacteria and is an essential response to exposure to reactive oxygen species.[50; 51] In *S. typhimurium,* the AhpR system is composed of two proteins, AhpF and AhpC. AhpC is a member of the peroxiredoxin family and has two redox-active

cysteinyl residues that are directly involved in the reduction of hydroperoxides.[52] During catalysis, the peroxidic cysteine of AhpC is oxidized to sulfenic acid (S-OH) by hydroperoxides. The resolving cysteine then condenses with the sulfenic acid to yield a disulfide.[53; 54; 55; 56] The oxidized form of AhpC is then reduced by AhpF thus completing the catalytic cycle.(Scheme 3)

Scheme 3

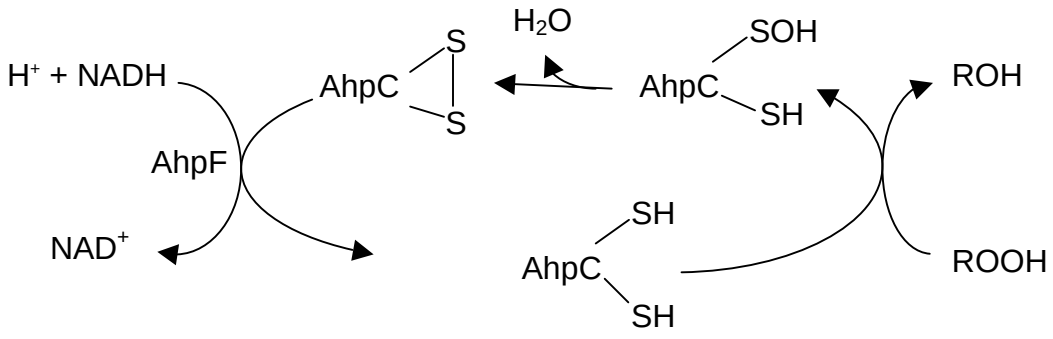

In this system, AhpF acts as a FAD-dependent protein disulfide reductase charged by the reductive power of NADH.[52; 57]

In *S. typhimurium,* the peroxidic cysteine of AhpC is resistant to the irreversible oxidation to a sulfinic acid (SO_2H). However, in mammals[58; 59; 60], plants[58; 59; 60] and yeast[61; 62], the peroxiredoxin homologues are more sensitive to irreversible inactivation by peroxides by a factor of 100. The exaggerated sensitivity of mammalian, plant and yeast peroxiredoxins to inactivation by peroxides has been proposed to be an adaptive feature for organisms that use peroxide signaling.[63] This so-called floodgate model proposes that under normal physiological conditions, peroxiredoxins keep peroxides levels low. However, during times of peroxide signaling, the flood of peroxides inactivate peroxiredoxins and thus allow peroxide to reach target proteins.[63] However, in *S. typhimurium,* high concentrations of peroxides indicates an attack; therefore inactivation of AhpC by peroxides would be detrimental to the bacterium because the AhpR system is essential for the bacterium's resistance to

hydrogen peroxide.[50] This thesis will explore the thioredoxin-like active site of the N-terminal domain of AhpF, which is responsible for reducing AhpC back to the dithiol form of the enzyme.

Directly measuring ephemeral reactive oxygen species in vivo remains one of the greatest challenges for understanding the role of oxidative stress in biology. The majority of techniques involve the detection of the oxidation products of amino acids, DNA and lipids. However, the recent advent of fluorescent probes that can specifically detect reactive oxygen species offers the promise of evaluating reactive oxygen species in vivo and in real-time. Two such probes are Mito-sox$_{RED}$^{tm}, which can form a novel product that appears to be specific for the detection of superoxide[64] and NiSPY which becomes fluorescent upon nitration by peroxynitrite.[65]

In addition to these two small molecular weight probes, green fluorescent protein has been suggested as a probe to measure in vivo nitration.[66] The fluorescence of GFP is dependent on the cyclization and spontaneous oxidation of the tri-peptide Ser65-Tyr66-Gly67.[67; 68; 69] GFP was initially suggested as a useful probe for nitration due to the requirement of Tyr66 for fluorescence. Espey et al.[66] hypothesized that the addition of a nitro group would quench the fluorescence and thus should provide a means to monitor nitration. In vitro, the authors showed that the GFP fluorescence was sensitive to bolus additions of peroxynitrite[66] However, the oxidative modifications that resulted in the decrease in GFP fluorescence were not determined and no evidence was provided to show whether the Tyr66-derived chromophore was directly modified by peroxynitrite or other reactive nitrogen species. In addition, the authors questioned the ability of peroxynitrite to cross cellular membranes to nitrate proteins based on the observation that the intracellular fluorescence of GFP was not affected by bolus addition of peroxynitrite. This thesis will provide evidence that GFP has limited utility as an intracellular marker for nitration, and that the loss of fluorescence that

results after treatment with peroxynitrite is due to the oxidative modification of residues other than Tyr66.

Chapter 2

Structural Characterization of Zinc-deficient Human Superoxide Dismutase and its Potential Implications for ALS

Blaine R. Roberts[1], John A. Tainer[2*], Elizabeth D. Getzoff[2], Dean A. Malencik[1], Sonia R. Anderson, Valerie C. Bomben[1], Kathrin R. Meyers[1], P. Andrew Karplus[1], Joseph S. Beckman[1,3,*]

Formatted for publication

2.1 Abstract

Over 130 mutations to copper, zinc superoxide dismutase (SOD) are implicated in the selective death of motor neurons found in 2% of amyotrophic lateral sclerosis (ALS) patients. Misfolding mutations that weaken SOD structure will also selectively decrease the enzymes affinity for zinc. Loss of zinc from SOD is sufficient to induce apoptosis in motor neurons *in vitro*. We report here the first crystal structure of zinc-deficient SOD at 2.0 Å resolution. The structure revealed a ca. 9^{o} twist of the subunits at the SOD dimer interface, which is the largest inter-subunit rotational shift yet observed for human a SOD variant. The electrostatic loop and zinc-binding sub-loop were disordered, the catalytically important Arg143 was rotated away from the active site, and the normally rigid intramolecular Cys57-Cys146 disulfide bridge assumed two distinct conformations. Together, these changes allow small molecules greater access to copper, consistent with the observed increased redox activity of zinc-deficient SOD. In addition, the dimer interface is weakened and the Cys57-Cys146 disulfide is more labile as demonstrated by the increased aggregation of zinc-deficient SOD in the presence of a thiol reductant. However, aggregation was prevented by addition of equimolar Cu,Zn SOD, which we show rapidly forms heterodimers with zinc-deficient SOD ($t_{1/2} \approx 15$ min). The apparent stabilization of zinc-deficient SOD as a heterodimer with Cu,Zn SOD may be a contributing factor to the dominant inheritance of ALS mutations.

2.2 Introduction

A major focus of neurodegeneration research involves the characterization of how the superoxide-scavenging enzyme Cu, Zn superoxide dismutase (SOD) is involved in amyotrophic lateral sclerosis (ALS). ALS is an adult onset disease involving the progressive death of lower motor neurons in the spinal cord and upper motor neurons in the brain stem and cortex.[14] In 1993, the first clue implicating a molecular cause for ALS came when mutations to the SOD gene were identified in approximately 2-3% of ALS patients. Since then, more than 130 different missense mutations as well as several C-terminal truncation mutations to the SOD gene have been linked to ALS (www.alsod.org).[16]

The discovery of a relationship between SOD mutations and ALS spurred intensive structural and other biophysical analyses aimed at revealing the molecular basis for the disease. Currently over 70 Cu,Zn SOD structures have been solved from various sources, including over 23 variants of human SOD. Human SOD is a tightly associated homodimer of 153 residues per subunit with each chain folding into an eight-stranded Greek key β-barrel (Figure. 1(a)). The active site channel on each subunit is formed on the outside of the β-barrels by two long loops (known as loop IV and loop VII) that bind copper and zinc ions, and also form part of the dimer interface. Of these, loop IV can be divided into a dimer interface subloop, a disulfide sub-loop and a zinc-binding sub-loop (Figure 1(a)). The dimer interface sub-loop forms 38% of the contact area that builds the dimer (Figure 1(b)). Loop VII, also known as the electrostatic loop, helps attract and orient superoxide anion into the active site.

Despite a wealth of structural and biochemical knowledge, how SOD is involved in ALS remains controversial. The mutations associated with ALS occur in all of the functional domains of the protein including the active site, dimer interface and β-barrel and many weaken the stability of SOD.[20; 21; 26; 70;

[71]. The seven available X-ray structures of ALS-causing SOD mutants (A4V [1N19[72],1UXM[70]], G37R [1AZV[73]], H43R [1PTZ[71]], H46R [1OZT[74]], I113T [1UXL[70]], D125H [1P1V[75]], S134D [134N[74]]) show some local distortions at the site of the mutation, but are otherwise remarkably similar to wild type Cu,Zn SOD, including the positions of the metals, the disulfide bridge, and the active site residue Arg143. However, the autosomal dominant inheritance and the development of motor neuron disease in transgenic animals over-expressing ALS SOD mutants provides strong evidence that these mutations somehow confer a toxic gain-of-function.[16; 19]

The loss of copper and zinc from SOD facilitates the reduction of the intra-molecular disulfide between C57 of the zinc-loop and C146 of the β-barrel. Recently, studies of SOD where the disulfide has been removed either by reduction or by mutation have shown that metal loss and disulfide reduction are thermodynamically linked to each other with disulfide formation contributing about 1.6 $kcal \cdot mol^{-1}$ to dimer stability.[33; 76] Structural studies of disulfide-free SOD with the holo or apo forms[33; 77] indicate that the disulfide stabilizes the dimer by ordering the interface sub-region of loop IV (Figure 1(a)). Furthermore, the side chain of Arg 143 is an important link between the interface, the disulfide regions of loop IV and the copper active site.[33; 78]

Reduction of the disulfide favors dissociation of Cu,Zn SOD into monomers, which greatly increases their propensity to form insoluble aggregates. Aggregation has been variously postulated to confer toxicity through disrupting mitochondrial function, interfering with chaperones,[26] or by inducing dysfunction of the ubiquitin-proteasome system.[20; 21; 27] Misfolded SODs may also preferentially associate with other proteins and even with RNA.[79] ALS mutant proteins have been shown to have increased hydrophobic character[80; 81] and associate with the anti-apoptotic protein Bcl-2 in a hydrophobic manner.[82] However, a major shortcoming of the aggregation hypothesis is that little evidence directly demonstrates that either SOD aggregates or apoSOD itself are directly toxic to motor neurons.[38; 83] A long

standing enigma is why the A4V mutation, which causes the most aggressive form of ALS in patients, does not produce disease when overexpressed in transgenic mice despite the presence of aggregated A4V protein in motor neurons.[19]

Many SOD mutations, including A4V, produce proteins that have comparable superoxide scavenging activity to that of wild-type SOD.[41] However, ALS mutations make the SOD mutants more susceptible to the loss of their metal cofactors. Zinc is more likely to disassociate than copper, because SOD has approximately a seven thousand fold lower affinity for zinc than it does for copper.[41] Zinc-deficiency dramatically increases the reduction of the active site copper by low molecular weight reductants such as ascorbate.[38] Delivery of zinc-deficient SOD intracellularly into cultured motor neurons by liposomes is sufficient to induce apoptosis. The basis for the toxicity of zinc-deficient SOD in this system was shown to involve increased redox activity of the remaining copper.[38] Furthermore, zinc-deficient wild-type SOD was shown to be just as toxic to cultured motor neurons as zinc-deficient mutant SOD.[38] Thus, the loss of zinc from wild-type SOD could be involved in the 98% of patients without SOD mutations. In the zinc-deficient hypothesis, the mutations to SOD do not directly cause the toxic gain-in-function, but rather increase the propensity of SOD to become zinc-deficient.

The loss of zinc from SOD is potentially important for both the aggregation and zinc-deficient hypotheses. Currently, structures are available for apoSOD,[74; 84] Zn,Zn SOD,[74; 75; 85] E,Zn SOD (i.e. copper-deficient SOD),[74] and for an engineered obligatory monomeric Cu,Zn SOD.[86] To characterize the effects of losing zinc, we have inactivated the zinc-binding pocket by generating mutations to create constitutively zinc-deficient SOD proteins. These mutations also prevent the migration of copper into the zinc pocket during the crystallization process. Here, we have solved the X-ray crystal structure of a zinc-deficient SOD protein and characterized how the loss of zinc affects dimer stability and aggregation.

2.3 Results

Crystal structure of zinc-deficient SOD.

The constitutively zinc-deficient SOD mutant H80S/D83S/C6A/C111S formed crystals belonging to the monoclinic space group C2 with unit cell constants that are unique among all previously observed SOD crystals. The asymmetric unit contained two chains of SOD constituting a dimer. The structure was solved by molecular replacement and refined to 2.0 Å resolution with final R/R_{free} factors of 0.19/0.25 (Table 1). The electron density map confirmed the presence of all four mutated side chains. Compared to either the wild-type or C111S/C6A Cu,Zn SOD, the basic fold of zinc-deficient SOD remained unchanged. The main chain conformations for the 123 residues principally forming the β-barrel core of SOD were well defined with an expected coordinate accuracy of 0.3 Å. These residues were generally similar in chains A and B (C_α rmsd=0.38 Å) and structural descriptions refer to both chains unless explicitly noted.

Consistent with the H80S/D83S mutations causing zinc-deficiency, electron density for zinc was absent in the zinc-binding site, but density for copper was clearly defined in the copper-binding site. Surprisingly, the coordination of copper remained quite similar to that found in Cu,Zn SOD. Even His63, which forms ligands with both copper and zinc in wild-type SOD, remained in a nearly native position in the zinc-deficient structure. In chain A, a small fraction (~17%) of copper could be modeled at an alternate position shifted by 1.3 Å to a location commonly associated with reduced (Cu^{1+}) SOD (Figure 2). Reduction of copper is commonly observed in SOD as the result of radiation-induced damage during data collection[87; 88]. However, only chain A of the SOD dimer had evidence for the alternate copper site.

The most striking change in the zinc-deficient SOD monomers was the lack of electron density for the zinc-binding section of loop IV (residues 68-78),

as might be expected from the loss of zinc coordination to its four ligands in this loop. The disruption extended to residues 132-139 of the electrostatic loop VII, which makes contacts with the zinc-binding sub-loop. The combined disordering of the electrostatic and zinc-binding loops substantially disrupted the active site channel, resulting in greater solvent accessibility of the copper (Figure 3).

The dimer interface of zinc-deficient SOD was substantially twisted compared to wild-type Cu,Zn SOD. Chain A was rotated 9° relative to chain B (Figure 4(a)) and exhibited subtle differences that affected the disulfide and interface sub-loop sections of loop IV (Figure 4(b)). The ca. 1.5 Å shift of the disulfide sub-loop into the dimer interface of chain A involves 5-15° shifts in the phi/psi angles of residues 53-59 and was accompanied by a new hydrogen bond between Thr58N and Ala55O. Together the changes in residues 53-59 of chain A result in a more pure 3_{10} helix. The shift in the disulfide sub-loop was also associated with a 0.6 Å shift of the guanidinium group of Arg143 away from the copper active site in chain A (Figure 4(d)). While Arg143 maintained hydrogen bonds to the carbonyl of Cys57 and two water molecules, Arg143 in the new conformation no longer formed hydrogen bonds to the carbonyl of Gly61, but instead formed a hydrogen bond to the carbonyl of Thr58. Coinciding with these shifts was the presence of two distinguishable conformations for the Cys57-Cys146 disulfide bridge (Figure 4(c)). The predominant conformation (occupancy=0.65) was the left-handed spiral conformation found in nearly all SOD structures; the second conformation involved a significant shift of only one atom, Cys146-Sγ, to yield a right-handed hook[89]. The conformations of Arg 143 and the disulfide subloop in chain B remained similar to those seen in wild-type Cu,Zn SOD.

Residues 124-131 of the electrostatic loop deviated substantially from other SOD structures due in part to a crystal packing interactions these residues make with the equivalent residues of a symmetry-related chain B subunit (Figure 5). Also, the observed asymmetry in the disulfide sub-loop of

chain A was stabilized by a crystal contacts with chain B of a symmetry mate (Figure 5). Two hydrogen bonds linked Arg143 of chain A with residues Lys91B_{sym} and Asp92B_{sym}, while Thr58A made two hydrogen bonds with Lys91B_{sym} and Glu40B_{sym}.

Comparison of the zinc-deficient SOD structure with other known structures.

To assess the novelty of various structural features seen in zinc-deficient SOD, an overlay was carried out with all human SOD crystal structures in the Protein Data Bank[90] with 2.0 Å or better resolution. Fifteen structures comprising 83 SOD chains meet these criteria. These comparisons show that the Arg143 conformation seen here was unusual, with only the A4V/C6A/C111S mutant having a similar positioning, and the artificially engineered monomeric form of human SOD having a conformation that is even more dramatically shifted from its canonical position (Figure 6(a)).

The partially occupied left-handed spiral conformation of the disulfide observed in this study was also rather unusual. A search of all SODs in the PDB (n=76) revealed at only three structures shared a similar conformation and partial occupancy. The human monomeric Cu,Zn SOD and “as-isolated” human Zn,Zn SOD (2C9U) displayed the partially occupied left-handed spiral disulfide however, in these cases it showed evidence of partial reduction with Sγ-Sγ distances of ~2.7 Å. The recently determined *Schistosoma mansoni* Cu,Zn SOD(1TO4) provides on additional example of partially occupied alternate conformation of the disulfide. Similar to the structure reported here, the *Schistosoma mansoni* disulfides Sγ-Sγ distances of ~2.1 Å indicating that the disulfide is oxidized.

Thiol-dependent aggregation and heterodimer formation.

The propensity of zinc-deficient SOD to aggregate was studied using analytical ultracentrifugation (Figure 7(a)). In the absence of the reductant dithiothreitol (DTT), all SODs tested, whether Cu,Zn or zinc-deficient, were resistant to aggregation (<10% aggregation after 72 hours at 20°C). In the presence of DTT, ~50% of both the D124N and D83S forms of zinc-deficient SOD aggregated, whereas < 5% of wild type and C111S Cu,Zn SODs aggregated. Surprisingly, the DTT-induced aggregation of both zinc-deficient SOD mutants was prevented by the addition of Cu,Zn SOD (Figure 7(a)). To determine whether heterodimers could form between Cu,Zn SOD and D83S SOD, two techniques were employed: fluorescence resonance energy transfer (FRET) and native gel electrophoresis (Figure 7(b) and 7(c)). Both approaches showed that subunit exchange between Cu,Zn SODs and D83S occurs readily at 37°C to create heterodimers; the measured half-lives were 17 ± 4 min and 12.5 ± 0.6 min for native gel and FRET experiments, respectively.

2.4 Discussion

Zinc-deficient SOD can be an important intermediate in both the aggregation and pro-oxidant models for ALS progression. The present structure reveals that the loss of zinc alters the structure of SOD far more than any ALS mutation that has been characterized to date. Overall, the zinc-deficient structure reveals features that help explain both its greater redox activity and susceptibility to aggregation. The most dramatic structural change is the disorder of the loop IV that forms the zinc-binding pocket containing all four zinc ligands. The electrostatic loop also becomes disordered because it makes significant contacts with the zinc loop. The disorder of these two loops is comparable to the disorder caused by the lack of both copper and zinc.[84]

The loss of zinc leaves the β-barrel itself essentially unaffected. In addition, the active site copper is in a nearly identical geometry in zinc-deficient SOD as found in oxidized Cu,Zn SOD. His63, which normally coordinates with both copper and zinc, also assumes a conformation similar to that found in Cu,Zn SOD even though much of the rest of loop IV is disordered. The remarkably similar geometries of the active site are consistent with the ability of oxidized (Cu^{+2}) zinc-deficient SOD to scavange superoxide at a rate that is nearly identical to the rate of Cu,Zn SOD.[6] However, the second step in catalysis, the oxidation of Cu^{+1} by superoxide, is slower and becomes pH dependent upon the loss of zinc from the enzyme.[6; 10]

An important consequence of the disruption of loops IV and VII is the opening of the narrow 4 Å wide channel that normally restricts small molecules from accessing the catalytic copper. The increased accessibility to the copper in zinc-deficient SOD provides a rationale for why copper in zinc-deficient SOD is more than a thousand-times more reactive with intracellular reductants such as ascorbate and glutathione than Cu,Zn SOD (Eqn. 1).[38] Although the reduced copper will continually be reoxidized by molecular oxygen to produce superoxide (Eqn. 2), in vivo the copper will tend to be maintained in a reduced state by oxidizing low molecular weight antioxidants to their respective free radical intermediates (Eqn. 1). With respect to motor neurons and ALS the depletion of ascorbate has been shown to be lethal in guinea pigs on a tocopherol-depleted diet.[91] This provides an additional mechanism that may account for the motor neuron toxicity of zinc-deficient SOD observed by Estevez et al.[38]

Ascorbate + Cu(II),E-SOD → Ascorbyl Radical + Cu(I),E-SOD (Equation 1)

$Cu(I),E\text{-}SOD + O_2 \rightarrow Cu(II),E\text{–}SOD + O_2^{\cdot -}$ (Equation 2)

Curiously, *Mycobacterium tuberculosis* expresses a membrane-bound, copper containing form of SOD (*Mt*SOD) that does not have a zinc-binding

site.[92] This *Mt*SOD is up-regulated and expressed on the extracellular surface of the mycobacterium upon entry into human macrophages, where superoxide levels are expected to be high.[93] Despite the absence of zinc, *Mt*SOD has an enzymatic rate comparable to that of most Cu, Zn SODs.[92] Consistent with zinc-deficient human SOD, the rate of superoxide dismutation of *M. tuberculosis* is pH dependent.[92] When exposed to high superoxide fluxes, as will occur in a macrophage phagosome, the rate of reoxidation (Eqn. 2) of Cu^{+1} by oxygen would be inconsequential. Because the host limits zinc availability within a macrophage, *M. tuberculosis* would have a selective advantage to express an efficient SOD lacking zinc[94]. To accommodate the absence of zinc, the dimer interface of *Mt*SOD involves the electrostatic loop and the addition of a unique dimerization loop.[92] The dimer interface in *Mt*SOD occludes more surface area and involves over 30 hydrogen bonds, compared to only a few hydrogen bonds in human SOD.[92] The increased stability of the dimer interface may be a mechanism to compensate for the loss in structural stability conferred by zinc in traditional copper and zinc containing SODs.

Crystal packing effects on structure.

An important aspect of the zinc-deficient SOD structure is that chain A assumed a somewhat different conformation from chain B and this is related to the structural changes in the dimer interface. In the crystal, the asymmetry observed in chain A was stabilized by interactions with symmetry-related molecules of chain B. This could represent an inherent asymmetry of zinc-deficient SOD or could have been induced by crystal packing interactions. Because so many SOD structures have been solved that do not show this asymmetry, we favor the hypothesis that the asymmetry reflects alterations to the dimer in solution. Even if this is not the case, the fact that the structure of chain A is perturbed in the crystal indicates that there has been a fundamental

destabilization of the structure to an extent not seen for other ALS SOD mutants characterized to date.

Zinc-loss leads to an altered dimer.

Rearrangements in loop IV along the dimer interface resulted in a nine-degree rotation in the monomer-monomer orientation, which is the largest shift reported for any SOD structure. The disorder in the normally rigidly held disulfide bond and the large rotation in the dimer interaction suggests that the monomer structure is itself more loosely packed and flexible, and that the dimer interface is also weaker. These observations are consistent with the loss of zinc being an initial step in the process of forming apo enzyme and consequent disulfide reduction, dimer dissociation, unfolding and aggregation. Except for the disorder of loops IV and VII, chain B closely resembles the structure of Cu,Zn SOD, while chain A shares features that are intermediate between a genetically engineered monomeric form of SOD and Cu,Zn SOD. The rotation of the guanidinium moiety of Arg143 away from the active site copper and movement of the disulfide region of loop IV are consistent with observations seen in the recently solved structures of the metal depleted, C57S, C146S disulfide mutants of SOD.[33] These changes in Arg143 emphasize the interconnections between the active site, the disulfide and the dimer interface.

Aggregation properties and insights into the mechanisms of disease. Monomeric

SOD subunits are now recognized to be a major intermediate in the formation of insoluble aggregates (Figure 8).[35; 78; 95] In the present study, we found that the thiol reducing agent DTT strongly promoted aggregation of zinc-deficient SOD. As noted above, the alternate conformation seen for the

Cys57-Cys146 disulfide in chain A of the zinc-deficient SOD structure is particularly noteworthy in this regard, as it implies a greater level of mobility that would be expected to correlate with greater ease of reduction. Remarkably, the thiol-dependent aggregation of zinc-deficient SOD was almost entirely prevented by the addition of Cu,Zn SOD (Figure 7(a)). As we have shown that heterodimers form readily (Figure 7(b) and (c)), we propose that Cu,Zn SOD prevents the thiol-dependent aggregation of zinc-deficient SOD through the formation of heterodimers with zinc-deficient SOD. Structurally this makes sense because the Cu,Zn subunit would stabilize the more native-like conformation of the disulfide section of loop IV in the zinc-deficient SOD subunit, and a more native conformation would make the disulfide less susceptible to reduction and thereby decrease the rate of formation of aggregation-prone monomers in the presence of DTT.

Possibly, the most intriguing aspect of this work is the implication of how heterodimer formation could influence disease progression. Cu,Zn and zinc-deficient SOD heterodimer formation significantly inhibits aggregation of the zinc-deficient enzyme (Figure 7(a)). The two different hypotheses of zinc-deficient toxicity and aggregation toxicity would predict different disease outcomes with respect to heterodimer formation. Under the aggregation hypothesis, heterodimer formation would be expected to decrease aggregation and therefore, lead to slower disease onset. According to the zinc-deficient SOD hypothesis (Figure 8), heterodimer formation would lead to more rapid disease onset because decreased aggregation would increase the lifetime of zinc-deficient mutant SOD, resulting in an increased consumption of ascorbate and production of superoxide. Indeed, crossing mice overexpressing wild-type SOD with FALS SOD mice accelerates development of motor neuron disease.[96; 97] Fukada et al.[96] attributed the accelerated disease progression to the stabilization of mutant SOD via the formation of heterodimers. In humans, FALS is an autosomal dominant disease, which allows for the formation of heterodimers of wild type and mutant SOD. The

zinc-deficient SOD structure provides new insights into how the formation of heterodimers with Cu,Zn wild-type SOD would stabilize zinc-deficient mutant SOD, a species known to be toxic to motor neurons, and thus contributes to the dominant inheritance of SOD mutations.

2.5 Materials and Methods

Description of SOD mutants. In the course of this work, we used five different forms of human Cu,Zn SOD with metal content assessed using the 4-pyridylazaresorcinol (PAR) assay[41]: wild-type (wild-type), C111S (C111S, 1.07 copper per monomer, 1.18 zinc per monomer), H80S/D83S/C6A/C111S (H80S/D83S), D124N/C111S (D124N,0.93 copper per monomer, 0.03 zinc per monomer), and D83S/C111S (D83S, 0.93 copper per monomer, 0.08 zinc per monomer). The previously characterized C111S and C6A mutations facilitate expression of soluble, stable protein from *E*. *coli* and do not significantly alter the structure or metal binding of SOD.[71; 98; 99] Mutation of the zinc ligands His80 and Asp83 makes SOD constitutively zinc-deficient. The D124N mutation was shown to yield a zinc-deficient SOD by disrupting hydrogen-bonds networks that stabilize the Zn ligands His46 and His71[12]. For the purposes of this study, we have grouped these variants into two categories: the normally “Cu, Zn” containing enzymes, wt SOD and C111S SOD, and the constitutively zinc-deficient (Cu, E) enzymes D124N SOD, D83S SOD and H80S/D83S SOD.

Expression and purification of SOD.

Zinc-deficient SOD was created by mutating the zinc-binding residues Asp83 and His80 to Ser or by mutating Asp124 to Asn using mutagenic PCR as previously described.[12; 72] All SOD proteins used in this study were expressed and purified from *E. coli* as previously described.[72; 98] Copper and

zinc content was determined using the 4-pyridylazaresorcinol (PAR) assay.[41] Protein concentrations were based on ε_{280}= 5,810 $M^{-1}cm^{-1}$ for the denatured protein that was calculated from the amino acid composition.[100]

Crystallization.

Crystals were grown at room temperature in less than one week using a reservoir of 2.45 M ammonium sulfate, 200 mM NaCl in 50 mM Tris, pH 7.5, and a drop made from 2 μL of 15.7 mg/mL protein in 50 mM Na/K phosphate pH 7.7 mixed with 2 μL of reservoir solution.

Data collection and refinement.

Diffraction data were collected at the Advanced Light Source (Lawrence-Berkeley National Laboratory, USA) at -170º C (1°oscillations; λ= 1.01 Å), and were processed using programs DENZO and SCALEPACK (Table I)[101]. The crystals formed in space group C2 with unit cell axes a=107.2 Å, b=35.9 Å, c=68.30 and β=104.8˚. All crystallographic refinement was done using the Crystallography and NMR System software (v1.1)[102]. A random 5% of the data were selected for cross-validation. The structure of the C6A, C111S SOD mutant (PDB code 1N18) succeeded as a search model to carry out molecular replacement against data from 20 to 5 Å resolution. Rigid body refinement yielded R/R_{free} values of 0.31/0.35, consistent with a correct solution. The $2F_O - F_C$ electron density map displayed well-defined density for residues 1-68, 79-131 and 140-153, however there was no clear density for atoms of the zinc binding sub-loop residues 68-78 or the electrostatic loop residues132-139 in either chain A or B. Hence, these residues were removed from the model for successive refinements. Residues 1-2, 23-28, 66-67 and 131 had weak backbone density but sufficient to allow them to be modeled. Local positional and B-factor refinement extending to 2.0 Å resolution, rapidly

dropped the R-factors to R= 0.226 and R_{free}= 0.273. Manual rebuilding of the model using the program O [103] was guided by $2F_O - F_C$ and $F_O - F_C$ electron density maps. Water molecules were added both manually and using the CNS utility Water-Pick with the following criteria: (1) a minimum 3σ peak in $F_O - F_C$ maps and (2) a reasonable hydrogen-bonding geometry. At the later stages of refinement, the largest positive difference peak corresponded to an alternate position for the Sγ atom of residue Cys 146. Occupancy of the Cys146-Sγ alternate position was selected as the value that yielded equivalent B-factors for the two positions [104]: final B-factors of ~30 $Å^3$ resulted from occupancies of 0.65 for the native-like Cys146-Sγ and 0.35 for the alternate conformation of Cys146-Sγ. Waters were numbered such that water 1 had the strongest electron density and water 193 had the weakest density. Waters with $2F_O$-F_c density of <1σ were removed from the model. Potential atomic clashes and erroneous side chain rotamers were identified with Molprobity [105]. Refinement was considered complete when the largest difference map peaks were not interpretable and R and R_{Free} had converged. Final statistics are reported in Table I. In addition, 100% of the ϕ,ψ-angles are in the allowed regions of the Ramachadran plot.

Root-mean-square deviation calculations and structural overlays were performed using the program HOMOLOGCORE (P.A. Karplus). The program HBPLUS v2.24 was used to define hydrogen bonds within the zinc-deficient model [106]. Structural figures were made using PyMOL[107].

Native gel electrophoresis.

Wild-type Cu, Zn SOD (40 μM) and D83S (40 μM) were combined in 100 mM sodium phosphate, pH=7.4, and 100 mM sodium chloride and incubated at 37° C for the time indicated. After incubation samples were flash frozen with liquid N_2. Samples were prepared with native sample buffer (Bio-Rad) and resolved using 7.5 % acrylamide/bis-acrylamide (37.5:1) resolving

gel and a 3% stacking gel. Electrophoresis was carried out at 4° C for 120 min. at 130 V. The gel was then stained with Coomassie Blue and quantified with NIH Image (http://rsb.info.nih.gov/nih-image/). Heterodimer formation was quantified as density of heterodimer band divided by the total density of all three bands.

Fluorescent resonance energy transfer (FRET).

SOD protein samples were conjugated to primary amines via succinamide esters of either donor fluorphore Alexa594 or acceptor fluorophore Alexa647 as described by the manufacturer (Invitrogen, Eugene, OR). Briefly a 10-fold molar excess of reactive dye was allowed to react with SOD for 2 h at pH=8.0 and 4° C. Conjugated SOD was purified from free dye using a Sephadex G25 column (30 cm x 0.75 cm) pre-equilibrated with 100 mM phosphate buffer, pH = 7.4. The degree of labeling ranged between 0.8 and 1.3 conjugates per SOD monomer. Fluorescent measurements were carried out at 37º C. Protein concentrations were 100 nM of each the acceptor and donor labeled protein. Fluorescence was measured by irradiating the sample with 586 nm excitation and monitoring the emission at 670 nm. To correct for background fluorescence, separate measurements were taken of the acceptor-labeled or donor-labeled SOD.

Analytical ultracentrifugation.

Equilibrium experiments were performed in a Beckman Optima XL-A analytical ultracentrifuge. Buffer densities and viscosity corrections were made according to Laue et al.[108]. The partial specific volume of SOD (0.725 cm^3/g) was estimated from the protein sequence[109]. The buffers were 100 mM potassium phosphate, pH 7.4, 100 mM NaCl with or without 1 mM DTT. Sedimentation velocity runs were performed at 20°C using a four hole AN-60Ti

rotor and double-sector charcoal/Epon filled centerpieces. 10 μM SOD samples (A_{230}=0.8) were centrifuged at 42,000 rpm. Aggregation of the protein was measured as a loss in absorbance. Scans were collected using absorbance optics and analyzed by the method of van Holde and Weischet[110], or an enhanced method as implemented in the UltraScan software[111; 112]. This analysis yields the integral distribution G(s) of diffusion-corrected sedimentation coefficients across the sedimentation boundary. In addition, the data were analyzed by the computer program Sedfit. This software analyses analytical ultracentrifuge velocity data files by direct fitting with numerical solutions of the Lamm Equation[113].

Sedimentation equilibrium experiments were performed at 20°C according to procedures described[114]. Typically, three 120-μl samples of 10 μM SOD were centrifuged to equilibrium at 3 different speeds from 15,000-22,000 rpm. Scans were collected with absorbance optics at wavelengths between 230 and 280 nm. The radial step size was 0.001 cm, and each **c** versus **r** data point was the average of 15 independent measurements. Wavelengths were chosen so that no points exceeded an absorbance of 1.0. Using UltraScan software, equilibrium data were fit to multiple models using global fitting. The most appropriate model was chosen based on the statistics and on visual inspection of the residual patterns.

Coordinates.

The coordinates and structure factors have been deposited in the Protein Data Bank (http://www.pdb.org/).

2.6 Acknowledgements

This publication was made possible in part by the Environmental Health Sciences Center supported by grant number P30 ES00210 from the National

Institute of Environmental Health Sciences, NIH. We appreciate the assistance of Rick Faber and Donnie Berkholz. This research was supported by grants ES00040 and AT002034-02 from the National Institute of Environmental Health Sciences to JSB.

Figure 2.1

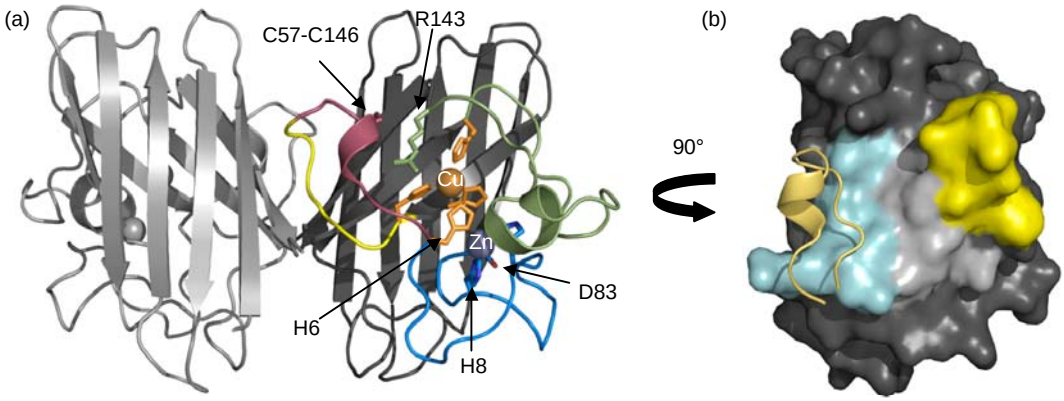

Figure 2.1 Key structural features of wild-type Cu,Zn SOD (PDB code 1HL5). (a) In the right hand monomer (chain A) copper (orange) and zinc (grey) are shown as spheres. Loop IV is divided into three sections; the dimerization sub-loop (yellow) creates part of the dimer interface, the disulfide sub-loop (raspberry) covalently attaches to the β-barrel via the Cys57-Cys146 disulfide and the zinc-binding region (blue) contains His63, His71, His80 and Asp83 (shown as sticks). Copper is coordinated by residues His63, His46, His48, and His120 (orange sticks). (b) Surface buried upon dimerization is shown for chain A. The ca. 1400 $Å^2$ area is divided into three regions contributed by the dimerization sub-loop (yellow), area buried by the interaction with the dimerization sub-loop of chain B (cyan with yellow ribbon showing chain B segment) and additional surface (light grey). As shown, the dimerization sub-loop is involved in ~ 75% of the total surface area buried.

Figure 2.2

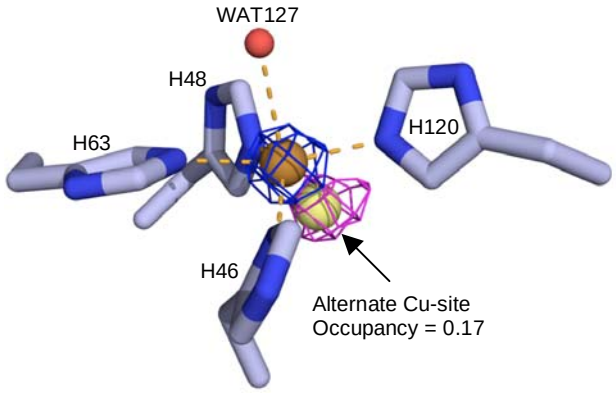

Figure 2.2 The copper active site of zinc-deficient SOD chain A. The 2Fo-Fc electron density is contoured at 7σ (blue mesh) and the Fo-Fc difference map after omitting the alternate copper is contoured at 3σ (magenta mesh). The axial water (red sphere) and histidine residues 46, 48, 63, 120 coordinate Cu^{2+} (orange sphere) with a distorted square planar geometry. The magenta positive density peak (peak height 5.7σ) indicates some of the copper (light yellow sphere) is in the alternate copper site, implying that it is in the Cu^{1+} state.

Figure 2.3

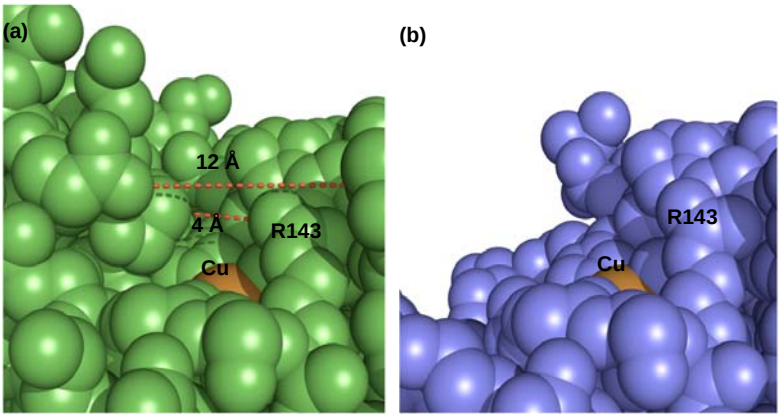

Figure 2.3 Disorder of the active site channel increases copper accessibility. (a) Access to the active site copper (orange) of wild type Cu,Zn SOD (green) is limited by the electrostatic and zinc-binding loops. The red dashes illustrate the dimensions of the active site channel, which narrows from ca. 12 Å to ca. 4 Å. (b) The active site of zinc-deficient SOD (blue) is open and more accessible due to the disorder of the electrostatic and zinc-binding loops.

Figure 2.4

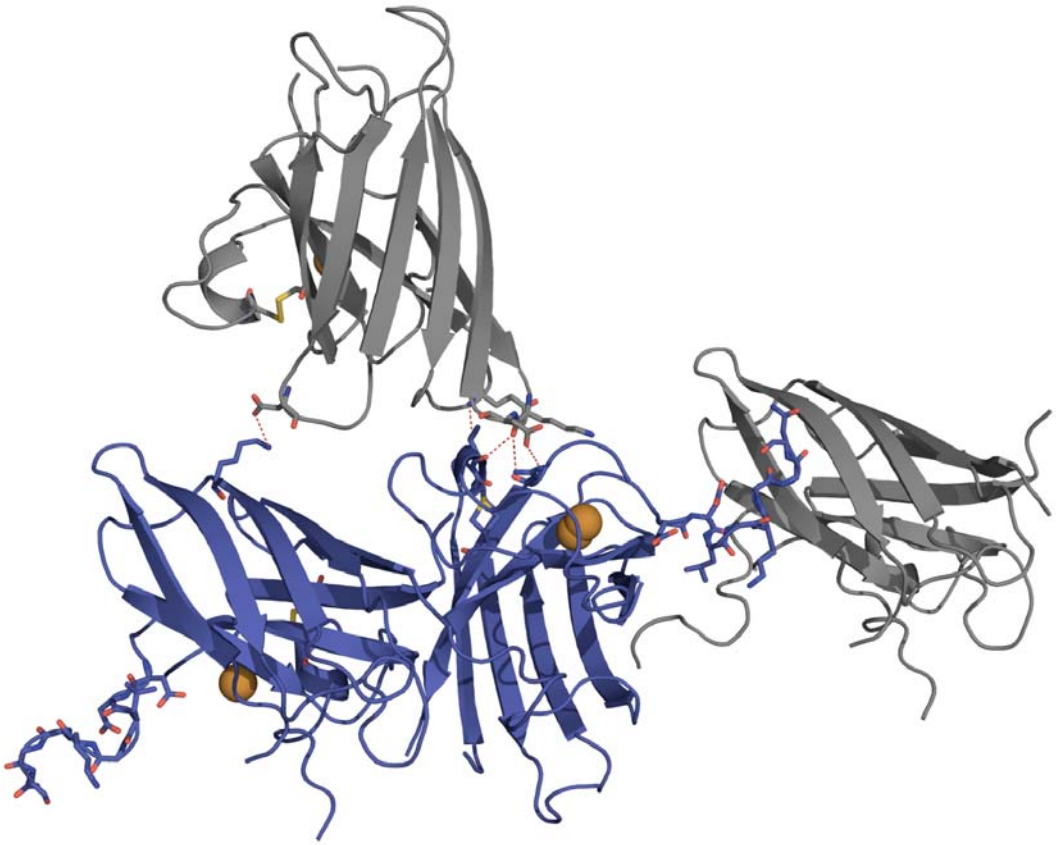

Figure 2.4. Crystal contacts influencing structure. Chain B of a symmetry related molecule (grey; Sym1) contacts both chains A and B (blue) of the asymmetric unit. The inset shows the symmetry mate makes four hydrogen bonds (red dashes) with chain A. The Sym1 symmetry mate also makes a single salt bridge with chain B. The electrostatic loop residues 124-131 are ordered due to an interaction across a two-fold with the same residues of another (Sym2) symmetry related molecule.

Figure 2.5

Figure 2.5 Origins of the shift in dimer orientation. (a) The zinc-deficient SOD dimer (blue ribbon) was overlaid with C6A, C111S Cu,Zn SOD (gray ribbon) based on the left hand monomer (chain A). The shift in the right hand monomer orientation of 9.3° can be seen in the misalignment of the ß-barrel. The average shift between zinc-deficient SOD and five different human SOD structures is 9.3°± 1.4°(std) (n=21 dimers)[pdb codes 1PU0, 1N18, 1HL5, 1HL4,1OZT]. (b) Close up view of the shift in the disulfide sub-loop of chain A towards the dimer interface. Thr58 prevents the shift in Arg143 due to clashes that would be created between the Nη and Cα of Thr58. The shift in the disulfide sub-loop is ca. 1 Å as measured at the Cα atom of Thr58. (c) The left-handed spiral conformation found in Cu,Zn SOD and in chain A and B of the zinc-deficient structure (orange spheres). The right-handed hook conformation observed as an alternate conformation in chain A of zinc-deficient SOD (yellow sphere) is shown with omit Fo-Fc density contoured to 3σ (magenta mesh). (d) Stereo image of the altered position of Arg143 in Chain A. In wild type Cu,Zn SOD (PDB code 1HL5) Arg143 H-bonds (gray dashes) to three waters (gray spheres), to the carbonyl oxygen of Gly61 and to the carbonyl oxygen of Cys57. Conversely, Arg143 in chain A of zinc-deficient SOD makes no H-bonds to Gly61-O, but makes a new H-bond to Thr58-O (red dashes).

Figure 2.5

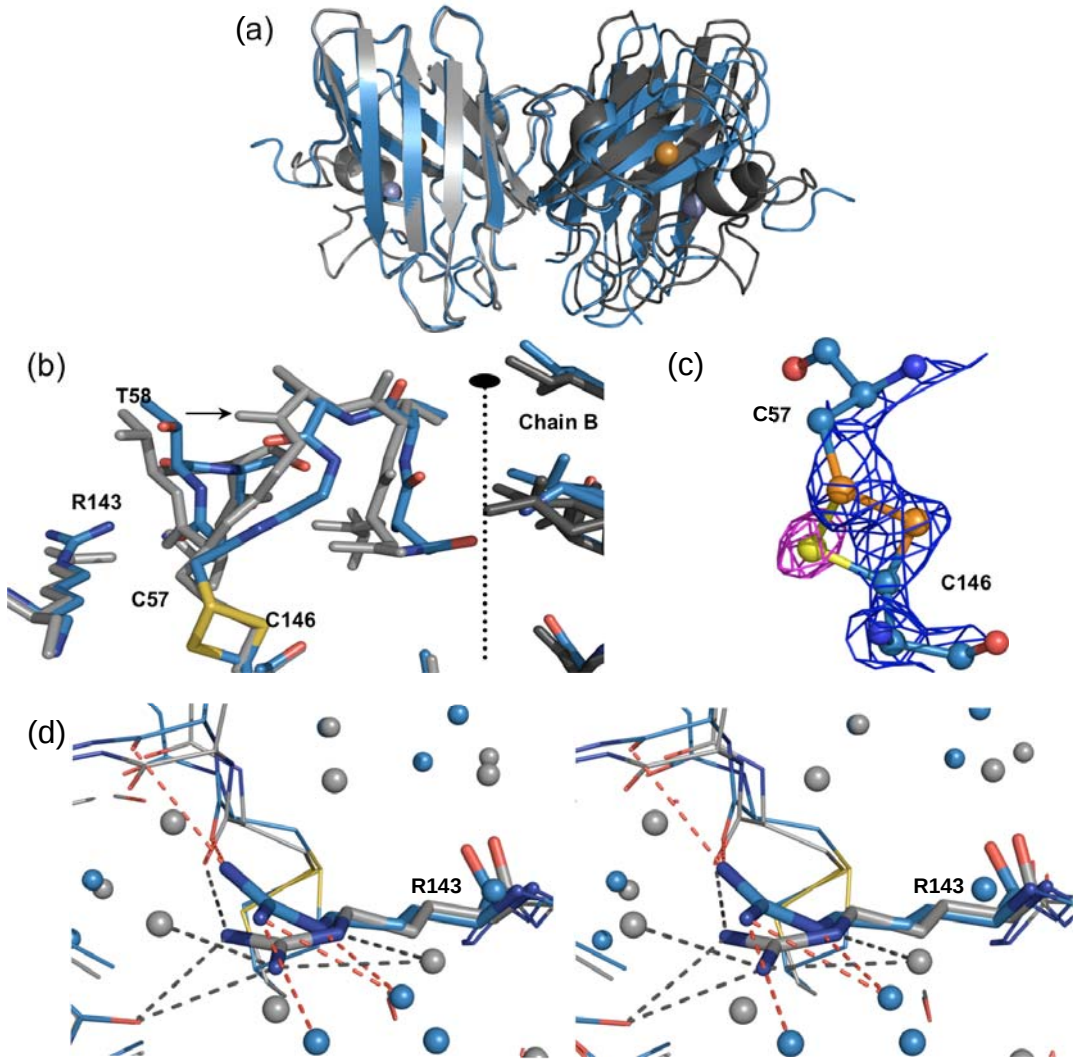

Figure 2.6

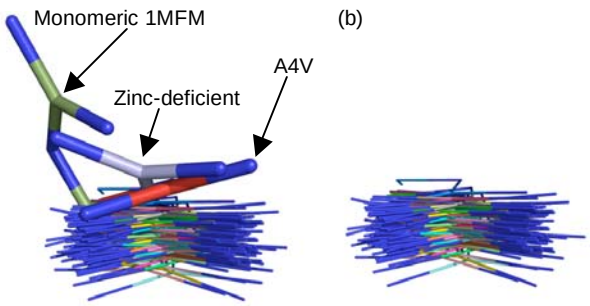

Figure 2.6. (a) Comparison of 83 independent Arg143 sidechains from 15 human SOD structures with resolution of 2.0 Å or better (PDB codes 1AZV, 1HL4, 1HL5, 1MFM, 1N18, 1N19, 1OZU, 1P1V, 1PTZ, 1PU0, 1UXL, 1UXM, 2C9S, 2C9U, 2C9V). The overlay was based on the main chain and Cβ atoms of Arg143. Arg143 of the monomeric (green, 1MFM), chain A of A4V/C6A/C111S (red, 1N19) and chain A of zinc-deficient (blue) SOD are shown as thicker models. (b) Overlay excluding the Arg143 of A4V/C6A/C111S, monomeric and zinc-deficient SOD showing that no other conformations were hidden by the sticks in panel A.

Figure 2.7

Figure 2.7. Aggregation and heterodimer formation. (a) The stability of the protein against aggregation is measured as the amount of protein remaining in solution at the end of a 72 h analytical ultracentrifuge equilibrium run. Copper and zinc containing SOD (open bars), zinc-deficient SOD (hashed bars) and zinc-deficient SOD mixed with Cu,Zn SOD (filled bars) were all measured with and without DTT as indicated (n=2). (b) SOD Native gel electrophoresis shows the time course of the formation of heterodimer as monitored by the appearance of a middle band. The half-life of heterodimer formation determined using densitometry was 17 ± 4 min (s.d.,n=3). (c) Shown is increase fluorescence at 670 nm as a function of time after mixing Alexa 647 conjugated zinc-deficient SOD(D83S) and Alexa-594 conjugated Cu,Zn SOD. Heterodimer formation was measured as an increase in fluorescence resonance energy transfer as indicated by the increase in the acceptor (Alexa 647) fluorophore fluorescence at 670 nm. The half-life of heterodimer formation was measured to be 12.5 ± 0.6 min (s.d.,n=3).

Figure 2.7

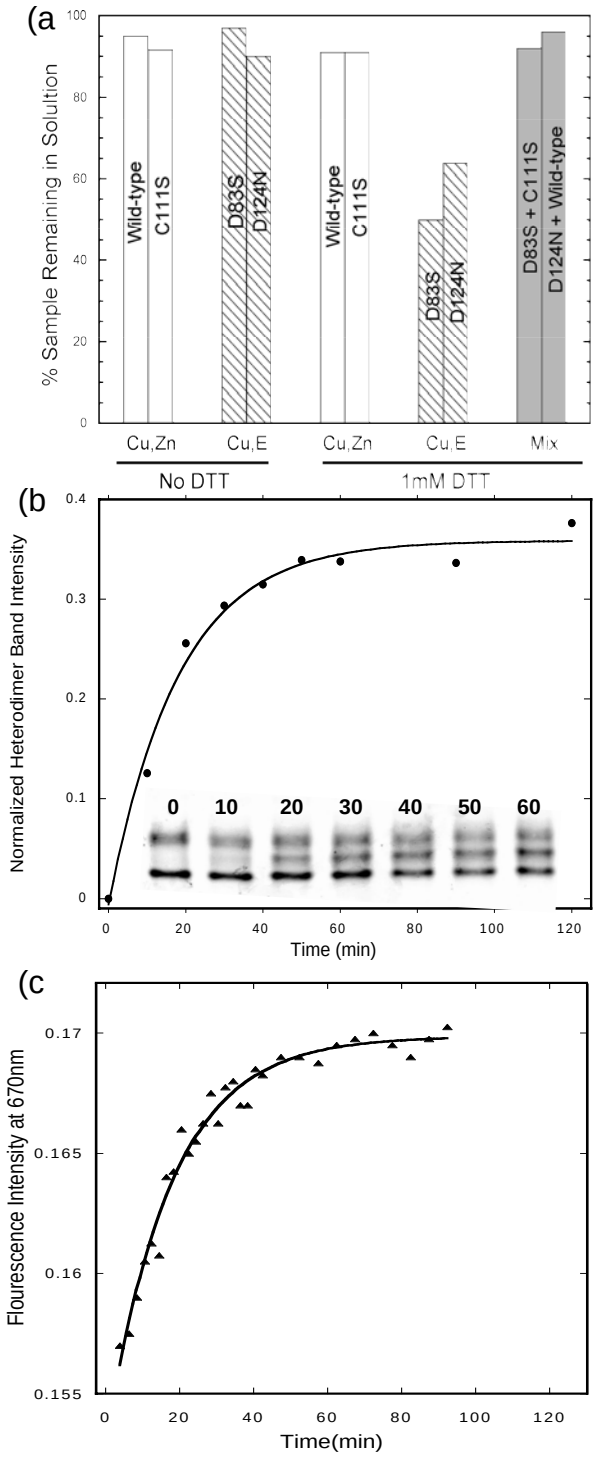
(a
% Sample Remaining in Solution
Wild-type
C111S
D83S
D124N
Wild-type
C111S
D83S
D124N
D83S + C111S
D124N + Wild-type
Cu,Zn
Cu,E
Cu,Zn
Cu,E
Mix
No DTT
1mM DTT
(b
Normalized Heterodimer Band Intensity
0
10
20
30
40
50
60
Time (min)
(c
Flourescence Intensity at 670nm
Time(min)

Figure 2.8

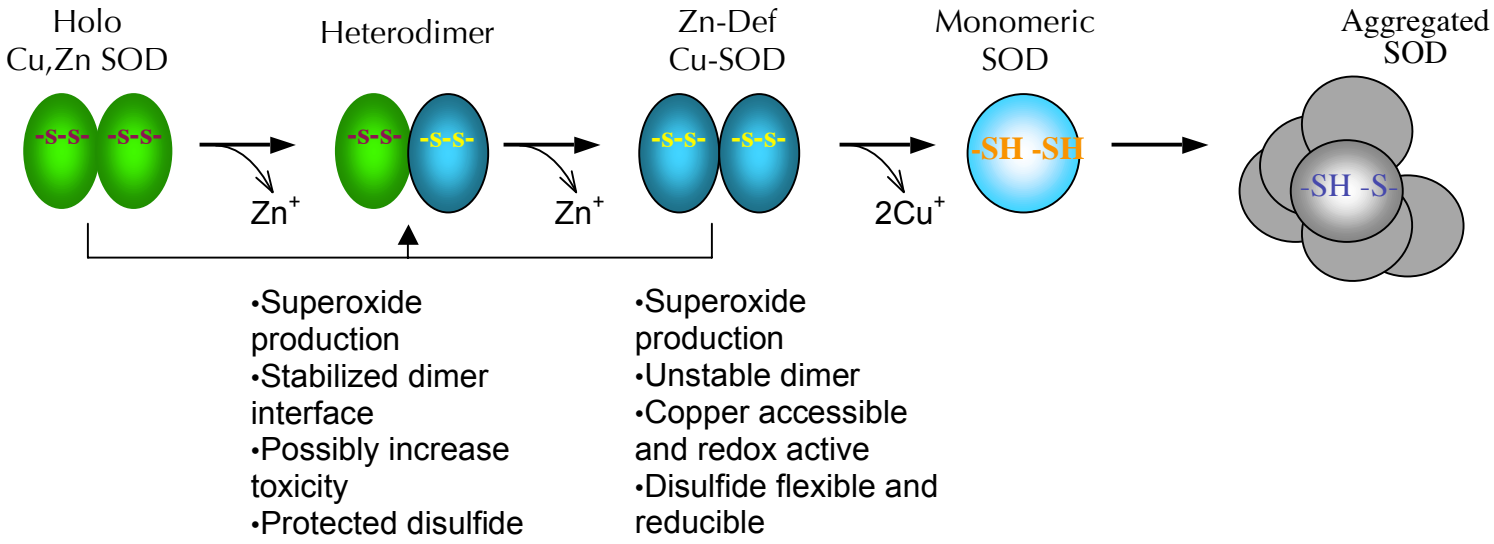

Figure 2.8. Zinc-deficient SOD, an intermediate that can be formed by both wild-type and mutant Cu,Zn SOD may contribute to the cellular toxicity in ALS. The loss of zinc or lack of zinc incorporation creates zinc-deficient heterodimers that are capable of producing superoxide and catalyzing the oxidation of ascorbate. This study describes how the loss of zinc both leads to disorder of loops IV and VII allowing access to the active site cooper and perturbs the quaternary structure of SOD to enhance its susceptibility to disulfide reduction and aggregation. The formation of heterodimers decreases the propensity of zinc-deficient SOD to aggregate and hence increases the lifetime over which zinc-deficient subunits can produce superoxide and deplete ascorbate. In this light, the enhanced toxicity seen when wild type SOD is coexpressed with mutant SOD[96] would seem to support the pro-oxidant hypothesis for ALS.

Table 1.1. Data collection and refinement statistics for zinc-deficient SOD

Data collection	
Resolution limits (Å)	20-2.0 (2.07-2.0)
Unique observations	15899
R_{sym}	0.061 (0.267)
Completeness (%)	95.8 (94.5)
Refinement	
No. of protein molecules	2
No. of amino acid residues	268
No. of water sites	190
Average B-factor ($Å^2$)	36
R_{Work}	0.187
R_{Free} (5% of data)	0.246
r.m.s.d. bond lengths (Å)	0.016
r.m.s.d. bond angles (°)	1.84

[a.] Numbers in parentheses correspond to values in the highest resolution shell

Chapter 3

Oxidized and synchrotron cleaved structures of the disulfide redox center in the N-terminal domain of *Salmonella typhimurium* AhpF

Blaine R. Roberts, Zachary A. Wood, Thomas J. Jönsson, Leslie B. Poole, and P. Andrew Karplus

Published in *Protein Science*,
The Protein Society, Bethesda, Maryland, USA
2005, **14** (9), 2414-2420.

3.1 Abstract

The flavoprotein component (AhpF) of *Salmonella typhimurium* alkyl hydroperoxide reductase contains an N-terminal domain (NTD) with two contiguous thioredoxin folds but only one redox-active disulfide (within the sequence –Cys_{129}-His-Asn-Cys_{132}-). This active site is responsible for mediating the transfer of electrons from the thioredoxin reductase-like segment of AhpF to AhpC, the peroxiredoxin component of the two-protein peroxidase system. The previously-reported crystal structure of AhpF possessed a reduced NTD active site although fully oxidized protein was used for crystallization [Wood, Z.A., Poole, L.B., and Karplus, P.A. 2001. *Biochemistry* **40:** 3900-3911]. To further investigate this active site, we crystallized an isolated recombinant NTD (rNTD); using diffraction data sets collected first at our in-house X-ray source and subsequently at a synchrotron, we show that the active site disulfide bond (Cys129-Cys132) is oxidized in the native crystals, but becomes reduced during synchrotron data collection. The NTD disulfide bond is apparently particularly sensitive to radiation cleavage compared to other protein disulfides. The two data sets provide the first view of an oxidized (disulfide) form of rNTD, and show that the changes in conformation upon reduction of the disulfide are localized and small. Furthermore, we report the apparent pK_a of the active site thiol to be ~5.1, a relatively low pK_a given its redox potential (-265 mV) compared to most members of the thioredoxin family.

3.2 Introduction

The alkyl hydroperoxide reductase system found in many eubacteria is responsible for catalyzing the reduction of hydrogen peroxide and organic hydroperoxides to their corresponding alcohols and water [47; 48; 49]. This peroxide-inducible system helps to protect cells against oxidative and

nitrosative damage to DNA and other cellular macromolecules [46]. The two protein components, AhpF and AhpC, work together to use NADH to reduce the hydroperoxide substrates as seen in Scheme 1:

Scheme 1

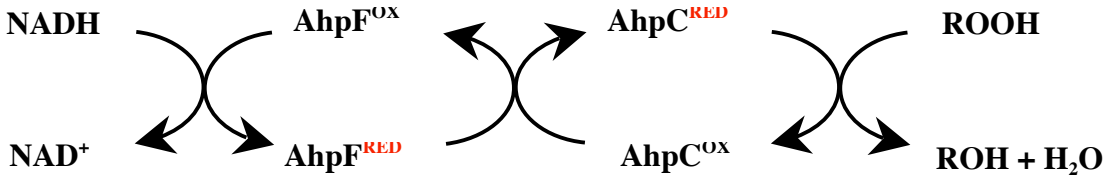

The AhpC component of the *Salmonella typhimurium* system is a member of the peroxiredoxin family and has two redox-active cysteinyl residues involved in the reduction of hydroperoxides [115]. The structure of AhpC has been solved in both the oxidized [56] and reduced [63] forms, and it is proposed to go through a dimer-decamer transition during its catalytic cycle [56]. The AhpF component is a homodimeric flavoenzyme (2x 57 kDa) composed of three domains, a 196-residue N-terminal redox domain (NTD), and a portion similar to *E. coli* thioredoxin reductase (TrxR), which includes an FAD binding domain and an NADH/redox-active disulfide domain (NADH/SS) [116].

The NTD domain of AhpF, the focus of this work, is the direct electron donor to AhpC, and it effectively acts as an appended substrate for the TrxR-like portion of AhpF [49; 116]. Indeed, both soluble recombinant NTD (rNTD) mixed with TrxR and NTD fused to TrxR endowed TrxR with AhpC reducing activity [117; 118]. In the crystal structure of AhpF [119], the NTD was seen to be attached to the FAD domain of AhpF by a flexible 14-residue linker consistent with its role as an appended substrate. In addition, the NTD was seen to be representative of a new class of thioredoxin-related proteins that contain a single redox-active disulfide in the context of two fused thioredoxin folds, the active site itself having a mirror image relationship to that of thioredoxin. A surprising result from the crystal structure of AhpF was that, although the oxidized protein was used for crystallization, the active site cysteines of the NTD (Cys129 and Cys132) were found to be in the reduced form. They

demonstrated a very close sulfur-sulfur distance of ~ 3 Å, and this interaction was proposed to be a thiol-thiolate hydrogen bond (Wood et al. 2001).

To further characterize this interesting variation on the thioredoxin motif, we are pursuing biochemical, and structural (NMR and X-ray) investigations of the isolated rNTD, which is smaller and more amenable to analysis than is intact AhpF. Here, we characterize the rNTD crystal structure and the pK_a of the active site Cys. We show that the rNTD active site disulfide is exquisitely sensitive to radiation-induced cleavage and, using laboratory-based diffraction data, we describe the structure of the disulfide form of the rNTD active site.

3.3 Results

Background.

In preliminary work, two data sets from crystals of rNTD were collected at synchrotron sources. These data sets, at 2.1 and 2.8 Å resolution, were easily solved by molecular replacement. One crystal was in space group $P2_12_12_1$ and the other was space group $P4_12_12$, but both showed a similar active site structure as was seen in the intact AhpF structure [119]: that is, the active site Cys residues did not form a disulfide, but appeared to be in a close, non-bonded interaction (near 3 Å separation). Being surprised again that the disulfide was reduced despite the lack of reducing agent in the purification and crystallization buffers, we biochemically assessed the oxidation state of purified NTD using a thiol-sensitive assay. Quantification of free thiol levels with DTNB demonstrated that the protein used for crystallization began in the oxidized state (0.05 moles of reactive thiol per mole of rNTD as purified vs. 2.21 thiols per mole of DTT reduced rNTD). This led us to conjecture that the disulfide was being reduced during synchrotron data collection, as has been seen for some other proteins [88; 120]. To test this hypothesis, and if possible, determine a structure of the unperturbed oxidized NTD, we selected a single

large crystal with the $P4_12_12$ space group (2 molecules/asymmetric unit) and collected two data sets: first one from our laboratory x-ray source and then one at a synchrotron.

Structure determinations and overall structure.

The refinements against both the LAB (2.3 Å resolution) and SYNC (2.4 Å resolution) data behaved well and led to structures with an expected accuracy for well ordered parts of the protein of ~0.3 Å.[121] Consistent with this expected coordinate accuracy, the LAB and SYNC structures are very similar to one another, with C_α rms deviations of 0.2 Å for chains A_{LAB} vs. A_{SYNC} and B_{LAB} vs. B_{SYNC}. In contrast, comparisons of NTD chains in different crystal environments, chain A versus chain B and chains A and B versus the NTD as seen in intact AhpF, differed by 0.5 Å. Overall, no significant differences are observed between the isolated rNTD and intact AhpF crystal structures (Figure 3.1) so the structural descriptions of Wood et al.[119] are relevant. For simplicity, the discussion and the figures refer to molecule A from the LAB and SYNC data sets, but the results hold for molecule B also.

Oxidation state of active site cysteines in the crystal structures. The structure determined from the LAB data set unambiguously revealed cysteines 129 and 132 to be in a disulfide bond (Figure 3.2). Confirmation of the oxidized state came from two trial refinements; in the first case, cysteines 129 and 132 were mutated to alanine and in the second case, the $S\gamma$ sulfurs of cysteines 129 and 132 were refined without van der Waals interactions. The results of both experiments were in agreement with the sulfurs being at a normal covalent disulfide bonding distance (ca. 2.1 Å).

The structure deduced from the SYNC data set, again refined without van der Waals constraints on the active site sulfur atoms, resulted in an electron density distribution and a model that were not consistent with a

disulfide bond. The refined Sγ- Sγ distance near 2.9 Å (Figure 3.2) was very similar to that reported for intact AhpF [119].

Determination of the pK_a for the active site Cys.

To confirm whether the short Sγ- Sγ distances observed in the synchrotron exposed crystals of AhpF[119] and the rNTD were due to a thiol-thiolate interation, we determined the pK_a of the reduced "dithiol" form of the active site. Following the formation of the thiolate ion by absorbance at 240 nm [122; 123; 124; 125], we obtained an apparent pK_a of 5.1 ± 0.4 (Figure 3.3). Two observations suggested that indeed the absorbance change is due to thiolate formation rather than another change in structure first the observation that the absorbance of oxidized (disulfide) rNTD remained constant over the pH range studied [126], and second that the change in extinction coefficient of ca. 6000 $M^{-1}cm^{-1}$ (Figure 3.3) matches that expected for a single thiolate [122].

3.4 Discussion

Disulfide cleavage from synchrotron radiation. The two crystal structures of rNTD reveal an interesting story of radiation-generated cleavage of a disulfide bond. Cleavage of disulfide bonds has been reported to selectively occur when disulfide-containing proteins are exposed to intense radiation [88]. In fact, this phenomenon of disulfide cleavage has been used to purposely generate structures of reduced tryparedoxin, when other attempts had proven unsuccessful [120]. The Sγ-Sγ bond distance increased from 2.05 Å in the oxidized state to 2.8 Å and 3.0 Å in the radiation-generated reduced state. In that case, reduction required prolonged x-ray exposures; accompanying the reduction of the disulfide bond, there were also decreases in diffraction strength indicating that general radiation damage to the crystal had also occurred.[88; 120] In contrast, the reduction of the rNTD disulfide was

much more rapid, and without evidence of general radiation damage. It occurred so rapidly, that a single 15 min data set behaves as if the protein was fully reduced. These observations indicate that the disulfide bond of rNTD is exquisitely sensitive to radiation cleavage and will be a useful model system for studying this process. Although we cannot recreate the radiation doses used for the structure solution of AhpF, this disulfide cleavage also occurred during the collection of a single data set consistent with it being similarly sensitive [119].

The oxidized structure of the NTD.

The structure solved from the rNTD LAB data set represents the first crystal structure of the oxidized form of this unusual domain. The AhpF crystals analyzed by Wood et al.[119] were not large enough to be analyzed using a laboratory source, but it was our good fortune that the size and order of the rNTD crystals did support such an analysis. Compared to the reduced form [119], the oxidized rNTD redox center shows only minor structural changes confined to the immediate vicinity of the disulfide bond. The only consistent and significant movement is the small rotation of the Cys129-χ torsion angle needed to form the disulfide. In one of the two monomers (chain A), there is also a shift of a His130-χ to a different rotomer, but this side chain is very disordered already. The small differences between the reduced and oxidized rNTD structures are consistent with what has been seen for thioredoxin.[127]

The oxidized rNTD is the redox form that is attacked by one of the Cys residues in the thioredoxin reductase-like portion of AhpF which initiates the thiol-disulfide interchange reaction resulting in NTD reduction [57; 119]. Two further structures needed to complete a structural view of the catalytic cycle of the NTD are the mixed disulfides it forms when it is being reduced by the thioredoxin reductase-like part of AhpF and when it is passing reducing equivalents to AhpC. We have been able to covalently trap both of these

mixed disulfide complexes, one via the generation of a C132S/C348S double mutant of AhpF [128], and the second with two single mutants, C132S AhpF and C46S of AhpC.[129] We are working to crystallize these constructs.

The NTD pK_a and thiol-thiolate hydrogen bonding.

As seen in the full length AhpF structure [119], the two cysteinyl residues (Cys129,Cys132) are involved in a close, ca. 3 Å, non-covalent interaction. Wood et al.[119] presented compelling arguments that this is a thiol-thiolate interaction, and now the measurement of a pK_a of 5.1 ± 0.4 for one of the active-site Cys residues confirms that one Cys would be expected to be mostly deprotonated (i.e. in a thiolate form) both in the rNTD crystals studied here, which are at pH = 8.4, and in the original AhpF crystals, that were at pH = 5.6. Although we have no direct evidence as to which Cys is being titrated, the geometry of the active site (see discussion in Wood et al. [119]), and analogy with thioredoxin and related proteins contatining the –C-X-X-C- motif both lead to the expectation that the low pK_a belongs to the Cys129, the more N-terminal and exposed Cys that attacks disulfide substrates [128].

This low pK_a is not unprecedented for thioredoxin-fold proteins, as the pK_a of *E. coli* DsbA is as low as ~3.2 [126; 130], but it is lower than the pK_a's of other Prx-reducing domains/proteins. Other reductants of Prxs such as *E. coli* Trx and *Trypanosoma brucei* tryparedoxin (Txn) have reported pK_a's around 7.0 [131; 132; 133; 134]. Thus, for all of these Trx-like –Cys-X-X-Cys- containing proteins, the pK_a of the more N-terminal Cys thiol is shifted significantly below the value of ~8.3 for an unperturbed Cys thiol in solution, but the specific values cover a wide range between 3.2 and 7.2. While the thiol-thiolate hydrogen bond exerts an important influence on this residue's pK_a, (e.g. Jeng et al. 1995; Mössner et al. 2000)[132; 135], most or all proteins in this group are thought to have such an interaction [127; 136; 137], so this cannot be the distinctive feature. Additional contributing factors documented in the literature are

structure-related effects including hydrogen bonding and electrostatic interactions [135; 138; 139]. For Trx-fold proteins, numerous studies have used mutations to study the role of the residues present between the two Cys residues in the –Cys-X-X-Cys- motif [125; 130; 138; 140; 141; 142; 143]. An important insight synthesizing many observations was that the pK_a of the N-terminal Cys appears largely determined by the number of hydrogen bonds that the –X-X-Cys residues provide to stabilize the thiolate [139; 144], with proteins having four, three, and two hydrogen bonds to the thiolate showing pK_a's of ~3 (e.g. DsbA), ~5 (e.g. Grx3), and ~7 (e.g. Trx). The NTD fits this generalization as it has three hydrogen bonds (from the Cys132 thiol, and the backbone amides of residues 131 and 132). In the NTD, the nearest positively charged side chains, His131 and Arg185, cannot approach Cys129 to form a hydrogen bond without rearrangements in backbone structure. As has been done for other Trx-like proteins [125; 130; 138; 143], this explanation for modulation of the pK_a could be tested by mutation of position 131 to His to add a fourth hydrogen bond and match the DsbA sequence or to Pro to remove a hydrogen bond and match the Trx sequence. Still, additional factors such as protein dynamics [139] and global electrostatics [145] also contribute to the active site properties, as some Trx family members with common dipeptide sequences but from different organisms exhibit considerably different pK_a values (e.g. Nelson and Creighton 1994; Ruddock et al. 1996)[126; 146].

Finally, a surprising result is that the pK_a of ca. 5.1 ± 0.4 for the NTD does not fit with the free energy correlation between the N-terminal Cys pK_a values and the redox potentials that has been demonstrated empirically for a number of Trx family members.[130; 135; 143; 147] Trx and Txn exhibit quite low redox potentials at pH 7.0 (E_o') of -270 and -249 mV, consistent with their highly reducing nature and relatively high pK_a's of ~7.[134; 135] The redox potential E_o' of -264 ± 8 mV [118] and function of the NTD are quite similar to these other redox donors, but the pK_a for Cys129 in the NTD, at ca. 5.1 ± 0.4, is not. In this regard, characterization of the mutants of the –Cys-X-X-Cys-

motif suggested above will be a useful first step to probe this unusual property of the NTD, and will reveal whether a group of NTD mutants will have a pK_a-to-redox potential relationship that is shifted but with the same slope as seen for other Trx proteins, or whether it has a different slope. Either way, because of its unusual properties, further work on the NTD promises to yield new insights into the factors governing the relationship between the pK_a's and redox potentials of the Trx family proteins.

3.5 Materials and Methods

Purification of rNTD.

The separately-expressed rNTD of AhpF, also known as F[1-202], was purified as previously described [117] from a 10 L fermentor growth by sequential chromatography on Q sepharose HP and Superose 12 columns using an Äkta Explorer 10S FPLC instrument (Amersham Biosciences**)**. For crystallization, rNTD was stored at 22.7 mg/mL in 25 mM potassium phosphate buffer, pH 7.0, containing 1 mM EDTA. rNTD concentration was assessed using an ε_{279}= 15 100 M^{-1} cm^{-1} [117].

Thiol quantification.

Thiols were quantified via reaction with DTNB [5,5'-dithio-*bis*-(2-nitrobenzoic acid), Ellman's reagent] as described previously [52]. Briefly, the free thiol groups within the oxidized and dithiothreitol- (DTT-) reduced rNTD protein were measured at pH 7.0 by the addition of 150 μM DTNB in the presence or absence of 4 M guanidine hydrochloride (denaturing or non-denaturing conditions, respectively) followed by detection of the TNB produced at 412 nm 14150 M^{-1} cm^{-1} [148] on a thermostated Milton Roy Spectronic 3000 diode array spectrophotometer.

Crystallization.

Rod-like crystals (ca. 1 x 0.2 x 0.2 mm^3) were grown at room temperature in about 3 weeks using a reservoir of 0.2 M ammonium acetate, 0.1 M Tris pH 8.4, 30-35% polyethylene glycol 4000, and a drop made from 2 μL of rNTD storage solution mixed with 2 μL of the reservoir solution. Most crystals had splayed ends but a few were single. For data collection, crystals were scooped into cryoloops through a mineral oil monolayer and immediately flash-frozen by plunging into liquid nitrogen.

Data collection and Refinement.

Two data sets were collected at –170 °C from a single rNTD crystal. Various parts of the crystal had variable diffraction quality and for each data set we attempted to find an optimal volume of the crystal through trial exposures. The first data set (LAB) was collected on an R-axis IV image plate detector (Molecular Structure Corp.) with a Rigaku RUH3R rotating anode (CuK_α) operating at 50 kV and 100 mA with a 0.3-mm collimator. The crystal was recovered and stored in liquid nitrogen until 8 weeks later when the second data set (SYNC) was collected at beamline 5.0.3 of the Advanced Light Source (Lawrence-Berkeley National Laboratory, USA) in two passes. The first pass included 50° of data (15 s per 1° frame; λ= 1.01 Å), and to avoid saturation of the lower resolution reflections, a second 45° of data were collected more rapidly (3 s per 1° frame). X-ray data were processed using programs DENZO and SCALEPACK [149] and the LAB and SYNC data each have reasonable statistics extending to 2.3 Å and 2.4 Å respectively (Table 1). We speculate that the slightly poorer resolution limit of the synchrotron data was limited by the intrinsic order of the volume of the crystal used. The crystals belong to the tetragonal space group $P4_12_12$ with two molecules in the

asymmetric unit and 56% solvent. A random 10% of the data were selected for cross validation.

The structure of NTD was solved by molecular replacement using the CNS suite of programs (v1.1) [150] and a search model based on the N-terminal domain (residues 1-196) from the structure of AhpF (PDB code 1HYU) [119]. Two molecules were unambiguously placed using data from 50.0 to 4.0 Å resolution, and rigid body refinement led to R and R_{free} values of 0.330 and 0.329, respectively. Positional and B-factor refinement from 50.0 to 2.3 Å resolution, rapidly dropped the R-factors to R= 0.267 and R_{free}= 0.299. Manual rebuilding of the model into $2F_O - F_C$ and $F_O - F_C$ electron density maps was done using program O [103]. Only small modifications of side chains were necessary. Waters were added both manually and using the CNS utility Water-Pick with the following criteria: (1) a minimum 3σ peak in $2F_O - F_C$ maps and (2) a minimum distance of 2.6 Å and a maximum distance of 3.5 Å to potential hydrogen-bond donor or acceptor. To allow for unbiased determination of the Cys129 and Cys132 positions, the van der Waals interactions for the sulfurs were turned off by use of an “IGROUP” statement in the minimization input file for CNS. In a separate control refinement, Cys129 and Cys132 were mutated to alanine to remove model bias. Refinements were considered complete when the largest difference map peaks were not interpretable and R and R_{free} had converged. Refinement using the SYNC data set was done starting with the final model from the LAB data set including waters. After one round of positional and B-factor refinement from 50.0 to 2.4 Å, R and R_{free} were 0.221 and 0.267, respectively. Two additional rounds of manual rebuilding and positional and B-factor refinement completed the refinement. Final statistics of both models are reported in Table 3.1.

Cysteine pK_a determination.

The thiolate anion was directly monitored at 240 nm (using a Shimadzu UV-2401PC UV-Vis spectrophotometer) as previously described by Kortemme et. Al.[125]. All measurements were carried out at 25 °C in buffer A: 1 mM each sodium citrate (pK_a = 3.13, 4.76, and 6.40), sodium borate (pK_a = 9.24), and sodium phosphate (pK_a = 2.15, 7.20, and 12.38), with 200 mM NaCl. Reduced NTD was prepared by incubation with 0.1 M Tris-HCl, 5 mM DTT, pH 7.4 for 15 min at room temperature. After incubation, the DTT was removed by a 1000-fold dilution into buffer-A at the appropriate pH by three successive 10-fold dilutions and concentration using Centricon concentrators (Millipore, 5 kDa cutoff) buffer without protein was used to control for residual DTT which had an absorbance of less than 0.001 at the wavelengths measured. Protein concentrations were between 10-15 μM. As a control the absorbance at 240 nm for the NTD in the disulfide form was measured over the same pH range. All measurements were carried out in triplicate.

3.6 Acknowledgements

This publication was made possible in part by the Environmental Health Sciences Center's Molecular Structure and Interactions Facilities core supported by grant number P30 ES00210 from the National Institute of Environmental Health Sciences, NIH. We thank Rick Faber and Sarma Ganapathy for all their help and support. This research was supported by a grant (RO1 GM50389) from the National Institutes of Health to L.B.P. and P.A.K and grant ES00040 from the National Institute of Environmental Health Sciences to Joe S. Beckman.

3.7 Abbreviations

AhpF, alkyl hydroperoxide reductase flavoprotein or NADH:peroxiredoxin oxidoreductase; NTD, N-terminal domain of AhpF; rNTD, recombinant NTD; DTT, 1,4-dithiothreitol; DTNB, 5,5'-dithio-*bis*-(2-nitrobenzoic acid); TNB, 2-nitro-5-thiobenzoate

Figure 3.1

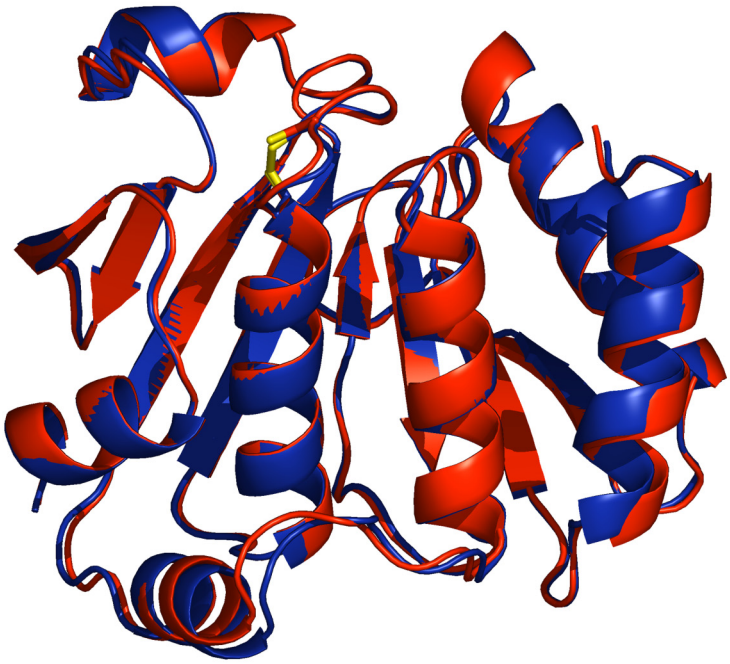

Figure 3.1. Comparison of rNTD with the N-terminal domain of AhpF. The backbones of rNTD (blue) and the N-terminal domain of AhpF (red) are represented as a ribbon; the bonds of the redox center (Cys129-Cys132) are depicted as sticks. The rmsd for the overlay is 0.5 Å for 196 Cα atoms. The figure was generated using Pymol.[107]

Figure 3.2

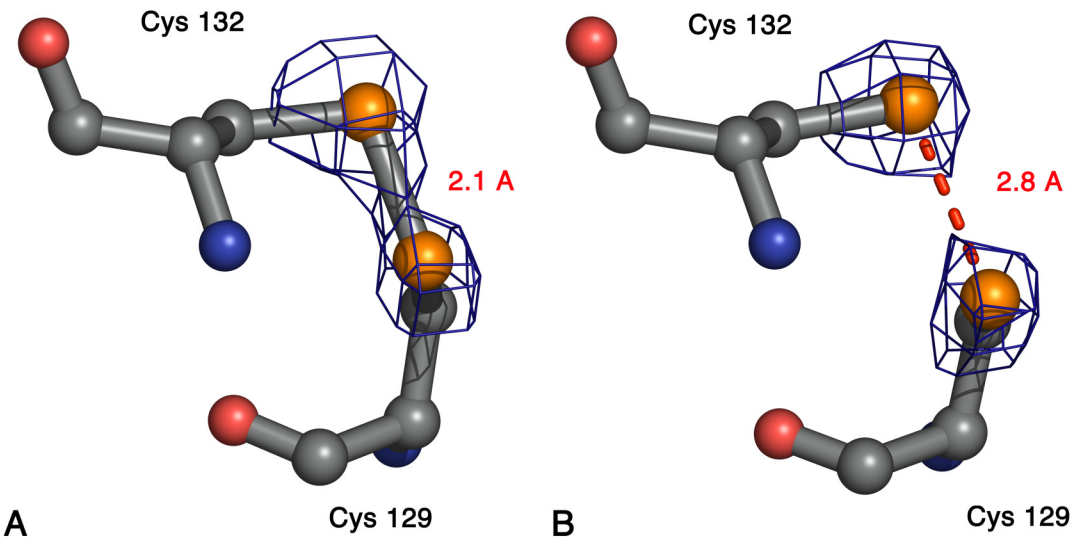

Figure 3.2. Reduction of the NTD redox-active disulfide center by synchrotron radiation. (A)The active site Cys-Xaa-Xaa-Cys of rNTD in its electron density based on the LAB data set, and (B) the equivalent image based on the SYNC data set. The electron density in both panels is contoured at 3.5 Å, and the Sγ-Sγ distances are given. The figure was generated using Pymol.[107]

Figure 3.3

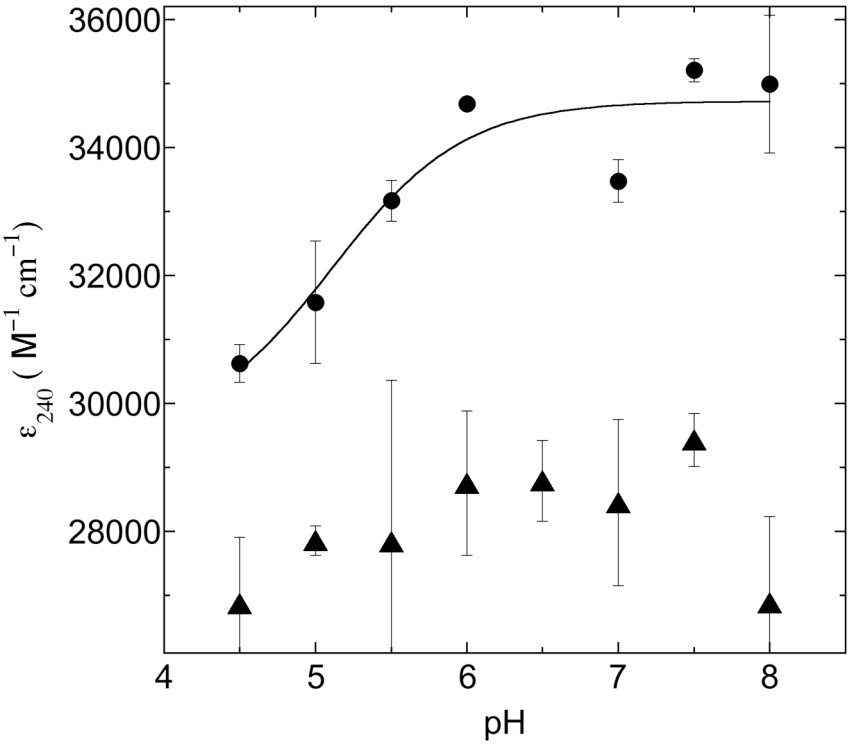

Figure 3.3. Apparent pK_a determination of the active site Cys129 thiol(ate). Absorbance values at 240 nm of reduced (circles) and oxidized (triangles) rNTD proteins were determined over the pH range of 4.5 to 8 as described in Methods. The difference in ε_{240nm} between the reduced and oxidized (average oxidized ε_{240nm} 28,100 $M^{-1}cm^{-1}$) protein was about 6000 $M^{-1}cm^{-1}$ which is in the range of 4000-6000 $M^{-1}cm^{-1}$ that is expected for the titration of a single thiol group [122]. Data points were fit to the equation:

$$y = \frac{\left(A \times 10^{x}\right) + \left(B \times 10^{\mathrm{pK_a}}\right)}{10^{x} + 10^{\mathrm{pK_a}}}$$

In this equation, x is the pH value and y the corresponding absorbance value, and A and B are allowed to vary and represent the upper and lower absorbances of the titration data, respectively. Final values from the fit using Kaleidagraph (Synergy Software) were 5.1 ± 0.4, 34,700 ± 400 and 29,500 ± 1500 for pK_a, A and B, respectively.

Table 3.1. Data collection and refinement statistics for NTD

	LAB	SYNC
Resolution limits (Å)	50-2.3 (2.38-2.3)	50-2.4 (2.49-2.4)
Space group	$P4_12_12$	$P4_12_12$
Unit cell(Å)	a = 85.41	a = 85.27
	b = c = 108.60	b = c = 107.94
Data collection		
Unique observations	22423	19094
Multiplicity	6.5 (6.5)	5.7 (3.2)
Average I/σ	16.2 (2.7)	12.2 (1.6)
R_{meas} (%)	7.2 (46.1)	9.2(51.9)
$R_{mergd\text{-}F}$ (%)	7.7 (35.3)	9.6(53.7)
Completeness (%)	99.7 (99.5)	98.7 (97.5)
Refinement		
No. of protein molecules	2	2
No. of amino acid residues	392	392
Average B-factor ($Å^2$)	45	44
Non-hydrogen protein atoms	3042	3042
R-Factor	0.199 (0.262)	0.206 (0.298)
Free R-factor (10% of data)	0.256 (0.325)	0.261 (0.343)
r.m.s.d. bond lengths (Å)	0.010	0.006
r.m.s.d. bond angles(°)	1.41	1.20

[a.] Numbers in parentheses correspond to values in the highest resolution shell

Chapter 4

Exploring the Reactions of Peroxynitrite with Green Fluorescent Protein

Blaine R. Roberts, Emily Clark, Chris Holguin, Joseph S. Beckman

Formatted for publication

4.1 Abstract

Green fluorescent protein (GFP) is a widely used molecular marker for gene expression, gene product location, and has been reengineered to monitor intracellular halides, metals and pH. GFP fluorescence is dependent on the spontaneous oxidation and cyclization of Ser^{65} (or Thr^{65}) –Tyr^{66}-Gly^{67} that produces a fluorophore rigidly bound within an 11-stranded ß-barrel. Because GFP fluorescence requires Tyr^{66}, Espey et al. [Espey, M. G., Xavier, S., Thomas, D. D., Miranda, K. M. and Wink, D. A. 2002. *Proc Natl Acad Sci U S A* **99**: 3481-6] proposed that the loss of fluorescence of GFP could be useful to monitor protein nitration in vitro and in vivo. Based on the loss of fluorescence upon addition of peroxynitrite to cells, they concluded that peroxynitrite did not cross cell membranes to nitrate proteins. Here, we further investigate the loss in fluorescence by peroxynitrite and its utility as an intracellular marker for protein nitration. Purified recombinant GFP exposed to peroxynitrite showed a concentration-dependent loss of fluorescence correlating with a modest susceptibility to nitration as determined by western blot analysis. However, no evidence was found for the nitration of the fluorophore Tyr^{66} as determined by difference absorbance spectroscopy. Although U-87 cells expressing α-actinin fused with GFP showed less than a 5% decrease in fluorescence after a 100 μM treatment with bolus additions of synthetic peroxynitrite, western blot analysis of cellular lysates for 3-nitrotyrosine reveals abundant nitration of multiple cellular proteins. Our results suggest that the oxidation by peroxynitrite of an amino acid other than tyrosine may be responsible for the loss of fluorescence by GFP and this oxidation is relatively insensitive compared to oxidation of other proteins, making GFP an ineffective indicator of intracellular protein nitration.

4.2 Introduction

Nitrotyrosine is found in a multitude of disease states such as ischemic reperfusion, atherosclerosis, neurodegenerative diseases and severe inflammation. [151; 152; 153; 154] As a biomarker, nitrotyrosine has biological and clinical importance because levels of nitrotyrosine correlate with disease risk and nitration of tyrosine affects protein function. [155; 156] In vivo, the nitration of tyrosine is indicative of aberrant free radical chemistry, resulting from the production of the reactive nitrogen species peroxynitrite ($ONOO^-$) and nitrogen dioxide ($\bullet NO_2$). The powerful oxidant peroxynitrite is formed by the diffusion controlled reaction of nitric oxide ($\bullet NO$) with superoxide ($O_2^{\bullet -}$; rate ~10^{10} $M^{-1}\bullet s^{-1}$).[157] Nitrogen dioxide is produced from essentially two sources – one involves the homolytic cleavage of O-O bond of peroxynitrite catalyzed by the Lewis acids H^+, CO_2 or transition metal centers.[158; 159] Alternatively, $\bullet NO_2$ is generated by heme-containing enzymes such as myeloperoxidase and horseradish peroxidase, which both use hydrogen peroxide and nitrite as substrates to produce $\bullet NO_2$.[160; 161]

Peroxynitrite does not react directly with tyrosine to form nitrotyrosine.[159] Rather, the nitration of tyrosine is generally thought to be a two-step process first requiring a 1 e^- oxidation to produce a tyrosyl radical. Carbonate radical ($CO_3^{\bullet -}$), nitrogen dioxide, oxo-metal species (M^n=O) such as oxoferryl (Fe^{+4}=O) and to a lesser extent hydroxyl radical ($\bullet OH$) are the oxidants that lead to the formation of the tyrosyl radical. Once the tyrosyl radical is formed, the near diffusion-controlled coupling of the tyrosyl radical with $\bullet NO_2$ completes the nitration of tyrosine. Fortuitously, the homolysis of the O-O bond of peroxynitrite is catalyzed most efficiently by CO_2 and more slowly by H^+, yielding the powerful oxidizing radicals $\bullet OH$ or $CO_3^{\bullet -}$ and $\bullet NO_2$, which appear to mediate tyrosine nitration. Nitration is about 8-14% efficient due to diffusion and alternative reactions of the nitrating species such as the reduction of $\bullet NO_2$ to nitrite. In addition, the antioxidants such as glutathione

and urate present in vivo will further scavenge these radical intermediates responsible for the nitration of tyrosine.[162; 163] Current techniques and the low yield of nitrotyrosine in vivo limit the real-time detection of nitration.

Intracellular detection of nitration in real time could yield new information about the processes generating reactive nitrogen intermediates *in vivo.* Furthermore, the ability to detect reactive nitrogen species in vivo would aid in testing the efficacy of therapeutic treatments in many disease processes. Espey et al.[66] proposed that the intracellular expression of GFP is well suited for the detection of nitration in vivo because of the requirement of Tyr[66] for the fluorescence of GFP.

The green fluorescent protein (GFP) from the jellyfish *Aequorea Victoria* and its mutant derivatives of GFP have proved to be superbly useful tools in cell biology and biotechnology.[164; 165; 166; 167] GFP consists of 238 amino acids that fold into an 11-stranded β-barrel wrapped around an α-helix that contains residues Ser65-Tyr66-Gly67. As the native protein folds, residues 65, 66 and 67 undergo spontaneous cyclization and oxidation, which yields the chromophore required for GFP fluorescence (Figure 4.1).[168] The chromophore outside of the interior of the GFP β-barrel is not fluorescent. [169] Likewise, the fluorescence of GFP is lost when the protein is denatured.[69; 170] Deletion mapping experiments have shown that nearly all 238 amino acids (2-232 and 7-229) are required for chromophore formation and fluorescence, emphasizing the functional influence that nearly every residue has on the fluorescence of GFP. [171; 172] The sensitivity of the choromphore to its local environment has been exploited by genetically engineering GFP to produce intracellular probes of pH, Ca^{2+}, nitrate, halide concentrations and metal concentration.[173; 174; 175; 176] Espey et al. demonstrated that peroxynitrite can decrease the fluorescence of purified GFP and suggested that nitration of the chromophore was responsible for the loss in GFP fluorescence.[66] However, the sites of oxidative modifications that result in the loss of GFP fluorescence were not determined.

In this study, we investigated whether the loss in GFP fluorescence was due to nitration of the GFP chromophore. In addition, we investigated if GFP fluorescence was sufficiently sensitive to detect nitrating species in the presence of alternative oxidation targets, such as bovine serum albumin.

4.3 Results

Repeated additions of 5 μM peroxynitrite decreased the fluorescence of wild-type GFP with 21 ± 0.7 μM required to inhibit the fluorescence signal by 50 % (Figure 4.2). The nitration of GFP was assed using a polyclonal antibody specific for 3-nitrotyrosine. By Western blot analysis, the nitration of GFP only became visible after the total addition of 20 μM peroxynitrite, a concentration which decreased fluorescence of GFP by 50% (Figure 4.3 A). In contrast, the polyclonal antibody was readily able to detect nitration of bovine serum albumin (BSA) from a BSA and GFP mixture that had been treated with only 5 μM peroxynitrite (Figure 4.3 B). For these experiments, one half the concentration of BSA compared to GFP was used, because it contains 21 tyrosine residues as compared to 10 in GFP. When equivalent concentrations of BSA, based on tyrosine content, was added to GFP solutions 50 μM peroxynitrite was required to decrease fluorescence by 50% (Figure 4.3 B). And similar to the nitration of GFP alone, the formation of nitrated GFP became visible after the fluorescence of GFP had decreased by ~50 % (Figure 4.3 B). These data suggest that oxidation of an amino acid other than tyrosine is likely to be responsible for the loss of fluorescence of GFP.

During the maturation of GFP, Tyr66 undergoes a cyclization and oxidation to yield the chropmophore. The modifications to Tyr66 may be extensive enough to prevent the nitrotyrosine antibodies from recognizing the nitrated form of Tyr66. Therefore, we used difference spectroscopy to evaluate whether the GFP chromophore was susceptible to nitration. The chromophore of mature GFP under native conditions has characteristic absorbance

maximums at 395 nm and 475 nm. Upon the denaturation of GFP with urea the absorbance maximums shift 380 nm and 450 nm (Figure 4.4 B). The difference spectrum of native GFP treated with successive 100 μM bolus additions of peroxynitrite revealed two absorbance peaks at 360 and 430 nm (Figure 4.4 A), which are characteristic of the absorbance of 3-nitrotyrosine (λ_{max}= 360nm and 428 nm), the absorption of the GFP chromophore was unchanged with peroxynitrite treatment. When GFP was denatured in urea and then treated with 100-400 μM peroxynitrite, the difference spectra of the GFP chromophore decreased at 385 nm and 460 nm consistent with a modification of Tyr66 (Figure 4.4 B). Larger concentrations of peroxynitrite did not further modify the chromophore of denatured GFP, but additional spectral changes occurred that were consistent with nitration of other tyrosines.

The sites of modification were investigated by tandem mass spectrometry using both Maldi and electrospray ionization methods. MS/MS of samples of GFP treated with a total of 100 μM in successive 5 μM bolus additions of peroxynitrite showed nitration of tyrosine residues 182 and 200. We also identified a peptide containing the only tryptophan (W57) in GFP although we did not identify any oxidative modifications of W57. Typically sequence coverage was 15-30% despite using two different ionization sources and 5 different digestion procedures. GFP is known to remarkable resistant to proteolysis.[177]

U87 glioma cells expressing a GFP-α-actinin fusion protein were used to determine if the loss of GFP fluorescence could be used assess the diffusion of peroxynitrite across cellular membranes. The treatment of cells with up to 100 μM peroxynitrite produced <3% decrease in GFP fluorescence (Figure 4.5 A). A western blot for nitrotyrosine prepared from the soluble fraction of the cellular lysates from peroxynitrite-treated U87-GFP-α-actinin cells, revealed that many proteins were immunoreactive for nitrotyrosine (Figure 4.5 B).

4.4 Discussion

Espey et al. reported that intracellular GFP fluorescence was unaffected by bolus additions of peroxynitrite, and concluded peroxynitrite was unable to cross cellular membranes to nitrate proteins.[66] This conclusion is at odds with previous literature showing that peroxynitrite can traverse biological membranes as well as mediate the nitration of intracellular proteins.[178] Even mitochondrial matrix proteins such as manganese SOD are modified by peroxynitrite added extracellularly, showing peroxynitrite can traverse as many as three membranes. Our western blot analysis for nitrotyrosine of the cellular lysates of GFP-expressing cells treated with 100 μM peroxynitrite (Figure 4.5 B) confirmed that peroxynitrite was nitrating proteins without changing the fluorescence of GFP.

The insensitivity of GFP fluorescence to intracellular nitration is likely due to two factors: the low level of GFP expression relative to the total protein content of the cell, and the lower susceptibility of GFP to modification, relative to tyrosines in other proteins, by peroxynitrite. For example, the sensitivity of GFP fluorescence to peroxynitrite was effectively attenuated by the addition of bovine serum albumin (BSA). Previous studies have also documented that certain tyrosine residues on the same protein are far more susceptible to nitration.[179] Western blots showed that BSA, which itself is not particularly sensitive to tyrosine nitration,[41] has a 5-10x greater sensitivity to nitration than GFP. The local environment surrounding a particular tyrosine in a given protein can greatly increase the susceptibility to nitration. [179] [41] Charged residues, such as acidic residues on the carboxy side or arginine on the amino side of tyrosine can increase the susceptibility to nitration in neurofilamant coiled-coil domains.[179] Similarly, the susceptibility of tyrosine to chlorination also depends on the neighboring residues as has been demonstrated for the lipoprotein ApoE.[180] The ability of low concentrations of BSA to diminish the sensitivity of GFP to peroxynitrite suggests that, intracellularly, GFP lacks the

sensitivity necessary to compete with cellular proteins for reactive nitrogen species.

The fluorescence of the GFP chromophore is, however, exquisitely sensitive to the local environment and mutations that expose the chromophore to solvent or shift the hydrogen bonding network of the chromophore either decrease fluorescence or change the excitation and emission properties of GFP.[164] Espey et al. hypothesized that the decrease in GFP fluorescence was due to the nitration of Tyr66-derived chromophore. However, difference spectroscopy established that the nitration of GFP does not affect the chromophore unless GFP had first been denatured with ~ 7 M urea. This suggests that peroxynitrite is likely to affect the fluorescence of GFP by modifying residues on the surface of GFP, which could result in a local perturbation and increased solvent exposure of the chromophore. For example, His148 and Tyr145 are both solvent accessible, making them potential targets for oxidation and nitration. Oxidative modification of His148 or the neighboring Tyr145 would directly affect the fluorescence of GFP as they are both part of a β-bulge that is intimately connected with the chromophore.[181; 182] The mass spectrometry analysis of peptide digests identified nitration of Tyr182, which is located only 4.5 Å (C_α- C_α distance) from Tyr145 on the adjacent β-strand. However, due to low sequence coverage it is not possible to conclude that the nitration of Tyr182 or Tyr200 has any direct affect on the fluorescence of GFP.

Although GFP has proved to be a revolutionary tool to study gene expression in vivo, it appears to be too insensitive for use as an intracellular probe of reactive nitrogen species derived from peroxynitrite (Figure 4.5 A and B). The sensitivity of GFP to nitration would need to be substantially enhanced for GFP to be a useful in vivo marker for nitration. Even if the sensitivity of GFP to nitration was increased by several orders of magnitude, it may still be difficult to achieve high enough expression levels to be able to adequately detect nitration. The assay is complicated because one is attempting to

measure a small decrease in fluorescence of a protein whose level of expression can vary significantly between cells as well as within any cellular compartment. Given this a more useful approach is to develop probes that become fluorescent upon modification by nitration, but this has not been possible because nitration typically quenches fluorescence. In an elegant paper, Ueno et al.[65] demonstrated that nitration generally quenches fluorescence of small fluorescent molecules because the nitro group is a strong electron-withdrawing agent. They constructed a new fluorescent probe NiSPY-1, where the highly fluorescent BoDipy moiety is quenched by electron-donating phenolic ring. The phenolic moiety is readily nitrated by peroxynitrite and no longer quenches fluorescence. Ueno et al. further demonstrated that this new fluorescent probe detects exogenous peroxynitrite added to cells, thus providing a novel and exciting probe for intracellular nitration.[65]

4.5 Materials and Methods

Expression and purification of GFP.

Wild-type GFP was expressed and affinity purified from *E. coli* BL21 as previously described[183] with the following changes. After induction with 1mM IPTG (isopropyl-beta-D-thiogalactopyranoside), the temperature was reduce to 15°C and expression was allowed to proceed for 16 hours before harvesting. The cells were lysed and N-terminal His_6-tagged GFP was affinity-purified using Ni-NTA agarose resin (BioRad). After removal of the N-terminal histidine tag GFP with γ-chymotrypsin, GFP was dialyzed against 20 mM tris, pH 8.0, and then loaded onto a HQ anion exchange column (Biorad) for further purification. GFP was eluted using 1 M NaCl in 20 mM tris, pH 8.0, and GFP-containing fractions were pooled and exhaustively dialyzed into protein 100 mM NaCl, 100 mM phosphate pH 7.4. Purified GFP was concentrate to 10-20 mg/mL using Centricon™ membrane concentrators (5k molecular weight

cutoff, Millipore) and stored at –20°C until needed. Protein concentrations were determined using an ε_{395} = 21,000 $M^{-1}cm^{-1}$ for wtGFP.[184]

Fluorescence spectroscopy.

Fluorescence measurements were made with a dual monchromator fluorometer using a 3 mL quartz cuvette. Excitation and emission scans were preformed on solutions of purified GFP to determine the exitation and emission maxima (wtGFP λ_{ex} = 395 nm λ_{em} = 512 nm). All nitration experiments where carried out at 37°C in a buffered solution consisting of 100 mM sodium phosphate, pH 7.4, 100 mM NaCl and 100 μM diethylenetriamine penta-acetic acid (DTPA). Peroxynitrite was synthezied as previously described using hydrogen peroxide and nitrite.[185] The concentration of peroxynitrite was determined using the extinction coefficient 1710 $M^{-1}cm^{-1}$.[186] Between 5-15 μL of a stock solution of peroxynitrite (typically 2-3 mM) were added in 5 μM or 10 μM increments to a 2.0 mL stirred solution of 300 nM GFP maintained at 37°C. After the addition of peroxynitrite the solution was allowed to stir continuously for 30 sec. before taking a fluorescence measurement. Between additions of peroxynitrite, 20 μL aliquots of the GFP solution were collected for western blot analysis. Fluorescence measurements were corrected for the dilution caused by the addition of peroxynitrite. After completing the titration of peroxynitrite, the pH of the solution was determined using pH strips and in all cases the pH of the solution remained between 7.4 and 8.0.

Detection of nitrotyrosine.

Aliquots of GFP collected during the titration of peroxynitrite were mixed with Laemmli's sodium dodecyl sulfate-loading buffer followed by incubation at 95°C for 5 min. Then, 50 ng of protein was loaded on to a 12.5% SDS gel,

electrophoresis conducted at room temperature and transferred to nitrocellulose membrane with a semidry blotting apparatus. After transfer, the membrane was incubated with 5% non-fat dry milk in phosphate buffered saline pH 7.4 for 1 h at room temperature. The membrane was then probed with a polyclonal rabbit antibody specific for 3-nitrotyrosine (stock concentration 1.5 mg/mL,1:1500; Upstate) for 12-16 hours at 4°C. The blot was then washed 3x with phosphate buffered saline pH 7.4 and then probed with goat anti-rabbit-HRP secondary antibody (1:3000, for 1 hour, Biorad) at room temperature. The blot was then rinsed 3x with phosphate buffered saline and then treated with a chemiluminescent substrate (Pierce, SuperSignal West Pico) followed by exposure to X-ray film (Pierce, CL-Xposure Film).

Difference Spectroscopy.

Spectral scans (200-700nm) using an absorbance-matched pair of quartz cuvettes were taken before each bolus addition of peroxynitrite. Peroxynitrite was added in 100 μM steps to vigorously stirred solutions of GFP maintained at room temperature (20°C). Decomposed peroxynitrite was added to the reference cuvette to correct for dilution effects. Absorbance scans of the samples were taken at the beginning of the titration and after the final addition of peroxynitrite. GFP was denatured by diluting the protein into 8 M urea 100 mM sodium phosphate, pH 7.4, 100 mM NaCl for a final urea concentration of 7.2 M. After dilution the GFP samples were placed in a 60°C water bath for 5 minutes. Solutions were then allowed to cool to room temperature (20°C) and an absorbance scan from 300-600 nm revealed two absorbance maximums at 380 nm and 450 nm confirming GFP had been denatured.[69]

Culture of U87MG glioblastoma cells.

U-87MG glioblastoma cells (ATCC) were cultured and transformed with GFP-α-actinin as previously described.[187; 188] Cells were grown to confluence and harvested using trypsin, then pelleted and washed 3 times with 100 mM NaCl, 100 mM phosphate pH 7.4 buffer containing 50 μM diethylenetriamine penta-acetic acid (DTPA). The cells were resuspended, using the same wash buffer, to a density of $5x10^5$ cells/mL. Two milliliters of cells were transferred to a 3 mL quartz cuvette maintained at 37°C with stirring and then treated with peroxynitrite in 10 μM steps until a total of 100 μM peroxynitrite had been added. The cells were then pelleted by centrifugation at 400 g. The supernatant was then decanted and the cells were lysed by resuspension in doubly distilled water followed by 30 seconds of sonication. The lysate was clarified by centrifugation (5 min, 16,000 g) and 40 μL of clarified cell lysate was electrophoresed using 12.5% SDS-polyacrylimide gel and then transfer to nitrocellulose membranes. Immunodetection for nitrotyrosine was then preformed. Protein loading was assed by electrophoresing a duplicate amount of cell lysate on a 12.5% SDS-polyacrylimide gel followed by staining with coomassie brilliant blue R-250.

Pepsin digest of GFP.

The pH of a 50 μL aliquot of GFP (300 nM) that had been treated with 100 μM peroxynitrite (as described above under fluorescence spectroscopy) was adjusted using 50 μL 1.0 M phosphate buffer pH 1.8. The digest was preformed by incubating 3 mg of pepsin from porcine gastric mucosa, cross-linked to agarose (30-70 units/mg, Sigma) for 2-3 minutes at room temperature. After incubation, the pepsin-agarose beads were pelleted by centrifugation (20 s at 5000g) and the supernatant was removed and retained. The supernatant was then immediately desalted using a C_{18}-Ziptip (Millipore)

following the manufactures instructions. Mass spectrometric data was interpreted with the aid of the search engine Mascot (www.matrixscience.com). All peptides identified using mascot were confirmed by manually inspecting the MS/MS data for each peptide.

Figure 4.1

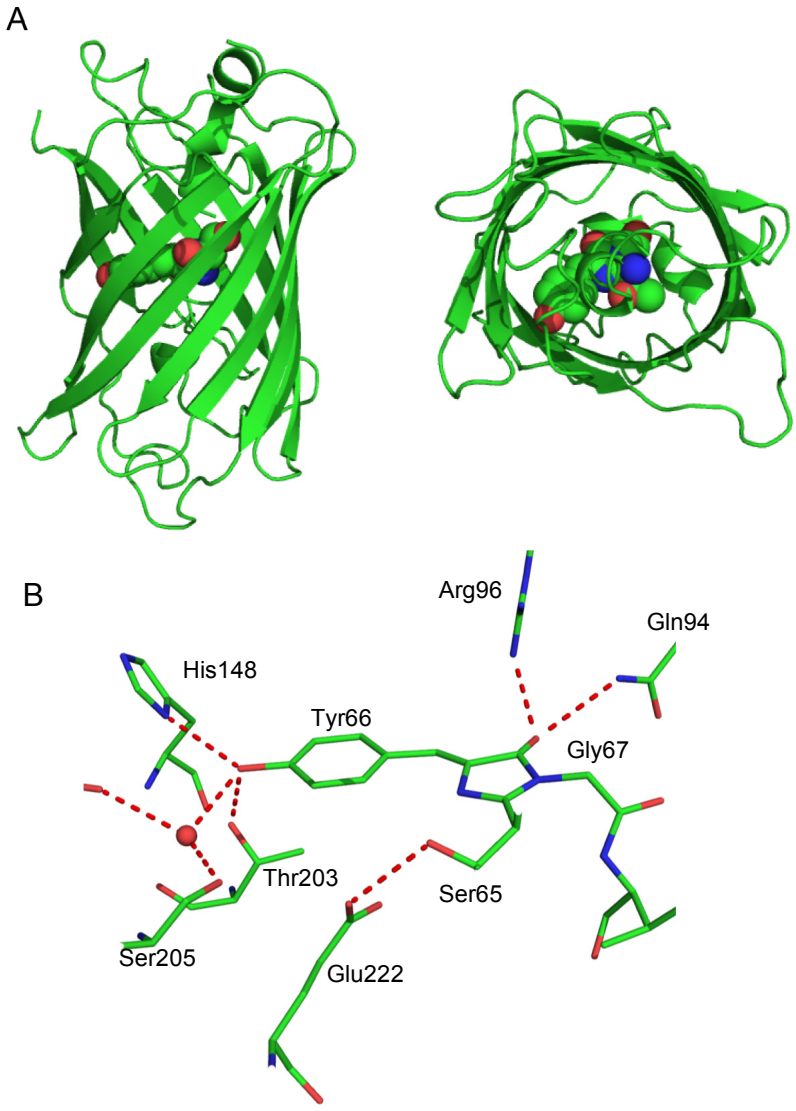

Figure 4.1.The structure of GFP and the fluorescent chromophore (pdb code 1EMA)[189]. (A) A ribbon diagram of the structure of GFP viewed from the side and looking down through the β-barrel. The spheres illistrate the position of the chromophore in the β-barrel (green=carbon, red=oxygen, blue=nitrogen). (B) Shown is the chromophore of GFP (S65-Y66-G67) the neighboring residues and water (red sphere) that make hydrogen bonds (red dashes) to the chromophore. The figure was generated using Pymol.[107]

Figure 4.2

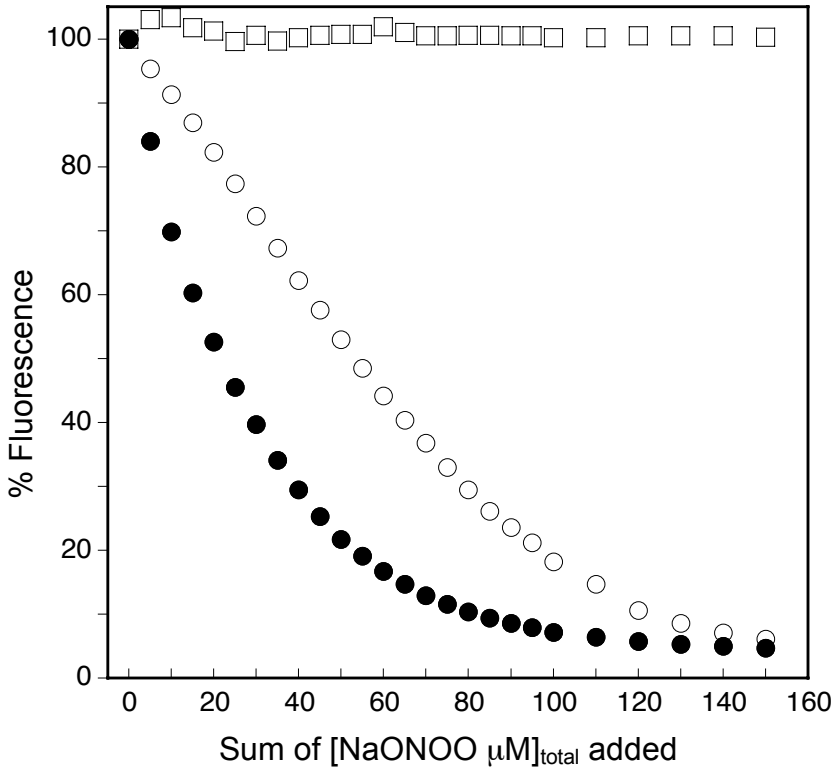

Figure 4.2 Sensitivity of GFP fluorescence to peroxynitrite. Shown is the decrease in the fluorescence of GFP (300 nM) exposed to 5 μM bolus additions of peroxynitrite (closed circles) at 37°C, pH 7.4, with stirring (IC_{50} = 20.7 μM). Mixing bovine serum albumin (150 nM) to a solution of GFP (300 nM; open circles) attenuated the decrease in GFP fluorescence caused by peroxynitrite (IC_{50} = 52.7 μM). The addition of decomposed peroxynitrite (open squares) did not cause a change in the fluorescence intensity of GFP. The resulting fluorescence data was fit to a single exponential decay with a nonzero offset (solid lines) using the program Kaleidagraph (Synergy Software).

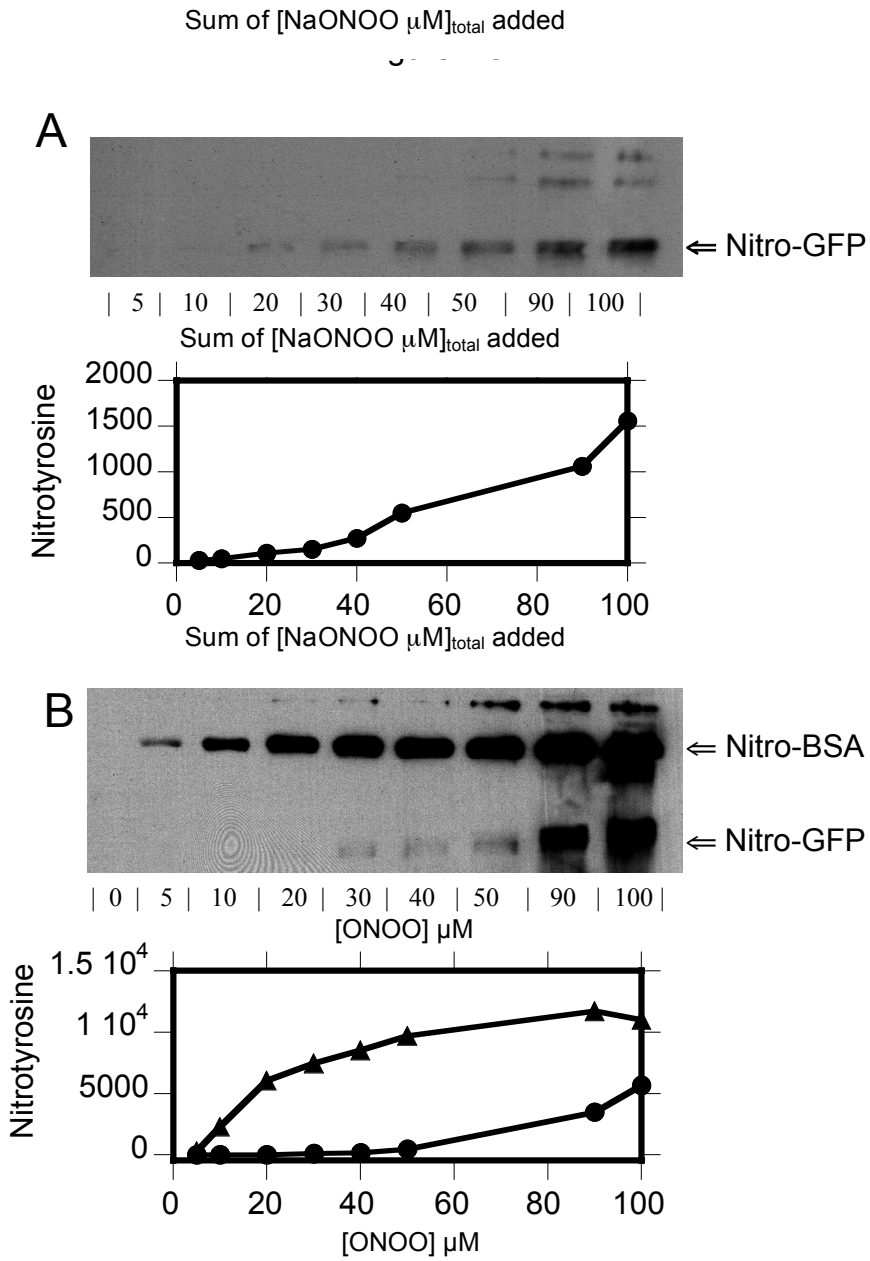

Figure 4.3.

Detection of nitrated GFP using a polyclonal antibody to nitrotyrosine. (A) GFP treated with increasing concentrations of peroxynitrite showed increased immunoreactivity for nitrotyrosine as determined by western blot analysis. Nitration of GFP became evident after the addition of 20 μM peroxynitrite. (B) Western blot analysis for nitrotyrosine of GFP +BSA samples treated with peroxynitrite. Nitration of BSA was immediately detectable after the first addition of peroxynitrite. Immunoreactiveity for the nitration of GFP became evident after the addition of 30 μM peroxynitrite. Below each western blot is the densitometry of the bands that correspond to nitrated GFP (filled circles) or nitrated BSA (filled trangles).

Figure 4.4

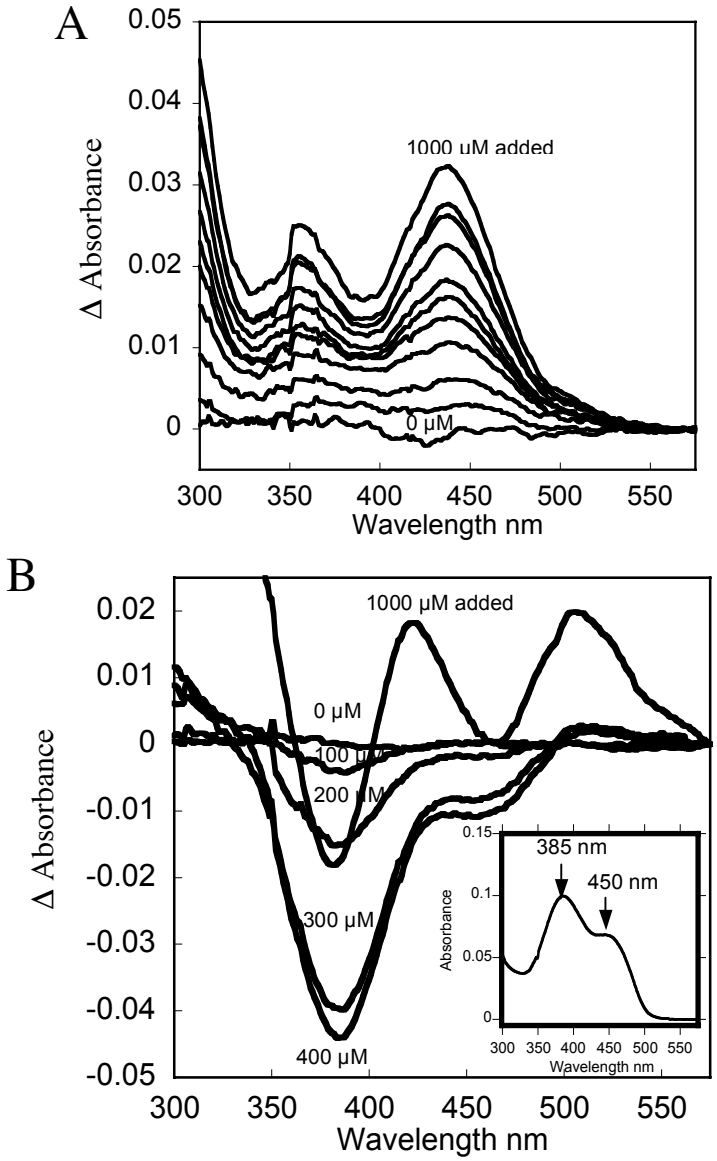

Figure 4.4. Difference spectra of denatured or native GFP treated with peroxynitrite. (A) Shown is the change in difference spectrum of native GFP treated with successive addition of 100 μM peroxynitrite. The two peaks shown have absorbance maximum at 355 nm and 436 nm consistent with the formation of nitrotyrosine. (B) The treatment of urea denatured GFP with 100 μM additions of peroxynitrite produced a decrease in the difference spectrum centered at 385 nm and 460 nm consistent with a change in the absorbance characteristics of the chromophore (inset, absorbance of GFP denatured with urea).

Figure 4.5

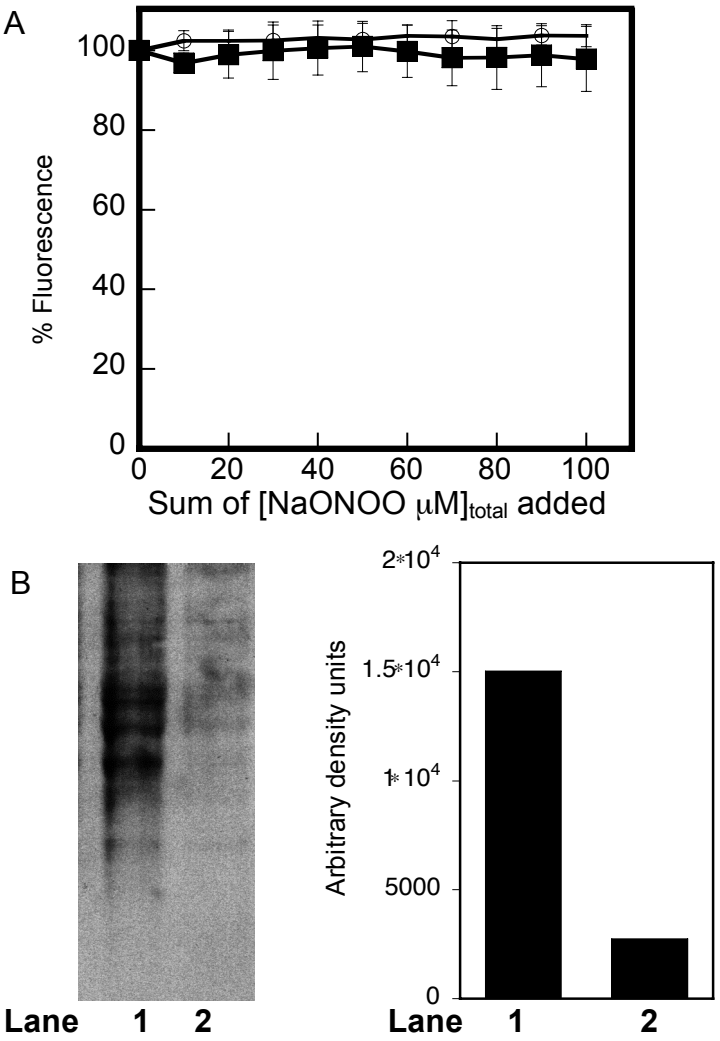

Figure 4.5. Nitration of glial cells expressing GFP-α-actinin with peroxynitrite. (A) Shown is the intracellular fluorescence of GFP from glial exposed to 10 μM sequential additions of peroxynitrite (filled squares, Avg. or 4 experiments +/- STD) or decomposed peroxynitrite(open circles, Avg. of 3 experiments +/- STD). (B) The western blot analysis for nitrotyrosine and the subsequent densitomety of the entire lane of the cellular lysates from the glial cells treated with 100 μM peroxynitrite (lane 1) or decomposed peroxynitrite (lane 2).

Chapter 5

Conclusion and Outlook

My research on oxidation of GFP and alkyl hydroperoxide reductase began as first year laboratory rotation projects, which drew my interest towards the subtle interactions of protein structure with oxidative stress. Although superoxide dismutase, the alkyl hydroperoxide reductase system and green fluorescent protein are completely different systems, understanding how the structure of each individually affects their interactions with oxidants has provided unanticipated insights into the subtle aspects of how multiple mutations to SOD may induce subtle alterations affecting a protein disulfide bond within SOD to cause ALS.

An appreciation for the subtleties of disulfide bond formation came from the structural studies of the thioredoxin-like N-terminal domain of AhpF (NTD-AhpF; chapter 3), which revealed in atomic detail, two intermediates in the catalytic cycle of the AhpR system of *Salmonella typhmirium*. The first was the oxidized structure of the active site and the second was a rarely observed reduced thiol-thiolate hydrogen bond intermediate.

Cys-S-S-Cys	*Oxidized*
Cys-SH$^{\cdots}$S-Cys	*Thiol-thioloate Intermediate also reduced*
Cys-SH HS-Cys	Reduced

The structure of the N-terminal domain of AhpF is unusual compared to other thioredoxin family members, because it is composed of two contiguous thioredoxin-like domains with only one functional active site. The structures of both the oxidized and reduced form of NTD-AhpF represent proposed intermediates in the catalytic cycle of many thioredoxin family members that have the conserved -C-X-X-C- motif. The measured pK_a of 5.1[190] for NTD-AhpF and the high reduction potential (ca. -264mV)[118] deviated from the norm

observed for other members of the thioredoxin family, such as thioredoxin (pK_a ~ 7; E_o' ~270mV). The uncoupling between the pK_a value and redox potential observed for NTD-AhpF provides an opportunity to study the factors that govern the redox potential of a disulfide bond.

Functionally, a lower pK_a would result in a greater fraction of reduced enzyme forming the thiol-thiolate intermediate at physiological pH. Hence, the decrease in pK_a observed for the NTD-AhpF may promote the reduction of oxidized AhpC. Minimizing the time that AhpC was in the oxidized state could be advantageous for *S. typhimurium* because the more rapidly that AhpC can be regenerated, the better the defense against hydrogen peroxide produced by the host's immune system. Conversely, peroxiredoxins in *H. sapiens* are less likely to be subject to a high concentration of hydrogen peroxide produced by phagocytic cells. Thus, the turnover of *H. sapiens* peroxiredoxins does not need to be as rapid, and therefore the higher pK_a of thioredoxin is less disadvantageous. The need for *S. typhimurium* to rapidly turnover oxidized AhpC may have driven the selection for a thioredoxin-like domain that retains the highly reducing nature of thioredoxin but has increased reactivity due to a lowered pK_a. This may explain why the ratio between pK_a and redox potential for NTD-AhpF is shifted compared to thioredoxin from many eukaryotes. Furthermore, this hypothesis would predict that other prokaryotes that rely on the alkylhydroperoxidase system for defense against the immune systems of a host will also have a pK_a/redox potential similar to NTD-AhpF.

Two neighboring cysteines have been engineered to create a redox-sensitive GFP. When oxidized, these cysteines form a disulfide bond near the beta bulge centered at His148.[191; 192] This redox-sensitve GFP system provided a platform to study how neighboring amino acids can modulate the redox potential of a disulfide bond. Using mutational analysis, Cannon and Remington showed that introducing positively charge residues near the disulfide of redox-sensitive GFP resulted in a more oxidizing redox potential.[191] This is in agreement with the ability of positively charged residues to reduce

the pK_a of the active site of many thioredoxin-like proteins.[135; 138; 139; 144] Decreasing the pK_a generally results in a more oxidizing redox potential. The similarities in the factors that regulate the disulfide in redox-sensitive GFP and thioredoxin family members allude to the possibility that the factors that govern the properties of disulfides may be conserved. Thus, insights into the factors that govern the active site disulfide from thioredoxin motifs and redox active GFP may be applicable to disulfides in other proteins such as SOD.

The study of redox-sensitive GFP and the mutational analysis of residues around the β-bulge centered at residue H148 have demonstrated that the fluorescence of GFP is particularly sensitive to changes in the amino acids in that region.[181; 182] We have demonstrated that the decrease in GFP fluorescence induced by peroxynitrite was not due to nitration of Tyr66 that forms the chromophore (chapter 4) and that nitration or oxidation of other residues than the chromophore is most likely responsible for the loss in fluorescence. This is structurally reasonable considering that the beta barrel of GFP fully surrounds the chromophore and thus protects the chromophore from oxidation by limiting its solvent accessibility. Oxidative modification of His148 or the neighboring Tyr145 could plausibly affect the fluorescence of GFP, as they are both part of the β-bulge. In addition, His148 and Tyr145 are both solvent accessible, unlike Tyr66 of the chromophore, making them more likely targets for oxidation and nitration. We were unable to identify Try 145 by mass spectrometry and can therefore not conclude if nitration of Tyr 145 affects GFP fluorescence. Alternatively, Trp57, which is precariously positioned at the top of the helix that extends thru the β-barrel of GFP, may be a target of oxidation that results in the loss of GFP fluorescence.

Over 100 mutations to the superoxide-scavenging enzyme; superoxide dismutase have been linked to ALS since 1993. These mutations are inherited in a dominant fashion, but cause only 2-3% of ALS cases. Roughly 90% of ALS cases are sporadic with no familial history, while other mostly unknown genes underlie another 8% of familial ALS. People with mutations to SOD

develop ALS at the same age as sporadic patients, which is typically between 40-80 years of age. The mutant SOD is expressed in all cells from birth. A causal role for SOD mutations was quickly established when transgenic mice expressing G93A SOD were created by Gurney et al. in 1994. Since then, multiple lines of transgenic mice as well as two lines of mutant SOD-expressing rats have been created that all develop motor neuron disease. The mutations are widely distributed throughout the SOD protein and are generally recognized to destabilize the protein (Figure 5.1). Mutations associated with ALS occur in all of the functional domains of the protein including the active site, dimer interface and β-barrel. Many reduce the stability of SOD.[20; 21; 26; 70; 71]

The mutant proteins are also more prone to aggregation when expressed in vitro. Aggregates of SOD in motor neurons are observed in some animal models, but often late in the disease and do not necessarily correlate with the development of disease. In spite of 14 years of intense research, the mechanism of how SOD causes ALS remains highly debated with several paradoxical results. For example, expression of wild type SOD generally protects transgenic animals from many types of stress, but expression of both wild-type and mutant SOD in transgenic mice accelerates disease progression[96; 97]. Eliminating the endogenous mouse copper chaperone for SOD (CCS) has no significant effect on disease progression in mutant SOD. However, SOD can obtain copper by a mechanism independent of the copper chaperone protein.[193] Remarkably, overexpressing human CCS dramatically accelerates the death of low expressing G93A SOD mice from 220 days to 39 days[194], suggesting the insertion of copper into SOD greatly enhances toxicity. On the other hand, a mutant of SOD with all four ligands for copper eliminated can still cause motor neuron disease to develop, which appears to rule out a role of copper in ALS. However, copper has been recognized since the 1970's to migrate into the zinc site of SOD and thus might still be participating in the toxicity of this Quad-His mutant SOD.[39]

Understanding the potentially toxic properties of zinc-deficient SOD prompted us to characterize the effects of zinc deficiency on the structure of SOD. Through collaboration with the Tainer lab (Scripps Institute), we completed the structural analysis of a constitutively zinc-deficient mutant protein of superoxide dismutase (chapter 2). The loss of zinc resulted in a remarkable destabilization of the two loops forming the active site channel that normally limits access of small molecules to the bound copper. The opening of the active site channel provides a rational for the 3000 fold acceleration in the rate of ascorbate oxidation by zinc-deficient SOD.[38] Functionally, two important consequences of increased accessibility to the copper in zinc-deficient SOD are to deplete intracellular antioxidants such as ascorbate and increase in the production of superoxide and peroxynitrite.[38]

A surprising result from the crystal structure of zinc-deficient SOD was that the dimer interface was perturbed, allowing the SOD monomers to reorient with respect to each other more than has been described in any other crystal structure (chapter 2). The altered dimer interface suggests that there should be a general decrease in the stability of the dimer. The shift in the orientation of SOD monomers was also coupled with an increased flexibility of the single disulfide (C57-C146) contained in SOD. The zinc-binding loop is connected by a short sequence to C57, which forms 70% of the dimer interface (Figure 5.2). Thus, the increased flexibility resulting from the loss of zinc would be expected to increase the flexibility of the normally rigid disulfide and make it more susceptible to reduction (Figure 5.3). The loss of zinc in combination with the reduction of the C57-C146 disulfide promotes the formation of aggregation-prone monomers[35; 95] Consistent with the interrelation between zinc-deficiency and reduction of the C57-C146 disulfide, we found that zinc-deficient SOD is more susceptible to aggregation in the presence of thiol-reductants (chapter 2).

The ability of Cu,Zn SOD to prevent the thiol-dependent aggregation of zinc-deficient SOD is consistent with the more native-like conformation of the

Cu,Zn subunit stabilizing the disulfide loop of the zinc-deficient SOD subunit. An increase in the stability of the disulfide would make zinc-deficient SOD less susceptible to disulfide reduction and thereby decrease the rate of formation of aggregation-prone monomers. Recently, the formation of a heterodimer of apoSOD with zinc-replete SOD has been shown to diminish the binding of zinc to the zinc-deficient apo subunit.[197] The diminished ability of zinc-deficient SOD to bind zinc and the protection of the disulfide from reduction due to heterodimer formation, would increase the half-life of zinc-deficient SOD. This stabilization of zinc-deficient SOD by wild-type Cu,Zn SOD might help explain the dominant inheritance of SOD.

Thus, the structure of zinc-deficient SOD has provided insights into how SOD can become toxic to motor neurons through simply the loss of the zinc atom. These considerations apply equally to sporadic ALS because wild-type SOD that becomes zinc-deficient is equally toxic as zinc-deficient SOD. In this hypothesis, the ALS-associated mutations to SOD would simply increase the chances that mutant SOD will become zinc-deficient. However, important questions remains as to why the ALS-SOD mutations could lead to the formation of zinc-deficient SOD in motor neurons.

Because mutations of SOD increase the susceptibility of the C57-C146 disulfide to reduction under physiological conditions,[198] we propose that the reduction of the disulfide makes the mutant SODs more susceptible to the loss of zinc. Just as the loss of zinc makes SOD more susceptible to reduction of the disulfide, reduction of the disulfide should strongly favor the loss of zinc. In contrast, copper is held by three histidine ligands on the stable beta-barrel and thus would be retained more strongly than zinc. Copper might also help in the reoxidation of C57 and C146 after zinc is lost to reform the stabilized disulfide bridge. Without zinc, both the loop containing C57 will be more mobile as well as Arg143 that sits between the disulfide bond and the active site copper that is normally located about 8 Å from C57 (Figure 5.3). Thus, the copper could readily oxidize C57 to a radical, which would react with C146. The resulting

disulfide radical is strongly reducing and will react with oxygen to produce superoxide to regenerate the C57-C146 disulfide bridge.

$$C57\text{-}SH + Cu^{2+} \rightarrow C57\text{-}S^{\cdot} + Cu^{1+} + H^{+}$$
$$C57\text{-}S^{\cdot} + C146\text{-}SH \rightarrow C57\ S^{\cdot -}\text{-}S\text{-}C146 + H^{+}$$
$$C57\ S^{\cdot -}\text{-}S\text{-}C146 + O2 \rightarrow C57\text{-}S\text{-}S\text{-}C146 + O_2^{\cdot -}$$

In this sequence, intracellular thiol reducing agents may promote the loss of zinc from SOD, while allowing the disulfide to reform. The process of copper catalyzed disulfide reduction would provide an additional means to stabilize zinc-deficient SOD by enabling it to form homodimers or heterodimers with Cu,Zn SOD. If the disulfide remained reduced, the SOD would stay as a monomer and be removed as a nontoxic aggregate.

The presence of a stable disulfide in SOD is unusual because SOD is found in the reducing environment of the cytosol and even 100 mM DTT concentrations do not appreciably reduce the disulfide in wild-type SOD.[95] However, mutations to SOD that perturb the SOD structure will create greater flexibility of the disulfide bond and make it more accessible to physiologically relevant concentrations of glutathione or thiol-reducing enzymes such as glutaredoxin or thioredoxin. Thus, the transient reduction of the disulfide bridge may make mutant SOD more susceptible to losing zinc in vivo.

This mechanism may help explain one of the most striking results obtained in SOD-expressing mice. The copper chaperone (CCS) protein is responsible for the direct insertion of copper into the active site of SOD. Little is known about how SOD obtains zinc, however it is known that the copper chaperone protein requires zinc to be bound to SOD in order to insert copper.[199] In a low expressing G93A SOD transgenic mouse model of ALS, coexpression of human CCS dramatically reduced the mean survival time from ~240 days in the G93A mice to 36 days in the doubly transgenic mice,[194] but has no ill effects in wild-type SOD transgenic mice. These results are

consistent with CCS inserting copper into both wild type SOD and mutant SOD, but that zinc is lost more readily from the mutant SOD and this results in the dramatically more rapid progression of disease in these mice.

Mitochondria may also have an important role in the formation of zinc deficient SOD as well as in the resulting toxicity. There is an increasing amount of interest in the role that mitochondria have in ALS. Several reports have shown that SOD associates with the mitochondria as the disease progresses and SOD can be toxic to the mitochondria .[24; 25; 97] The import of SOD into the mitochondria requires that the SOD have a reduced disulfide and not contain metals.[199] Interestingly, there is evidence that the final step of activation of Cu,Zn SOD in the inter membrane space of the mitochondria maybe regulated by a thiol-disulfide conversion mediated by protein disulfide isomerase (PDI).[200] Protein disulfide isomerase is a member of the thioredoxin family and has the classic -C-X-X-C- motif that is also found in the NTD-AhpF (chapter 3). PDI is known to have both protein chaperone and disulfide exchange properties that facilitate the folding and disulfide formation of nascent proteins.[201; 202] Recent studies have shown that PDI can be located in the inter mitochondrial space in addition to the endoplasmic reticulum. PDI has also be found to complex with both wild type and mutant SOD.[203] In addition to the PDI complexes, the insertion of copper by CCS into SOD involves a CCS:SOD complex that is held together by hydrophobic interactions and an intermolecular disulfide bond.[204] How the CCS:SOD intramolecular disulfide is resolved remains unclear, but PDI is a prime candidate because of its disulfide exchange properties. The activation of SOD in the inter mitochondrial space is dependent on the function of PDI.[200] The strong reducing environment of the mitochondria may increase the formation of zinc-deficient mutant SOD compared to wild-type SOD because of the more facile reduction of the disulfide bridge.

In conclusion, this thesis describes the first X-ray crystal structure of zinc-deficient form of Cu, Zn SOD. The aggregation and dimer exchange

properties of zinc-deficient SOD reported in this thesis extend our understanding of how zinc-deficient SOD is toxic and how mutations to SOD may result in ALS. In addition, the biochemical characterization of the NTD-AhpF revealed a relationship between the pK_a and redox potential of the active site disulfide that has not been observed in other members of the thioredoxin family. Lastly, we demonstrate that GFP is not a sufficiently sensitive reporter for detecting in vivo nitration.

Figure 5.1

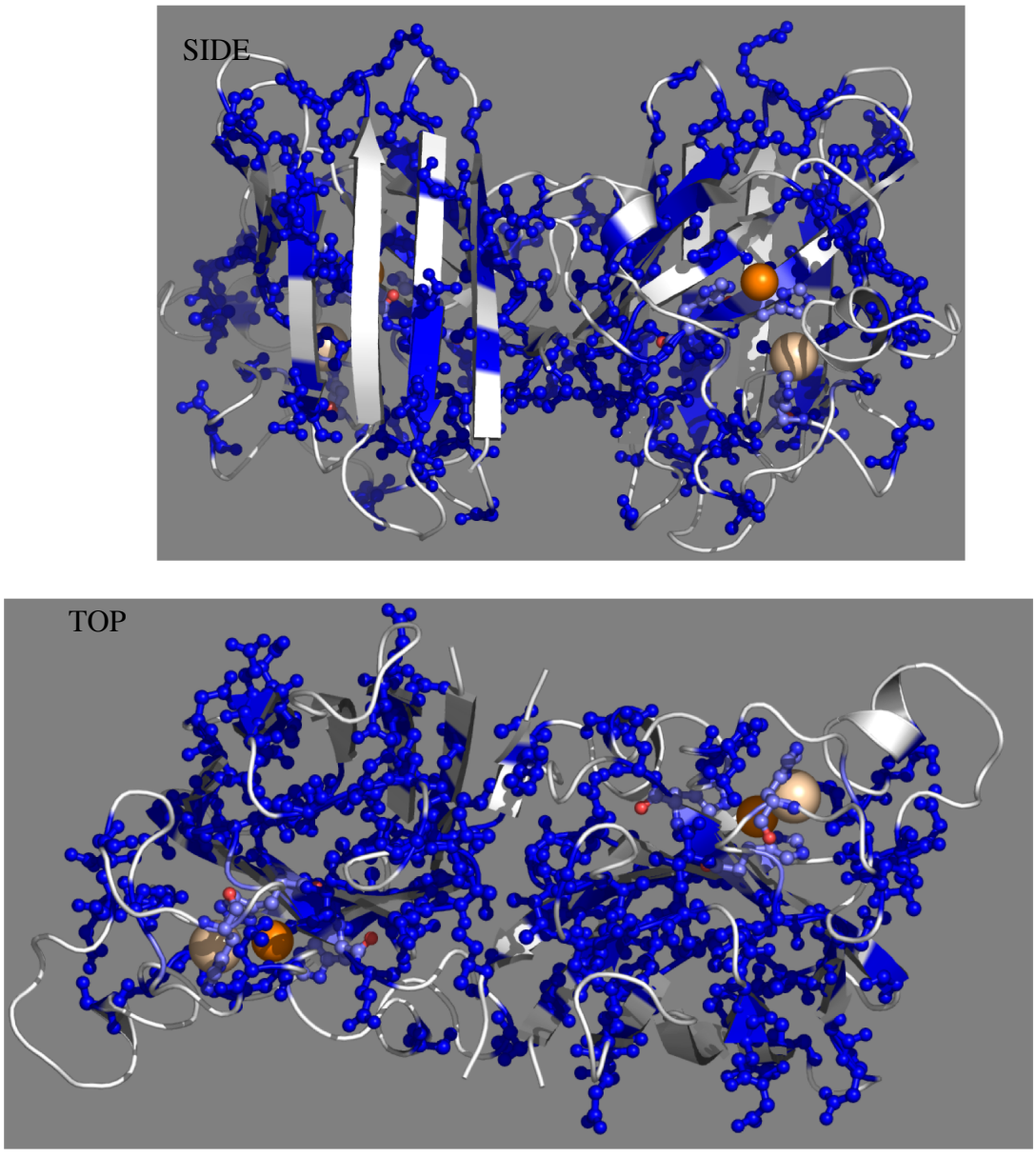

Figure 5.1. Location of ALS causing mutations on SOD. Shown is a ribbon diagram of Cu,Zn SOD. Residues that have been associated with the familial form of Amyotrophic lateral sclerosis (Blue) are found throughout the SOD polypeptide. Copper (copper) and zinc (grey) are represented as spheres. This image was generated using Pymol.[107]

Figure 5.2

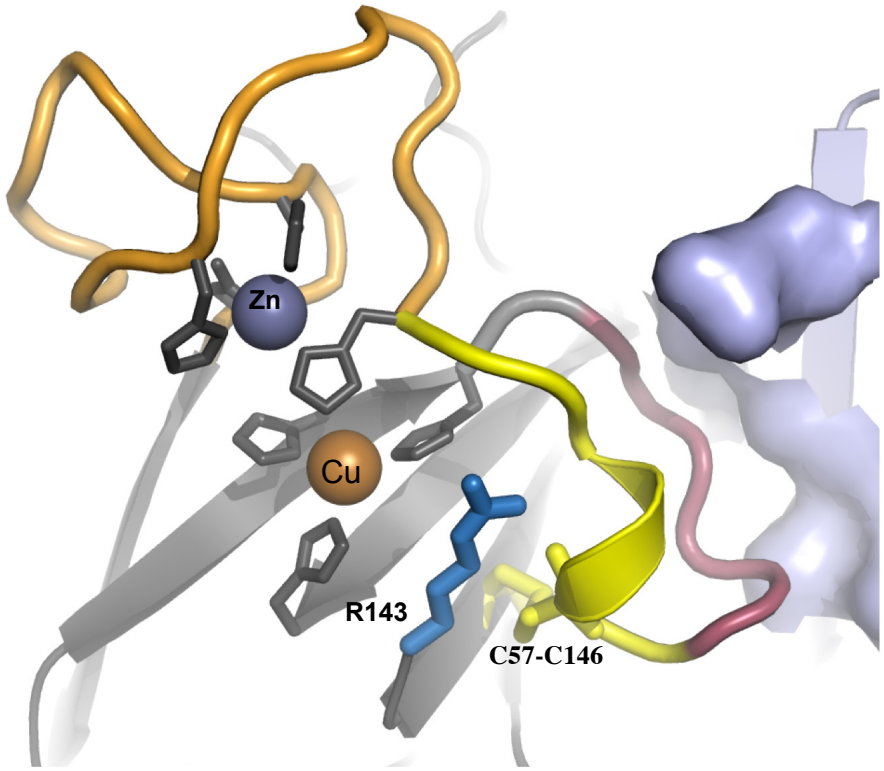

Figure 5.2 The link between the disulfide and the zinc binding site and dimer interface. The yellow ribbon diagram of Cu, Zn SOD illustrates the relationship between the C57-C146 disulfide (yellow sticks) and the zinc-binding site(orange ribbon). Arg 143 (blue sticks), copper, and zinc (orange and grey spheres respectively) are also depicted. The surface of the residues from the opposing subunit that are in contact with the dimer interface sub-loop (raspberry) are shown in light blue. This image was generated using Pymol and pdb code 1HL5.[107]

Figure 5.3

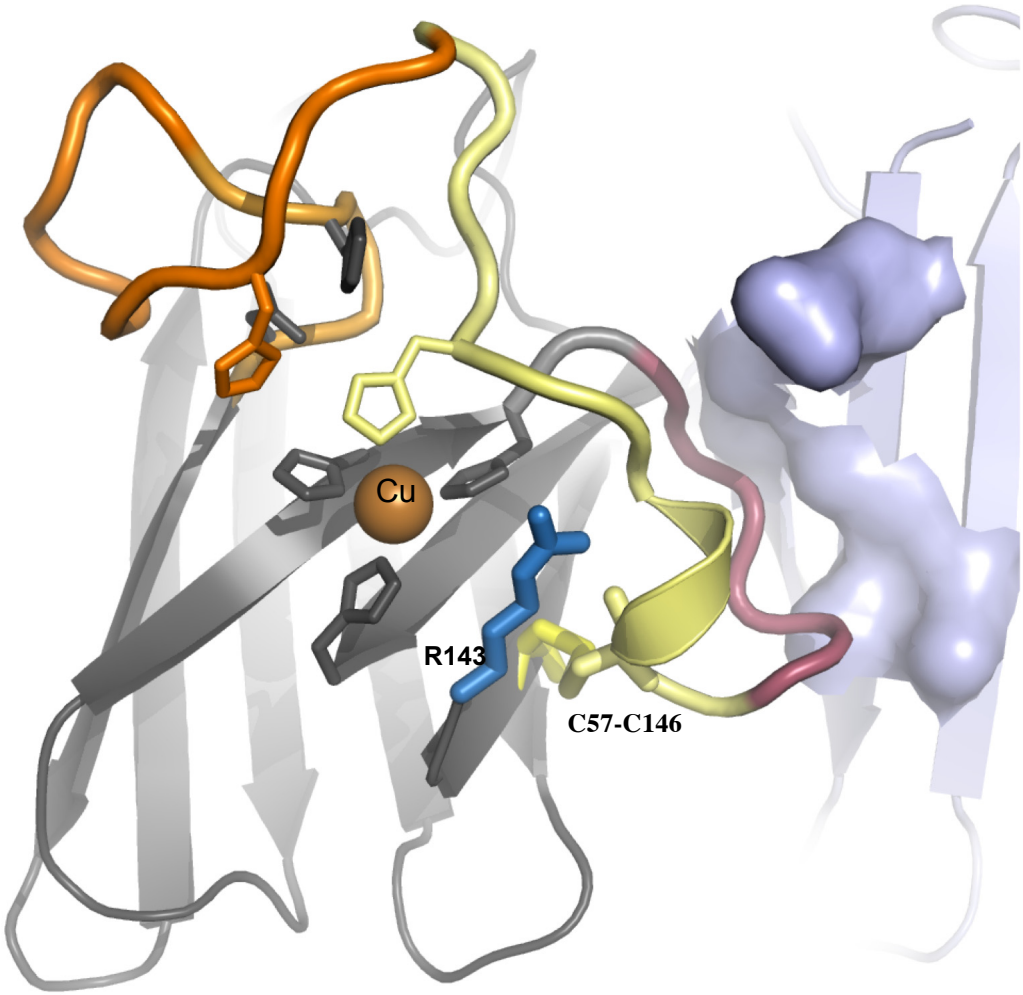

Figure 5.3. The affect the loss of zinc has on the stability of the zinc loop. The disulfide and part of the zinc-binding loop are shown as a pale yellow ribbon the residues highlighted in orange represent the part of the zinc-loop that becomes disordered in the absence of zinc. The interface between the opposing subunit (light blue surface) and the dimer interface sub-loop (raspberry ribbon) are also shown. This image was generated using Pymol and pdb code 1HL5.[107]

BIBLIOGRAPHY

1. Fridovich, I. (1997). Superoxide anion radical (O2-.), superoxide dismutases, and related matters. *J Biol Chem* **272**, 18515-7.
2. Okado-Matsumoto, A. & Fridovich, I. (2001). Subcellular distribution of superoxide dismutases (SOD) in rat liver: Cu,Zn-SOD in mitochondria. *J Biol Chem* **276**, 38388-93.
3. Sturtz, L. A., Diekert, K., Jensen, L. T., Lill, R. & Culotta, V. C. (2001). A fraction of yeast Cu,Zn-superoxide dismutase and its metallochaperone, CCS, localize to the intermembrane space of mitochondria. A physiological role for SOD1 in guarding against mitochondrial oxidative damage. *J Biol Chem* **276**, 38084-9.
4. Klug, D., Rabani, J. & Fridovich, I. (1972). A direct demonstration of the catalytic action of superoxide dismutase through the use of pulse radiolysis. *J Biol Chem* **247**, 4839-42.
5. McCord, J. M. & Fridovich, I. (1988). Superoxide dismutase: the first twenty years (1968-1988). *Free Radic Biol Med* **5**, 363-9.
6. Lisa M. Ellerby, D. E. C., Janet A. Graden, and & Valentine, J. S. (1996). Copper-Zinc Superoxide Dismutase: Why Not pH-Dependent? *Journal of American Chemical Society* **118**, 6556-6561.
7. Hart, P. J., Balbirnie, M. M., Ogihara, N. L., Nersissian, A. M., Weiss, M. S., Valentine, J. S. & Eisenberg, D. (1999). A structure-based mechanism for copper-zinc superoxide dismutase. *Biochemistry* **38**, 2167-78.
8. Tainer, J. A., Getzoff, E. D., Richardson, J. S. & Richardson, D. C. (1983). Structure and mechanism of copper, zinc superoxide dismutase. *Nature* **306**, 284-7.
9. Forman, H. J. & Fridovich, I. (1973). On the stability of bovine superoxide dismutase. The effects of metals. *J Biol Chem* **248**, 2645-9.
10. Pantoliano, M. W., Valentine, J. S., Burger, A. R. & Lippard, S. J. (1982). A pH-dependent superoxide dismutase activity for zinc-free bovine erythrocuprein. Reexamination of the role of zinc in the holoprotein. *J Inorg Biochem* **17**, 325-41.
11. Fee, J. A. & Bull, C. (1986). Steady-state kinetic studies of superoxide dismutases. Saturative behavior of the copper- and zinc-containing protein. *J Biol Chem* **261**, 13000-5.
12. Banci, L., Bertini, I., Cabelli, D. E., Hallewell, R. A., Tung, J. W. & Viezzoli, M. S. (1991). A characterization of copper/zinc superoxide dismutase mutants at position 124. Zinc-deficient proteins. *Eur J Biochem* **196**, 123-8.
13. O'Neill, P., Davies, S., Fielden, E. M., Calabrese, L., Capo, C., Marmocchi, F., Natoli, G. & Rotilio, G. (1988). The effects of pH and various salts upon the activity of a series of superoxide dismutases. *Biochem J* **251**, 41-6.
14. Rowland, L. P. & Shneider, N. A. (2001). Amyotrophic lateral sclerosis. *N Engl J Med* **344**, 1688-700.

15. Deng, H. X., Hentati, A., Tainer, J. A., Iqbal, Z., Cayabyab, A., Hung, W. Y., Getzoff, E. D., Hu, P., Herzfeldt, B., Roos, R. P. & et al. (1993). Amyotrophic lateral sclerosis and structural defects in Cu,Zn superoxide dismutase. *Science* **261**, 1047-51.
16. Rosen, D. R., Siddique, T., Patterson, D., Figlewicz, D. A., Sapp, P., Hentati, A., Donaldson, D., Goto, J., O'Regan, J. P., Deng, H. X. & et al. (1993). Mutations in Cu/Zn superoxide dismutase gene are associated with familial amyotrophic lateral sclerosis. *Nature* **362**, 59-62.
17. Parton, M. J., Broom, W., Andersen, P. M., Al-Chalabi, A., Nigel Leigh, P., Powell, J. F. & Shaw, C. E. (2002). D90A-SOD1 mediated amyotrophic lateral sclerosis: a single founder for all cases with evidence for a Cis-acting disease modifier in the recessive haplotype. *Hum Mutat* **20**, 473.
18. Jonsson, P. A., Backstrand, A., Andersen, P. M., Jacobsson, J., Parton, M., Shaw, C., Swingler, R., Shaw, P. J., Robberecht, W., Ludolph, A. C., Siddique, T., Skvortsova, V. I. & Marklund, S. L. (2002). CuZn-superoxide dismutase in D90A heterozygotes from recessive and dominant ALS pedigrees. *Neurobiol Dis* **10**, 327-33.
19. Gurney, M. E., Pu, H., Chiu, A. Y., Dal Canto, M. C., Polchow, C. Y., Alexander, D. D., Caliendo, J., Hentati, A., Kwon, Y. W., Deng, H. X. & et al. (1994). Motor neuron degeneration in mice that express a human Cu,Zn superoxide dismutase mutation. *Science* **264**, 1772-5.
20. Bruijn, L. I., Miller, T. M. & Cleveland, D. W. (2004). Unraveling the mechanisms involved in motor neuron degeneration in ALS. *Annu Rev Neurosci* **27**, 723-49.
21. Jonsson, P. A., Ernhill, K., Andersen, P. M., Bergemalm, D., Brannstrom, T., Gredal, O., Nilsson, P. & Marklund, S. L. (2004). Minute quantities of misfolded mutant superoxide dismutase-1 cause amyotrophic lateral sclerosis. *Brain* **127**, 73-88.
22. Valentine, J. S., Doucette, P. A. & Potter, S. Z. (2005). COPPER-ZINC SUPEROXIDE DISMUTASE AND AMYOTROPHIC LATERAL SCLEROSIS. *Annu. Rev. Biochem* **74**, 563-93.
23. Watanabe, M., Dykes-Hoberg, M., Culotta, V. C., Price, D. L., Wong, P. C. & Rothstein, J. D. (2001). Histological evidence of protein aggregation in mutant SOD1 transgenic mice and in amyotrophic lateral sclerosis neural tissues. *Neurobiol Dis* **8**, 933-41.
24. Bacman, S. R., Bradley, W. G. & Moraes, C. T. (2006). Mitochondrial involvement in amyotrophic lateral sclerosis: trigger or target? *Mol Neurobiol* **33**, 113-31.
25. Hervias, I., Beal, M. F. & Manfredi, G. (2006). Mitochondrial dysfunction and amyotrophic lateral sclerosis. *Muscle Nerve* **33**, 598-608.
26. Okado-Matsumoto, A. & Fridovich, I. (2002). Amyotrophic lateral sclerosis: a proposed mechanism. *Proc Natl Acad Sci U S A* **99**, 9010-4.
27. Wang, J., Slunt, H., Gonzales, V., Fromholt, D., Coonfield, M., Copeland, N. G., Jenkins, N. A. & Borchelt, D. R. (2003). Copper-binding-site-null SOD1

causes ALS in transgenic mice: aggregates of non-native SOD1 delineate a common feature. *Hum Mol Genet* **12**, 2753-64.

28. Morrison, B. M., Morrison, J. H. & Gordon, J. W. (1998). Superoxide dismutase and neurofilament transgenic models of amyotrophic lateral sclerosis. *J Exp Zool* **282**, 32-47.
29. Sherman, M. Y. & Goldberg, A. L. (2001). Cellular defenses against unfolded proteins: a cell biologist thinks about neurodegenerative diseases. *Neuron* **29**, 15-32.
30. Johnston, J. A. & Madura, K. (2004). Rings, chains and ladders: ubiquitin goes to work in the neuron. *Prog Neurobiol* **73**, 227-57.
31. Lynch, S. M., Boswell, S. A. & Colon, W. (2004). Kinetic stability of Cu/Zn superoxide dismutase is dependent on its metal ligands: implications for ALS. *Biochemistry* **43**, 16525-31.
32. Lindberg, M. J., Bystrom, R., Boknas, N., Andersen, P. M. & Oliveberg, M. (2005). Systematically perturbed folding patterns of amyotrophic lateral sclerosis (ALS)-associated SOD1 mutants. *Proc Natl Acad Sci U S A* **102**, 9754-9.
33. Hornberg, A., Logan, D. T., Marklund, S. L. & Oliveberg, M. (2007). The Coupling between Disulphide Status, Metallation and Dimer Interface Strength in Cu/Zn Superoxide Dismutase. *J Mol Biol* **365**, 333-42.
34. Khare, S. D., Caplow, M. & Dokholyan, N. V. (2004). The rate and equilibrium constants for a multistep reaction sequence for the aggregation of superoxide dismutase in amyotrophic lateral sclerosis. *Proc Natl Acad Sci U S A* **101**, 15094-9.
35. Doucette, P. A., Whitson, L. J., Cao, X., Schirf, V., Demeler, B., Valentine, J. S., Hansen, J. C. & Hart, P. J. (2004). Dissociation of human copper-zinc superoxide dismutase dimers using chaotrope and reductant. Insights into the molecular basis for dimer stability. *J Biol Chem* **279**, 54558-66.
36. Beckman, J. S., Carson, M., Smith, C. D. & Koppenol, W. H. (1993). ALS, SOD and peroxynitrite. *Nature* **364**, 584.
37. Beckman, J. S., Estevez, A. G., Crow, J. P. & Barbeito, L. (2001). Superoxide dismutase and the death of motoneurons in ALS. *Trends Neurosci* **24**, S15-20.
38. Estevez, A. G., Crow, J. P., Sampson, J. B., Reiter, C., Zhuang, Y., Richardson, G. J., Tarpey, M. M., Barbeito, L. & Beckman, J. S. (1999). Induction of nitric oxide-dependent apoptosis in motor neurons by zinc-deficient superoxide dismutase. *Science* **286**, 2498-500.
39. Valentine, J. S., Pantoliano, M. W., McDonnell, P. J., Burger, A. R. & Lippard, S. J. (1979). pH-dependent migration of copper(II) to the vacant zinc-binding site of zinc-free bovine erythrocyte superoxide dismutase. *Proc Natl Acad Sci U S A* **76**, 4245-9.
40. Lyons, T. J., Liu, H., Goto, J. J., Nersissian, A., Roe, J. A., Graden, J. A., Cafe, C., Ellerby, L. M., Bredesen, D. E., Gralla, E. B. & Valentine, J. S. (1996). Mutations in copper-zinc superoxide dismutase that cause amyotrophic lateral sclerosis alter the zinc binding site and the redox behavior of the protein. *Proc Natl Acad Sci U S A* **93**, 12240-4.

41. Crow, J. P., Sampson, J. B., Zhuang, Y., Thompson, J. A. & Beckman, J. S. (1997). Decreased zinc affinity of amyotrophic lateral sclerosis-associated superoxide dismutase mutants leads to enhanced catalysis of tyrosine nitration by peroxynitrite. *J Neurochem* **69**, 1936-44.
42. Hagen, T. M., Moreau, R., Suh, J. H. & Visioli, F. (2002). Mitochondrial decay in the aging rat heart: evidence for improvement by dietary supplementation with acetyl-L-carnitine and/or lipoic acid. *Ann N Y Acad Sci* **959**, 491-507.
43. Ames, B. N., Shigenaga, M. K. & Hagen, T. M. (1995). Mitochondrial decay in aging. *Biochim Biophys Acta* **1271**, 165-70.
44. Heinzelmann, M., Mercer-Jones, M. A. & Passmore, J. C. (1999). Neutrophils and renal failure. *Am J Kidney Dis* **34**, 384-99.
45. Babior, B. M. (2000). Phagocytes and oxidative stress. *Am J Med* **109**, 33-44.
46. Chen, L., Xie, Q. W. & Nathan, C. (1998). Alkyl hydroperoxide reductase subunit C (AhpC) protects bacterial and human cells against reactive nitrogen intermediates. *Mol Cell* **1**, 795-805.
47. Jacobson, F. S., Morgan, R. W., Christman, M. F. & Ames, B. N. (1989). An alkyl hydroperoxide reductase from Salmonella typhimurium involved in the defense of DNA against oxidative damage. Purification and properties. *J Biol Chem* **264**, 1488-96.
48. Niimura, Y., Poole, L. B. & Massey, V. (1995). Amphibacillus xylanus NADH oxidase and Salmonella typhimurium alkyl-hydroperoxide reductase flavoprotein components show extremely high scavenging activity for both alkyl hydroperoxide and hydrogen peroxide in the presence of S. typhimurium alkyl-hydroperoxide reductase 22-kDa protein component. *J Biol Chem* **270**, 25645-50.
49. Poole, L. B. & Ellis, H. R. (1996). Flavin-dependent alkyl hydroperoxide reductase from Salmonella typhimurium. 1. Purification and enzymatic activities of overexpressed AhpF and AhpC proteins. *Biochemistry* **35**, 56-64.
50. Christman, M. F., Morgan, R. W., Jacobson, F. S. & Ames, B. N. (1985). Positive control of a regulon for defenses against oxidative stress and some heat-shock proteins in Salmonella typhimurium. *Cell* **41**, 753-62.
51. Morgan, R. W., Christman, M. F., Jacobson, F. S., Storz, G. & Ames, B. N. (1986). Hydrogen peroxide-inducible proteins in Salmonella typhimurium overlap with heat shock and other stress proteins. *Proc Natl Acad Sci U S A* **83**, 8059-63.
52. Poole, L. B. (1996). Flavin-dependent alkyl hydroperoxide reductase from Salmonella typhimurium. 2. Cystine disulfides involved in catalysis of peroxide reduction. *Biochemistry* **35**, 65-75.
53. Ellis, H. R. & Poole, L. B. (1997). Novel application of 7-chloro-4-nitrobenzo-2-oxa-1,3-diazole to identify cysteine sulfenic acid in the AhpC component of alkyl hydroperoxide reductase. *Biochemistry* **36**, 15013-8.
54. Ellis, H. R. & Poole, L. B. (1997). Roles for the two cysteine residues of AhpC in catalysis of peroxide reduction by alkyl hydroperoxide reductase from Salmonella typhimurium. *Biochemistry* **36**, 13349-56.

55. Poole, L. B. & Ellis, H. R. (2002). Identification of cysteine sulfenic acid in AhpC of alkyl hydroperoxide reductase. *Methods Enzymol* **348**, 122-36.
56. Wood, Z. A., Poole, L. B., Hantgan, R. R. & Karplus, P. A. (2002). Dimers to doughnuts: redox-sensitive oligomerization of 2-cysteine peroxiredoxins. *Biochemistry* **41**, 5493-504.
57. Li Calzi, M. & Poole, L. B. (1997). Requirement for the two AhpF cystine disulfide centers in catalysis of peroxide reduction by alkyl hydroperoxide reductase. *Biochemistry* **36**, 13357-64.
58. Cha, M. K., Yun, C. H. & Kim, I. H. (2000). Interaction of human thiol-specific antioxidant protein 1 with erythrocyte plasma membrane. *Biochemistry* **39**, 6944-50.
59. Rabilloud, T., Heller, M., Rigobello, M. P., Bindoli, A., Aebersold, R. & Lunardi, J. (2001). The mitochondrial antioxidant defence system and its response to oxidative stress. *Proteomics* **1**, 1105-10.
60. Wagner, E., Luche, S., Penna, L., Chevallet, M., Van Dorsselaer, A., Leize-Wagner, E. & Rabilloud, T. (2002). A method for detection of overoxidation of cysteines: peroxiredoxins are oxidized in vivo at the active-site cysteine during oxidative stress. *Biochem J* **366**, 777-85.
61. Koo, K. H., Lee, S., Jeong, S. Y., Kim, E. T., Kim, H. J., Kim, K., Song, K. & Chae, H. Z. (2002). Regulation of thioredoxin peroxidase activity by C-terminal truncation. *Arch Biochem Biophys* **397**, 312-8.
62. Park, S. G., Cha, M. K., Jeong, W. & Kim, I. H. (2000). Distinct physiological functions of thiol peroxidase isoenzymes in Saccharomyces cerevisiae. *J Biol Chem* **275**, 5723-32.
63. Wood, Z. A., Poole, L. B. & Karplus, P. A. (2003). Peroxiredoxin evolution and the regulation of hydrogen peroxide signaling. *Science* **300**, 650-3.
64. Robinson, K. M., Janes, M. S., Pehar, M., Monette, J. S., Ross, M. F., Hagen, T. M., Murphy, M. P. & Beckman, J. S. (2006). Selective fluorescent imaging of superoxide in vivo using ethidium-based probes. *Proc Natl Acad Sci U S A* **103**, 15038-43.
65. Ueno, T., Urano, Y., Kojima, H. & Nagano, T. (2006). Mechanism-based molecular design of highly selective fluorescence probes for nitrative stress. *J Am Chem Soc* **128**, 10640-1.
66. Espey, M. G., Xavier, S., Thomas, D. D., Miranda, K. M. & Wink, D. A. (2002). Direct real-time evaluation of nitration with green fluorescent protein in solution and within human cells reveals the impact of nitrogen dioxide vs. peroxynitrite mechanisms. *Proc Natl Acad Sci U S A* **99**, 3481-6.
67. Shimomura, O. (1979). Structure of the chromophore of Aequorea green fluorescrent protein. *FEBS Lett.* **104**, 220-222.
68. Cody, C. W., Prasher, D. C., Westler, W. M., Prendergast, F. G. & Ward, W. W. (1993). Chemical structure of the hexapeptide chromophore of the Aequorea green-fluorescent protein. *Biochemistry* **32**, 1212-8.
69. Ward, W. W. & Bokman, S. H. (1982). Reversible denaturation of Aequorea green-fluorescent protein: physical separation and characterization of the renatured protein. *Biochemistry* **21**, 4535-40.

70. Hough, M. A., Grossmann, J. G., Antonyuk, S. V., Strange, R. W., Doucette, P. A., Rodriguez, J. A., Whitson, L. J., Hart, P. J., Hayward, L. J., Valentine, J. S. & Hasnain, S. S. (2004). Dimer destabilization in superoxide dismutase may result in disease-causing properties: structures of motor neuron disease mutants. *Proc Natl Acad Sci U S A* **101**, 5976-81.
71. DiDonato, M., Craig, L., Huff, M. E., Thayer, M. M., Cardoso, R. M., Kassmann, C. J., Lo, T. P., Bruns, C. K., Powers, E. T., Kelly, J. W., Getzoff, E. D. & Tainer, J. A. (2003). ALS mutants of human superoxide dismutase form fibrous aggregates via framework destabilization. *J Mol Biol* **332**, 601-15.
72. Cardoso, R. M., Thayer, M. M., DiDonato, M., Lo, T. P., Bruns, C. K., Getzoff, E. D. & Tainer, J. A. (2002). Insights into Lou Gehrig's disease from the structure and instability of the A4V mutant of human Cu,Zn superoxide dismutase. *J Mol Biol* **324**, 247-56.
73. Hart, P. J., Liu, H., Pellegrini, M., Nersissian, A. M., Gralla, E. B., Valentine, J. S. & Eisenberg, D. (1998). Subunit asymmetry in the three-dimensional structure of a human CuZnSOD mutant found in familial amyotrophic lateral sclerosis. *Protein Sci* **7**, 545-55.
74. Elam, J. S., Taylor, A. B., Strange, R., Antonyuk, S., Doucette, P. A., Rodriguez, J. A., Hasnain, S. S., Hayward, L. J., Valentine, J. S., Yeates, T. O. & Hart, P. J. (2003). Amyloid-like filaments and water-filled nanotubes formed by SOD1 mutant proteins linked to familial ALS. *Nat Struct Biol* **10**, 461-7.
75. Elam, J. S., Malek, K., Rodriguez, J. A., Doucette, P. A., Taylor, A. B., Hayward, L. J., Cabelli, D. E., Valentine, J. S. & Hart, P. J. (2003). An alternative mechanism of bicarbonate-mediated peroxidation by copper-zinc superoxide dismutase: rates enhanced via proposed enzyme-associated peroxycarbonate intermediate. *J Biol Chem* **278**, 21032-9.
76. Lindberg, M. J., Normark, J., Holmgren, A. & Oliveberg, M. (2004). Folding of human superoxide dismutase: disulfide reduction prevents dimerization and produces marginally stable monomers. *Proc Natl Acad Sci U S A* **101**, 15893-8.
77. Banci, L., Bertini, I., Cantini, F., D'Amelio, N. & Gaggelli, E. (2006). Human SOD1 before harboring the catalytic metal: solution structure of copper-depleted, disulfide-reduced form. *J Biol Chem* **281**, 2333-7.
78. Ray, S. S., Nowak, R. J., Strokovich, K., Brown, R. H., Jr., Walz, T. & Lansbury, P. T., Jr. (2004). An intersubunit disulfide bond prevents in vitro aggregation of a superoxide dismutase-1 mutant linked to familial amytrophic lateral sclerosis. *Biochemistry* **43**, 4899-905.
79. Ge, W. W., Wen, W., Strong, W., Leystra-Lantz, C. & Strong, M. J. (2005). Mutant copper-zinc superoxide dismutase binds to and destabilizes human low molecular weight neurofilament mRNA. *J Biol Chem* **280**, 118-24.
80. Rakhit, R., Crow, J. P., Lepock, J. R., Kondejewski, L. H., Cashman, N. R. & Chakrabartty, A. (2004). Monomeric Cu,Zn-superoxide dismutase is a common misfolding intermediate in the oxidation models of sporadic and familial amyotrophic lateral sclerosis. *J Biol Chem* **279**, 15499-504.

81. Tiwari, A., Xu, Z. & Hayward, L. J. (2005). Aberrantly increased hydrophobicity shared by mutants of Cu,Zn-superoxide dismutase in familial amyotrophic lateral sclerosis. *J Biol Chem* **280**, 29771-9.
82. Pasinelli, P., Belford, M. E., Lennon, N., Bacskai, B. J., Hyman, B. T., Trotti, D. & Brown, R. H., Jr. (2004). Amyotrophic lateral sclerosis-associated SOD1 mutant proteins bind and aggregate with Bcl-2 in spinal cord mitochondria. *Neuron* **43**, 19-30.
83. Rodriguez, J. A., Shaw, B. F., Durazo, A., Sohn, S. H., Doucette, P. A., Nersissian, A. M., Faull, K. F., Eggers, D. K., Tiwari, A., Hayward, L. J. & Valentine, J. S. (2005). Destabilization of apoprotein is insufficient to explain Cu,Zn-superoxide dismutase-linked ALS pathogenesis. *Proc Natl Acad Sci U S A* **102**, 10516-21.
84. Strange, R. W., Antonyuk, S., Hough, M. A., Doucette, P. A., Rodriguez, J. A., Hart, P. J., Hayward, L. J., Valentine, J. S. & Hasnain, S. S. (2003). The structure of holo and metal-deficient wild-type human Cu, Zn superoxide dismutase and its relevance to familial amyotrophic lateral sclerosis. *J Mol Biol* **328**, 877-91.
85. Strange, R. W., Antonyuk, S. V., Hough, M. A., Doucette, P. A., Valentine, J. S. & Hasnain, S. S. (2006). Variable metallation of human superoxide dismutase: atomic resolution crystal structures of Cu-Zn, Zn-Zn and as-isolated wild-type enzymes. *J Mol Biol* **356**, 1152-62.
86. Ferraroni, M., Rypniewski, W., Wilson, K. S., Viezzoli, M. S., Banci, L., Bertini, I. & Mangani, S. (1999). The crystal structure of the monomeric human SOD mutant F50E/G51E/E133Q at atomic resolution. The enzyme mechanism revisited. *J Mol Biol* **288**, 413-26.
87. Burmeister, W. P. (2000). Structural changes in a cryo-cooled protein crystal owing to radiation damage. *Acta Crystallogr D Biol Crystallogr* **56**, 328-41.
88. Weik, M., Ravelli, R. B., Kryger, G., McSweeney, S., Raves, M. L., Harel, M., Gros, P., Silman, I., Kroon, J. & Sussman, J. L. (2000). Specific chemical and structural damage to proteins produced by synchrotron radiation. *Proc Natl Acad Sci U S A* **97**, 623-8.
89. Richardson, J. S. (1981). The anatomy and taxonomy of protein structure. *Adv Protein Chem* **34**, 167-339.
90. Berman, H. M., Henrick, K. & Nakamura, H. (2003). Announcing the worldwide Protein Data Bank. . *Nature Structural Biology* **10**, 980.
91. Burk, R. F., Christensen, J. M., Maguire, M. J., Austin, L. M., Whetsell, W. O., Jr., May, J. M., Hill, K. E. & Ebner, F. F. (2006). A combined deficiency of vitamins E and C causes severe central nervous system damage in guinea pigs. *J Nutr* **136**, 1576-81.
92. Spagnolo, L., Toro, I., D'Orazio, M., O'Neill, P., Pedersen, J. Z., Carugo, O., Rotilio, G., Battistoni, A. & Djinovic-Carugo, K. (2004). Unique features of the sodC-encoded superoxide dismutase from Mycobacterium tuberculosis, a fully functional copper-containing enzyme lacking zinc in the active site. *J Biol Chem* **279**, 33447-55.

93. D'Orazio, M., Folcarelli, S., Mariani, F., Colizzi, V., Rotilio, G. & Battistoni, A. (2001). Lipid modification of the Cu,Zn superoxide dismutase from Mycobacterium tuberculosis. *Biochem J* **359**, 17-22.
94. Blencowe, D. K. & Morby, A. P. (2003). Zn(II) metabolism in prokaryotes. *FEMS Microbiol Rev* **27**, 291-311.
95. Arnesano, F., Banci, L., Bertini, I., Martinelli, M., Furukawa, Y. & O'Halloran, T. V. (2004). The unusually stable quaternary structure of human Cu,Zn-superoxide dismutase 1 is controlled by both metal occupancy and disulfide status. *J Biol Chem* **279**, 47998-8003.
96. Fukada, K., Nagano, S., Satoh, M., Tohyama, C., Nakanishi, T., Shimizu, A., Yanagihara, T. & Sakoda, S. (2001). Stabilization of mutant Cu/Zn superoxide dismutase (SOD1) protein by coexpressed wild SOD1 protein accelerates the disease progression in familial amyotrophic lateral sclerosis mice. *Eur J Neurosci* **14**, 2032-6.
97. Deng, H. X., Shi, Y., Furukawa, Y., Zhai, H., Fu, R., Liu, E., Gorrie, G. H., Khan, M. S., Hung, W. Y., Bigio, E. H., Lukas, T., Dal Canto, M. C., O'Halloran, T. V. & Siddique, T. (2006). Conversion to the amyotrophic lateral sclerosis phenotype is associated with intermolecular linked insoluble aggregates of SOD1 in mitochondria. *Proc Natl Acad Sci U S A* **103**, 7142-7.
98. Leinweber, B., Barofsky, E., Barofsky, D. F., Ermilov, V., Nylin, K. & Beckman, J. S. (2004). Aggregation of ALS mutant superoxide dismutase expressed in Escherichia coli. *Free Radic Biol Med* **36**, 911-8.
99. Parge, H. E., Hallewell, R. A. & Tainer, J. A. (1992). Atomic structures of wild-type and thermostable mutant recombinant human Cu,Zn superoxide dismutase. *Proc Natl Acad Sci U S A* **89**, 6109-13.
100. Gill, S. C. & von Hippel, P. H. (1989). Calculation of protein extinction coefficients from amino acid sequence data. *Anal Biochem* **182**, 319-26.
101. Otwinowski, Z. & Minor, W. (1997). Processing of X-ray diffraction data collected in oscillation mode. *Methosd of Enzymology* **276**, 307-326.
102. Brunger, A. T., Adams, P. D., Clore, G. M., DeLano, W. L., Gros, P., Grosse-Kunstleve, R. W., Jiang, J. S., Kuszewski, J., Nilges, M., Pannu, N. S., Read, R. J., Rice, L. M., Simonson, T. & Warren, G. L. (1998). Crystallography & NMR system: A new software suite for macromolecular structure determination. *Acta Crystallogr D Biol Crystallogr* **54**, 905-21.
103. Jones, T. A., Zou, J. Y., Cowan, S. W. & Kjeldgaard. (1991). Improved methods for building protein models in electron density maps and the location of errors in these models. *Acta Crystallogr A* **47 (Pt 2)**, 110-9.
104. Savvides, S. N., Scheiwein, M., Bohme, C. C., Arteel, G. E., Karplus, P. A., Becker, K. & Schirmer, R. H. (2002). Crystal structure of the antioxidant enzyme glutathione reductase inactivated by peroxynitrite. *J Biol Chem* **277**, 2779-84.
105. Lovell, S. C., Davis, I. W., Arendall, W. B., 3rd, de Bakker, P. I., Word, J. M., Prisant, M. G., Richardson, J. S. & Richardson, D. C. (2003). Structure validation by Calpha geometry: phi,psi and Cbeta deviation. *Proteins* **50**, 437-50.

106. McDonald, I. K. & Thornton, J. M. (1994). Satisfying hydrogen bonding potential in proteins. *J Mol Biol* **238**, 777-93.
107. DeLano, W. L. (2002). The PyMOL Molecular Graphics System.
108. Olsen, P. H., Esmon, N. L., Esmon, C. T. & Laue, T. M. (1992). Ca2+ dependence of the interactions between protein C, thrombin, and the elastase fragment of thrombomodulin. Analysis by ultracentrifugation. *Biochemistry* **31**, 746-54.
109. Perkins, S. J. (1986). Protein volumes and hydration effects. The calculations of partial specific volumes, neutron scattering matchpoints and 280-nm absorption coefficients for proteins and glycoproteins from amino acid sequences. *Eur J Biochem* **157**, 169-80.
110. Weischet, W. O., Tatchell, K., Van Holde, K. E. & Klump, H. (1978). Thermal denaturation of nucleosomal core particles. *Nucleic Acids Res* **5**, 139-60.
111. Demeler, B. & van Holde, K. E. (2004). Sedimentation velocity analysis of highly heterogeneous systems. *Anal Biochem* **335**, 279-88.
112. Cao, W. & Demeler, B. (2005). Modeling analytical ultracentrifugation experiments with an adaptive space-time finite element solution of the Lamm equation. *Biophys J* **89**, 1589-602.
113. Schuck, P. (2000). Size-distribution analysis of macromolecules by sedimentation velocity ultracentrifugation and lamm equation modeling. *Biophys J* **78**, 1606-19.
114. Ausio, J., Malencik, D. A. & Anderson, S. R. (1992). Analytical sedimentation studies of turkey gizzard myosin light chain kinase and telokin. *Biophys J* **61**, 1656-63.
115. Poole, L. B. (2005). Bacterial defenses against oxidants: mechanistic features of cysteine-based peroxidases and their flavoprotein reductases. *Arch Biochem Biophys* **433**, 240-54.
116. Poole, L. B., Reynolds, C. M., Wood, Z. A., Karplus, P. A., Ellis, H. R. & Li Calzi, M. (2000). AhpF and other NADH:peroxiredoxin oxidoreductases, homologues of low Mr thioredoxin reductase. *Eur J Biochem* **267**, 6126-33.
117. Poole, L. B., Godzik, A., Nayeem, A. & Schmitt, J. D. (2000). AhpF can be dissected into two functional units: tandem repeats of two thioredoxin-like folds in the N-terminus mediate electron transfer from the thioredoxin reductase-like C-terminus to AhpC. *Biochemistry* **39**, 6602-15.
118. Reynolds, C. M. & Poole, L. B. (2000). Attachment of the N-terminal domain of Salmonella typhimurium AhpF to Escherichia coli thioredoxin reductase confers AhpC reductase activity but does not affect thioredoxin reductase activity. *Biochemistry* **39**, 8859-69.
119. Wood, Z. A., Poole, L. B. & Karplus, P. A. (2001). Structure of intact AhpF reveals a mirrored thioredoxin-like active site and implies large domain rotations during catalysis. *Biochemistry* **40**, 3900-11.
120. Alphey, M. S., Gabrielsen, M., Micossi, E., Leonard, G. A., McSweeney, S. M., Ravelli, R. B., Tetaud, E., Fairlamb, A. H., Bond, C. S. & Hunter, W. N. (2003). Tryparedoxins from Crithidia fasciculata and Trypanosoma brucei: photoreduction of the redox disulfide using synchrotron radiation and evidence

for a conformational switch implicated in function. *J Biol Chem* **278**, 25919-25.

121. Read, R. J. (1986). Improved Fourier coefficients for maps using phases from partial structures with errors. *Acta Cryst* **A42**, 140-149.
122. Benesch, R. E., Lardy, H. A. & Benesch, R. (1955). The sulfhydryl groups of crystalline proteins. I. Some albumins, enzymes, and hemoglobins. *J Biol Chem* **216**, 663-76.
123. Polgar, L. (1974). Mercaptide-imidazolium ion-pair: the reactive nucleophile in papain catalysis. *FEBS Lett* **47**, 15-8.
124. Graminski, G. F., Kubo, Y. & Armstrong, R. N. (1989). Spectroscopic and kinetic evidence for the thiolate anion of glutathione at the active site of glutathione S-transferase. *Biochemistry* **28**, 3562-8.
125. Kortemme, T., Darby, N. J. & Creighton, T. E. (1996). Electrostatic interactions in the active site of the N-terminal thioredoxin-like domain of protein disulfide isomerase. *Biochemistry* **35**, 14503-11.
126. Nelson, J. W. & Creighton, T. E. (1994). Reactivity and ionization of the active site cysteine residues of DsbA, a protein required for disulfide bond formation in vivo. *Biochemistry* **33**, 5974-83.
127. Weichsel, A., Gasdaska, J. R., Powis, G. & Montfort, W. R. (1996). Crystal structures of reduced, oxidized, and mutated human thioredoxins: evidence for a regulatory homodimer. *Structure* **4**, 735-51.
128. Jönsson, T. & Poole, L. B. (2002). Intramolecular electron transfer pathway in mutants of AhpF, a flavoprotein disulfide reductase. In *Flavins and Flavoproteins 2002* (Chapman, S., Perham, R. & Scrutton, N., eds.), pp. 691-696. Agency for Scientific Publications, Berlin.
129. Poole, L. B. (1999). Flavins and Flavoproteins 1999. *Agency for Scienctific Publications*, 691-694.
130. Grauschopf, U., Winther, J. R., Korber, P., Zander, T. P., Dallinger, P. & Bardwell, J. C. A. (1995). Why is DsbA such an oxidizing disulfide catalyst? *Cell* **83**, 947-955.
131. Kallis, G. B. & Holmgren, A. (1980). Differential reactivity of the functional sulfhydryl groups of cysteine-32 and cysteine-35 present in the reduced form of thioredoxin from Escherichia coli. *J Biol Chem* **255**, 10261-5.
132. Jeng, M. F., Holmgren, A. & Dyson, H. J. (1995). Proton sharing between cysteine thiols in Escherichia coli thioredoxin: implications for the mechanism of protein disulfide reduction. *Biochemistry* **34**, 10101-5.
133. Dyson, H. J., Jeng, M. F., Tennant, L. L., Slaby, I., Lindell, M., Cui, D. S., Kuprin, S. & Holmgren, A. (1997). Effects of buried charged groups on cysteine thiol ionization and reactivity in Escherichia coli thioredoxin: structural and functional characterization of mutants of Asp 26 and Lys 57. *Biochemistry* **36**, 2622-36.
134. Reckenfelderbaumer, N. & Krauth-Siegel, R. L. (2002). Catalytic properties, thiol pK value, and redox potential of Trypanosoma brucei tryparedoxin. *J Biol Chem* **277**, 17548-55.

135. Mössner, E., Iwai, H. & Glockshuber, R. (2000). Influence of the pKa value of the buried, active-site cysteine on the redox properties of thioredoxin-like oxidoreductases. *FEBS Lett.* **477**, 21-26.
136. Guddat, L. W., Bardwell, J. C. & Martin, J. L. (1998). Crystal structures of reduced and oxidized DsbA: investigation of domain motion and thiolate stabilization. *Structure* **6**, 757-67.
137. Nordstrand, K., Aslund, F., Meunier, S., Holmgren, A., Otting, G. & Berndt, K. D. (1999). Direct NMR observation of the Cys-14 thiol proton of reduced Escherichia coli glutaredoxin-3 supports the presence of an active site thiol-thiolate hydrogen bond. *FEBS Lett* **449**, 196-200.
138. Mössner, E., Huber-Wunderlich, M. & Glockshuber, R. (1998). Characterization of *Escherichia coli* thioredoxin variants mimicking the active-sites of other thiol-disulfide oxidoreductases. *Prot. Sci.* **7**, 1233-1244.
139. Foloppe, N. & Nilsson, L. (2004). The glutaredoxin -C-P-Y-C- motif: influence of peripheral residues. *Structure (Camb)* **12**, 289-300.
140. Krause, G., Lundstrom, J., Barea, J. L., Pueyo de la Cuesta, C. & Holmgren, A. (1991). Mimicking the active site of protein disulfide-isomerase by substitution of proline 34 in Escherichia coli thioredoxin. *J Biol Chem* **266**, 9494-500.
141. Chivers, P. T., Prehoda, K. E. & Raines, R. T. (1997). The CXXC motif: a rheostat in the active site. *Biochemistry* **36**, 4061-6.
142. Guddat, L. W., Bardwell, J. C., Glockshuber, R., Huber-Wunderlich, M., Zander, T. & Martin, J. L. (1997). Structural analysis of three His32 mutants of DsbA: support for an electrostatic role of His32 in DsbA stability. *Protein Sci* **6**, 1893-900.
143. Huber-Wunderlich, M. & Glockshuber, R. (1998). A single dipeptide sequence modulates the redox properties of a whole enzyme family. *Fold Des* **3**, 161-71.
144. Foloppe, N., Sagemark, J., Nordstrand, K., Berndt, K. D. & Nilsson, L. (2001). Structure, dynamics and electrostatics of the active site of glutaredoxin 3 from Escherichia coli: comparison with functionally related proteins. *J Mol Biol* **310**, 449-70.
145. Gane, P. J., Freedman, R. B. & Warwicker, J. (1995). A molecular model for the redox potential difference between thioredoxin and DsbA, based on electrostatics calculations. *J Mol Biol* **249**, 376-87.
146. Ruddock, L. W., Hirst, T. R. & Freedman, R. B. (1996). pH-dependence of the dithiol-oxidizing activity of DsbA (a periplasmic protein thiol:disulphide oxidoreductase) and protein disulphide-isomerase: studies with a novel simple peptide substrate. *Biochem J* **315 (Pt 3)**, 1001-5.
147. Shaked, Z., Szajewski, R. P. & Whitesides, G. M. (1980). Rates of thiol-disulfide interchange reactions involving proteins and kinetic measurements of thiol pKa values. *Biochemistry* **19**, 4156-66.
148. Riddles, P. W., Blakeley, R. L. & Zerner, B. (1979). Ellman's reagent: 5,5'-dithiobis(2-nitrobenzoic acid) -- a reexamination. *Anal. Biochem.* **94**, 75-81.
149. Otwinowski, Z. & Minor, W. (1997). Processing of X-ray diffraction data collected in oscillation mode. *Methods Enzymol* **276**, 307-326.

150. Brunger, A. T., Adams, P. D., Clore, G. M., DeLano, W. L., Gros, P., Grosse-Kunstleve, R. W., Jiang, J. S., Kuszewski, J., Nilges, M., Pannu, N. S., Read, R. J., Rice, L. M., Simonson, T. & Warren, G. L. (1998). Crystallography & NMR system: A new software suite for macromolecular structure determination. *Acta Crystallogr D Biol Crystallogr* **54 (Pt 5)**, 905-21.
151. Beckman, J. S., Ye, Y. Z., Chen, J. & Conger, K. A. (1996). The interactions of nitric oxide with oxygen radicals and scavengers in cerebral ischemic injury. *Adv Neurol* **71**, 339-50; discussion 350-4.
152. Butterfield, D. A., Reed, T. T., Perluigi, M., De Marco, C., Coccia, R., Keller, J. N., Markesbery, W. R. & Sultana, R. (2007). Elevated levels of 3-nitrotyrosine in brain from subjects with amnestic mild cognitive impairment: Implications for the role of nitration in the progression of Alzheimer's disease. *Brain Res*.
153. Kamat, J. P. (2006). Peroxynitrite: a potent oxidizing and nitrating agent. *Indian J Exp Biol* **44**, 436-47.
154. Mohiuddin, I., Chai, H., Lin, P. H., Lumsden, A. B., Yao, Q. & Chen, C. (2006). Nitrotyrosine and chlorotyrosine: clinical significance and biological functions in the vascular system. *J Surg Res* **133**, 143-9.
155. Shishehbor, M. H. & Hazen, S. L. (2004). Inflammatory and oxidative markers in atherosclerosis: relationship to outcome. *Curr Atheroscler Rep* **6**, 243-50.
156. Mallozzi, C., Di Stasi, A. M. & Minetti, M. (2001). Nitrotyrosine mimics phosphotyrosine binding to the SH2 domain of the src family tyrosine kinase lyn. *FEBS Lett* **503**, 189-95.
157. Pacher, P., Beckman, J. S. & Liaudet, L. (2007). Nitric oxide and peroxynitrite in health and disease. *Physiol Rev* **87**, 315-424.
158. Ferrer-Sueta, G., Quijano, C., Alvarez, B. & Radi, R. (2002). Reactions of manganese porphyrins and manganese-superoxide dismutase with peroxynitrite. *Methods Enzymol* **349**, 23-37.
159. Beckman, J. S., Ischiropoulos, H., Zhu, L., van der Woerd, M., Smith, C., Chen, J., Harrison, J., Martin, J. C. & Tsai, M. (1992). Kinetics of superoxide dismutase- and iron-catalyzed nitration of phenolics by peroxynitrite. *Arch Biochem Biophys* **298**, 438-45.
160. Sampson, J. B., Ye, Y., Rosen, H. & Beckman, J. S. (1998). Myeloperoxidase and horseradish peroxidase catalyze tyrosine nitration in proteins from nitrite and hydrogen peroxide. *Arch Biochem Biophys* **356**, 207-13.
161. Burner, U., Furtmuller, P. G., Kettle, A. J., Koppenol, W. H. & Obinger, C. (2000). Mechanism of reaction of myeloperoxidase with nitrite. *J Biol Chem* **275**, 20597-601.
162. Santos, C. X., Anjos, E. I. & Augusto, O. (1999). Uric acid oxidation by peroxynitrite: multiple reactions, free radical formation, and amplification of lipid oxidation. *Arch Biochem Biophys* **372**, 285-94.
163. Bartesaghi, S., Ferrer-Sueta, G., Peluffo, G., Valez, V., Zhang, H., Kalyanaraman, B. & Radi, R. (2006). Protein tyrosine nitration in hydrophilic and hydrophobic environments. *Amino Acids*.

164. Zimmer, M. (2002). Green fluorescent protein (GFP): applications, structure, and related photophysical behavior. *Chem Rev* **102**, 759-81.
165. Tsien, R. Y. (1998). The green fluorescent protein. *Annu Rev Biochem* **67**, 509-44.
166. Remington, S. J. (2006). Fluorescent proteins: maturation, photochemistry and photophysics. *Curr Opin Struct Biol* **16**, 714-21.
167. Giepmans, B. N., Adams, S. R., Ellisman, M. H. & Tsien, R. Y. (2006). The fluorescent toolbox for assessing protein location and function. *Science* **312**, 217-24.
168. Heim, R., Prasher, D. C. & Tsien, R. Y. (1994). Wavelength mutations and posttranslational autoxidation of green fluorescent protein. *Proc Natl Acad Sci U S A* **91**, 12501-4.
169. Niwa, H., Inouye, S., Hirano, T., Matsuno, T., Kojima, S., Kubota, M., Ohashi, M. & Tsuji, F. I. (1996). Chemical nature of the light emitter of the Aequorea green fluorescent protein. *Proc Natl Acad Sci U S A* **93**, 13617-22.
170. Bokman, S. H. & Ward, W. W. (1981). Renaturation of Aequorea gree-fluorescent protein. *Biochem Biophys Res Commun* **101**, 1372-80.
171. Li, X., Zhang, G., Ngo, N., Zhao, X., Kain, S. R. & Huang, C. C. (1997). Deletions of the Aequorea victoria green fluorescent protein define the minimal domain required for fluorescence. *J Biol Chem* **272**, 28545-9.
172. Dopf, J. & Horiagon, T. M. (1996). Deletion mapping of the Aequorea victoria green fluorescent protein. *Gene* **173**, 39-44.
173. Wachter, R. M., Yarbrough, D., Kallio, K. & Remington, S. J. (2000). Crystallographic and energetic analysis of binding of selected anions to the yellow variants of green fluorescent protein. *J Mol Biol* **301**, 157-71.
174. Wachter, R. M. & Remington, S. J. (1999). Sensitivity of the yellow variant of green fluorescent protein to halides and nitrate. *Curr Biol* **9**, R628-9.
175. Li, Y., Agrawal, A., Sakon, J. & Beitle, R. R. (2001). Characterization of metal affinity of green fluorescent protein and its purification through salt promoted, immobilized metal affinity chromatography. *J Chromatogr A* **909**, 183-90.
176. Jayaraman, S., Haggie, P., Wachter, R. M., Remington, S. J. & Verkman, A. S. (2000). Mechanism and cellular applications of a green fluorescent protein-based halide sensor. *J Biol Chem* **275**, 6047-50.
177. Chiang, C. F., Okou, D. T., Griffin, T. B., Verret, C. R. & Williams, M. N. (2001). Green fluorescent protein rendered susceptible to proteolysis: positions for protease-sensitive insertions. *Arch Biochem Biophys* **394**, 229-35.
178. Denicola, A., Souza, J. M. & Radi, R. (1998). Diffusion of peroxynitrite across erythrocyte membranes. *Proc Natl Acad Sci U S A* **95**, 3566-71.
179. Souza, J. M., Daikhin, E., Yudkoff, M., Raman, C. S. & Ischiropoulos, H. (1999). Factors determining the selectivity of protein tyrosine nitration. *Arch Biochem Biophys* **371**, 169-78.
180. Shao, B., Oda, M. N., Bergt, C., Fu, X., Green, P. S., Brot, N., Oram, J. F. & Heinecke, J. W. (2006). Myeloperoxidase impairs ABCA1-dependent cholesterol efflux through methionine oxidation and site-specific tyrosine chlorination of apolipoprotein A-I. *J Biol Chem* **281**, 9001-4.

181. Baird, G. S., Zacharias, D. A. & Tsien, R. Y. (1999). Circular permutation and receptor insertion within green fluorescent proteins. *Proc Natl Acad Sci U S A* **96**, 11241-6.
182. Topell, S., Hennecke, J. & Glockshuber, R. (1999). Circularly permuted variants of the green fluorescent protein. *FEBS Lett* **457**, 283-9.
183. Hanson, G. T., McAnaney, T. B., Park, E. S., Rendell, M. E., Yarbrough, D. K., Chu, S., Xi, L., Boxer, S. G., Montrose, M. H. & Remington, S. J. (2002). Green fluorescent protein variants as ratiometric dual emission pH sensors. 1. Structural characterization and preliminary application. *Biochemistry* **41**, 15477-88.
184. Heim, R. & Tsien, R. Y. (1996). Engineering green fluorescent protein for improved brightness, longer wavelengths and fluorescence resonance energy transfer. *Curr Biol* **6**, 178-82.
185. Robinson, K. M. & Beckman, J. S. (2005). Synthesis of peroxynitrite from nitrite and hydrogen peroxide. *Methods Enzymol* **396**, 207-14.
186. D. Scott Bohle, B. H., Scott C. Paulson, Bryan D. Smith. (1994). Biomimetic Synthesis of the Putative Cytotoxin Peroxynitrite, ONOO-, and Its Characterization as a Tetramethylammonium Salt. *J. Am. Chem. Soc.* **116**, 7423-7424.
187. Fraley, T. S., Pereira, C. B., Tran, T. C., Singleton, C. & Greenwood, J. A. (2005). Phosphoinositide binding regulates alpha-actinin dynamics: mechanism for modulating cytoskeletal remodeling. *J Biol Chem* **280**, 15479-82.
188. Greenwood, J. A., Theibert, A. B., Prestwich, G. D. & Murphy-Ullrich, J. E. (2000). Restructuring of focal adhesion plaques by PI 3-kinase. Regulation by PtdIns (3,4,5)-p(3) binding to alpha-actinin. *J Cell Biol* **150**, 627-42.
189. Ormo, M., Cubitt, A. B., Kallio, K., Gross, L. A., Tsien, R. Y. & Remington, S. J. (1996). Crystal structure of the Aequorea victoria green fluorescent protein. *Science* **273**, 1392-5.
190. Roberts, B. R., Wood, Z. A., Jonsson, T. J., Poole, L. B. & Karplus, P. A. (2005). Oxidized and synchrotron cleaved structures of the disulfide redox center in the N-terminal domain of Salmonella typhimurium AhpF. *Protein Sci* **14**, 2414-20.
191. Cannon, M. B. & Remington, S. J. (2006). Re-engineering redox-sensitive green fluorescent protein for improved response rate. *Protein Sci* **15**, 45-57.
192. Hanson, G. T., Aggeler, R., Oglesbee, D., Cannon, M., Capaldi, R. A., Tsien, R. Y. & Remington, S. J. (2004). Investigating mitochondrial redox potential with redox-sensitive green fluorescent protein indicators. *J Biol Chem* **279**, 13044-53.
193. Jensen, L. T. & Culotta, V. C. (2005). Activation of CuZn superoxide dismutases from Caenorhabditis elegans does not require the copper chaperone CCS. *J Biol Chem* **280**, 41373-9.
194. Son, M., Puttaparthi, K., Kawamata, H., Rajendran, B., Boyer, P. J., Manfredi, G. & Elliott, J. L. (2007). Overexpression of CCS in G93A-SOD1 mice leads

to accelerated neurological deficits with severe mitochondrial pathology. *Proc Natl Acad Sci U S A* **104**, 6072-7.

195. Ye, Y., Quijano, C., Robinson, K. M., Ricart, K. C., Strayer, A. L., Sahawneh, M. A., Shacka, J. J., Kirk, M., Barnes, S., Accavitti-Loper, M. A., Radi, R., Beckman, J. S. & Estevez, A. G. (2007). Prevention of peroxynitrite-induced apoptosis of motor neurons and PC12 cells by tyrosine-containing peptides. *J Biol Chem* **282**, 6324-37.
196. Estevez, A. G., Spear, N., Manuel, S. M., Radi, R., Henderson, C. E., Barbeito, L. & Beckman, J. S. (1998). Nitric oxide and superoxide contribute to motor neuron apoptosis induced by trophic factor deprivation. *J Neurosci* **18**, 923-31.
197. Potter, S. Z., Zhu, H., Shaw, B. F., Rodriguez, J. A., Doucette, P. A., Sohn, S. H., Durazo, A., Faull, K. F., Gralla, E. B., Nersissian, A. M. & Valentine, J. S. (2007). Binding of a Single Zinc Ion to One Subunit of Copper-Zinc Superoxide Dismutase Apoprotein Substantially Influences the Structure and Stability of the Entire Homodimeric Protein. *J Am Chem Soc*.
198. Tiwari, A. & Hayward, L. J. (2003). Familial amyotrophic lateral sclerosis mutants of copper/zinc superoxide dismutase are susceptible to disulfide reduction. *J Biol Chem* **278**, 5984-92.
199. Field, L. S., Furukawa, Y., O'Halloran, T. V. & Culotta, V. C. (2003). Factors controlling the uptake of yeast copper/zinc superoxide dismutase into mitochondria. *J Biol Chem* **278**, 28052-9.
200. Inarrea, P., Moini, H., Han, D., Rettori, D., Aguilo, I., Alava, M. A., Iturralde, M. & Cadenas, E. (2007). Mitochondrial respiratory chain and thioredoxin reductase regulate intermembrane Cu,Zn-superoxide dismutase activity: implications for mitochondrial energy metabolism and apoptosis. *Biochem J*.
201. Pandhare, J. & Deshpande, V. (2004). Both chaperone and isomerase functions of protein disulfide isomerase are essential for acceleration of the oxidative refolding and reactivation of dimeric alkaline protease inhibitor. *Protein Sci* **13**, 2493-501.
202. Laboissiere, M. C., Sturley, S. L. & Raines, R. T. (1995). The essential function of protein-disulfide isomerase is to unscramble non-native disulfide bonds. *J Biol Chem* **270**, 28006-9.
203. Atkin, J. D., Farg, M. A., Turner, B. J., Tomas, D., Lysaght, J. A., Nunan, J., Rembach, A., Nagley, P., Beart, P. M., Cheema, S. S. & Horne, M. K. (2006). Induction of the unfolded protein response in familial amyotrophic lateral sclerosis and association of protein-disulfide isomerase with superoxide dismutase 1. *J Biol Chem* **281**, 30152-65.
204. Lamb, A. L., Torres, A. S., O'Halloran, T. V. & Rosenzweig, A. C. (2001). Heterodimeric structure of superoxide dismutase in complex with its metallochaperone. *Nat Struct Biol* **8**, 751-5.